EMERGENT COLLECTIVE PHENOMENA IN *V. CHOLERAE* BIOFILMS, MIXED HUMAN-AUTONOMOUS FLEETS, AND NASCENTLY MULTICELLULAR BODIES.

A Dissertation
Presented to
The Academic Faculty

By

David Yanni

In Partial Fulfillment
of the Requirements for the Degree
Doctor of Philosophy in the
School of Physics

Georgia Institute of Technology

December 2019

EMERGENT COLLECTIVE PHENOMENA IN *V. CHOLERAE* BIOFILMS, MIXED HUMAN-AUTONOMOUS FLEETS, AND NASCENTLY MULTICELLULAR BODIES.

Approved by:

Dr. Peter Yunker, Advisor
School of Physics
Georgia Institute of Technology

Dr. William Ratcliff
School of Biology
Georgia Institute of Technology

Dr. Brian Hammer
School of Biology
Georgia Institute of Technology

Dr. Kurt Wiesenfeld
School of Physics
Georgia Institute of Technology

Dr. J.C. Gumbart
School of Physics
Georgia Institute of Technology

Date Approved: November 4, 2019

ACKNOWLEDGEMENTS

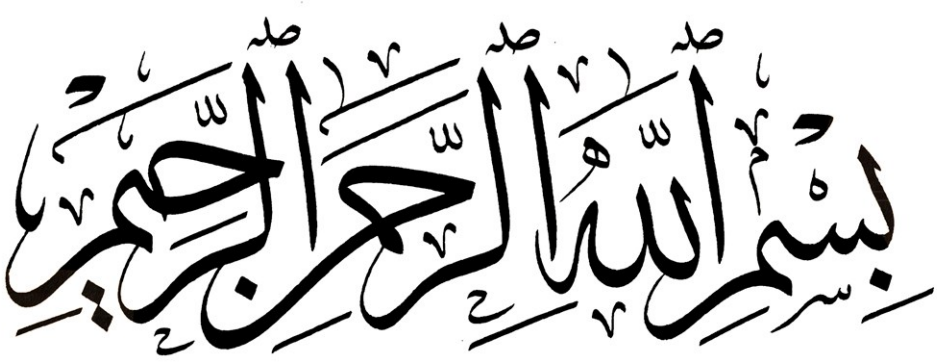

My advisor, Prof. Peter Yunker, has been a role model for me to aspire to throughout my graduate school career. He knows how to maintain optimism and faith in a project, how to fundamentally respect the ideas of others and give them room to develop those ideas on their own while simultaneously remaining available for feedback and guidance, and how to balance science with everything else important in life. He has been not just a patient science mentor, but has also taught me how to speak publicly, how to navigate the games we all must play in our careers with honesty, efficiency, and minimal frustration, and has imparted countless other small wisdoms and professional skills that add up to a complete training. Importantly, he reached out during a very difficult time when my daughter Noura was in the NICU while my wife was in the ICU of a different hospital, and organized a schedule (along with his wife Dr. Erin Buckley) for fellow lab members to help out making sure I had something to eat throughout that week. Peter is an excellent human and I would like to thank him first and foremost.

Secondly, I thank Will Ratcliff, Brian Hammer, and Jesse Silverberg. Each member of this trio rose above the level of collaborator and provided crucial guidance and additional mentorship at key moments throughout my graduate career.

Third, I thank fellow lab mates without whom none of this work would have been possible. Arben Kalziqi, Shane Jacobeen, and Jonathan Michel welcomed me to the lab and showed me the ropes. Ben adopted me onto the effective temperature project and taught me to love Stephen Wolfram. Shane provided me with painstakingly gathered AFM measurements and offered words of encouragement during my overwhelming first year of coursework— which is like drinking from a firehose. Skanda Vivek and I kept the traffic project interesting for each other, and discussed ideas and helped each other out over games of racquetball. Gabi Steinbach has really provided a great deal of experimental insight into *V. cholerae* biofilms and brought life to projects I think would have gone stale without her. All of the above, as well as Ali and Tom, also stepped up and helped out when Noura was first born. For that I am tremendously grateful.

Finally, I thank my parents who made it possible for me to approach physics without crippling debt hanging over my head, my wife Rafiya who has patiently supported me and offered insight and advice without complaint, even while I chatter endlessly about bacteria and traffic at home and in my sleep, and my mother in law Bushra Khala who has made it possible for me to focus on work knowing that Noura is safely in loving hands, especially during this past few months.

TABLE OF CONTENTS

LIST OF TABLES

LIST OF FIGURES

PREFACE

When reviewing all the work I've done in graduate school in preparation for writing this document, I was immediately confronted with the fact that my contributions have been... lets say "eclectic". On the one hand I have spent time in the laboratory with the lights off photographing bioluminescent *V. harveyi* bacteria to test what impact the coffee-ring effect has on quorum sensing during the formation of a sessile community of microbes. On the other hand I have spent time at the computer wrestling with the Google Places API to find the location of every hospital in Manhattan so that I could calculate the fraction of hospitals likely to become inaccessible during a large scale hack of internet connected vehicles in Manhattan. This raises the question— in what subfield do I possess a PhD level understanding? Vehicular traffic? Microbial social evolution? The answer I'd be most comfortable arguing for is *prototyping minimalistic simulations of a particular type of many-component system, and leveraging the results to develop lightweight physics based theory*. Now I'll try to say what I mean by that.

In the early days of digital computers, simulation was difficult, niche, and often met with skepticism. During the Manhattan Project a Monte Carlo algorithm was famously implemented on a punch-card IBM computer simulating just 12 hard spheres. This was considered revolutionary at the time. Since then the use of computer simulation has advanced to the point that many disciplines in science (and especially engineering) simply couldn't function without them. Some have even envisioned scientific inquiry as a trio of mutually reinforcing approaches: theoretical, experimental, and computational. Obviously there are plenty of fields that get along just fine without much computation and without any direct simulation. However, there are two categories of many-body systems in which this trio picture rings especially true.

The first case is when the microscopic dynamics of the constituent particles are very well known, but the sheer number of particles or the complexity of their interaction makes

it difficult to predict *a priori* some macroscopic behavior of interest. The macroscopic behaviors we are interested in are usually more difficult to directly observe experimentally in these systems as well. Some examples are: the equilibrium dynamics of proteins within a cellular environment, the effect of small weight-percent additives on the electronic behavior of metals and oxides, and the heat-transfer behavior of physically heterogeneous solids. For these examples common approaches are molecular dynamics, density functional theory, and finite element analysis, respectively. These simulation approaches are entire fields unto themselves, are advanced and nuanced, and require a great deal of skill to master. A scientist could definitely expect to spend his or her career contributing to the simulation corner of the simulation-experiment-theory triangle. These are not the type of simulations that I have focused on.

Instead, I've spent most of my time thinking about a second type of many-body system in which simulations are tremendously helpful. That is where the macroscopic behaviors are relatively easy to observe but are unpredictable and/or not understood, and the microscopic details of the system are numerous and/or complex. We see flash-crashes in the stock market, traffic jams that persist and even travel for days after an accident, raft and trail and bridge formation in ants, and spontaneous synchronization in fireflies. When physicists investigate these sorts of systems it's often called "active matter physics". We would like to understand these phenomena, but modeling the multitude of details about the underlying individual constituents that could possibly give rise to these emergent macroscopic behaviors can be difficult or impossible. For example, we observe long-range orientational order in flocks of birds; can birds achieve this using only local information (velocity matching to near neighbors), or would we need to understand a lot about bird brains to figure out how this happens? In a suspension of motile *E. coli* we can observe high density clumps of bacteria form, surrounded by lower density regions of fast swimming bacteria; can this behavior be captured by a minimal description of a bacterium as an active brownian particle? Would we observe this pattern formation with any motile bacteria or is there some

particular genetic basis unique to the lab strain were using? If I simulate traffic, do I need to include the detail that drivers decelerate more rapidly than they accelerate in order to capture observed traffic behavior like the waves of high density "traffic jams" that travel "upstream"? For a biofilm composed to two strains of *V. cholerae* equipped with the type VI secretion system we see a very specific form of height-height correlations on the surface of the biofilm that is related to cellular activity in the bulk of the biofilm. Is cell shape important for this effect? How about the production of exopolysaccharides?

Successful simulations of this type of system are often abstract and simple. The famous Vicsek model for flocking can be implemented as a simulation in just a few lines of code and run on any modern computer quickly enough to generate any data wed be interested in. The Nagel-Schreckenberg cellular automaton model for traffic reduces the entire complexity of human driving behavior on a roadway to a one dimensional grid of occupied and unoccupied sites and four basic update rules. So implementing such a simulation, especially in 2019, is almost embarrassingly easy. That is to say it's easy once you've decided what to include in your simulation. The difficult part is prototyping lots of these simulations and using systematic tinkering to figure out which details are really important, which ones are less important, and which ones are important but that you've incorporated incorrectly. Once a simulation is written, you need to carefully analyze and interpret its outputs and try to tie them to existing theory and experiments. Often you then need to go back and tweak your simulation. This cycle is where I've spent most of my time.

The usefulness of simple simulations in throwing into clear relief what appear in retrospect to have been obvious facts about a system is the real reason I ended up starting to collaborate on so many disparate projects. Although active matter physics theory is quite advanced in some areas, often there is no clear physical picture so simulations can elucidate important underlying mechanisms.

What hopefully happens with a successful simulation is that you are able to make a connection between microscopic dynamics and emergent macroscopic behaviors in a way

that adds understanding or predictive power. For example when you understand the microscopic origins of traffic jams you might be able to program self-driving cars to prevent them. A nice bonus is that sometimes you notice new phenomena. For example, in a simple biofilm simulation in which immotile cells reproduce at a rate proportional to their distance to available nutrients we noticed an overall upward convection of cells away from nutrient media and toward the top of the biofilm. When simulated cells reproduce at a uniform rate regardless of nutrients this effect disappears. This upward convection effect was observed in biofilm experiments where tracer beads drifted upward over time. Tying this result back to, and expanding on, existing physical theory relating cell death and division was only possible because of simple simulations. This is an example of the method working.

As another example, when simulating traffic dynamics after a large-scale hack we noticed that sometimes you would see congested traffic while other times with all of the same parameters you would see traffic just completely halt altogether. We were then able to describe this effect as obstacle percolation and write down an analytical prediction for its probability. Obstacle percolation seems sort of obvious in retrospect, and it is more or less an elementary exercise in probability theory to write down an equation for it. But the whole process from simulation to mathematics takes time to get right.

Furthermore, working in this area is necessarily collaborative if you're a physics student. If you want to simulate bacteria you need to be in contact with a biologist! Working with scientists from other disciplines expands and refines your definition of an interesting question. So when you have your simple model working properly and notice some new phenomena you want to ask follow-up questions that are natural to the system itself, not just follow-up questions that are natural for a physics student. Once we noticed obstacle percolation we wanted to investigate what that would mean for cyberphysical risks of internet connected vehicles in a large city like Manhattan. And once we figured out how the coffee ring effect impacts bacterial spatial distribution we wanted to figure out what sort of ecological consequences that would imply.

Simple simulations and lightweight theory, usually particle-based or cellular automaton simulations informed by soft-matter physics intuition, have been where I spent most of my time and effort. They are in the arena where my strongest training lies in terms of methodology. They are what I would argue that I understand at a PhD level. However, in terms of *content*, I have worked on mainly three distinct model systems and have helped to develop three distinct lines of scientific inquiry, that each deserve the respect of their own scientific narrative.

For that reason I've chosen to divide up the dissertation as follows. I present three separate "mini-dissertations" for the distinct systems I've worked on, with an emphasis first on the physics and second on more system-specific results. The above is the extent of the overall summary and discussion that relates them, but within each chapter I give relevant summary and literature review. Each chapter also contains its own conclusions or outlook section according the what is appropriate to each system as well as the work presented here. Simulations have played a central role in all of these projects, as discussed above. However, the details related to their implementation do not represent the major contributions of this work, and so these implementation details have been suppressed to the appendix.

CHAPTER 1

PUBLICATIONS

Much of the text and many of the figures in this dissertation is drawn from work that has either been previously published, is under review, or has been submitted for review. It therefore would seem to be helpful to simply list every work on which I am a co-author here. I am including arXiv preprints in this list.

- Yanni D, Mrquez-Zacaras P, Yunker PJ, Ratcliff WC. Drivers of Spatial Structure in Social Microbial Communities. Current Biology. 2019 Jun 3;29(11):R545-50.

- Vivek S, Yanni D*, Yunker PJ, Silverberg JL. Cyber-physical risks of hacked Internet-connected vehicles. Phys. Rev. E. 2019 Jul; 100(1):012316

- Vivek S, Yanni D, Yunker PJ, Silverberg JL. Collective behavior and emergent risks in a model of human-and autonomously-driven vehicles. arXiv preprint arXiv:1708.03791. 2017 Aug 12.

- Yanni D, Kalziqi A, Thomas J, Ng SL, Vivek S, Ratcliff WC, Hammer BK, Yunker PJ. Life in the coffee-ring: how evaporation-driven density gradients dictate the outcome of inter-bacterial competition. arXiv preprint arXiv:1707.03472. 2017 Jul 11.

- Kalziqi A, Yanni D, Thomas J, Ng SL, Vivek S, Hammer BK, Yunker PJ. Immotile Active Matter: Activity from Death and Reproduction. Physical review letters. 2018 Jan 5;120(1):018101.

- Kalziqi A, Ng SL, Yanni D, Steinbach G, Hammer BK, Yunker PJ. Viscosity independent diffusion mediated by death and reproduction in biofilms. arXiv preprint arXiv:1901.01350. 2019 Jan 5.

Furthermore, the chapter in this document entitled “Topological constraints in early multicellularity favor reproductive division of labor” has been submitted very recently to PNAS. I am listed as co-first author on that manuscript.

CHAPTER 2
CONTRIBUTIONS

Due to the highly collaborative nature of the work presented in this dissertation, it could be difficult to evaluate my work without knowing which parts of the overall effort presented here are my work in particular. Therefore, I have devoted this chapter to clearly describe what I did and did not do to contribute to each project. In particular, I'd like to point out a few places where work in this document is presented which was primarily the effort of another lab member.

- Biofilm Experiments: All of the strains used were developed by the Hammer lab—particularly by Jacob Thomas, Siu Lung Ng, and Brian Hammer. All of the interferometry experiments and associated data analyses were performed by Arben Kalziqi. All of the tracer bead experiments and associated analysis was performed by Gabi Steinbach and Arben Kalziqi. Most of the confocal microscopy images associated with the coffee-ring project were taken by Jacob Thomas or Arben Kalziqi, although I did spend some time on that microscope.

- SVYY model: Jesse Silverberg originally proposed this model; I performed subsequent analyses (stability analysis and flux/density prediction), implemented it in Python, and Skanda Vivek and myself analyzed output from simulations.

- Calibration of SVYY model human response time: Skanda Vivek analyzed the live video footage of traffic and the NGSIM data used in chapter 4.

- Fitness model: Shane Jacobeen proposed the model for group fitness used in chapter 5, and originally had implemented some evolutionary simulations. I carried out the analysis and re-implemented many of the simulations.

With the exception of the above items, I was the major co-contributor to all of the theoretical, experimental, and computational results presented in this dissertation.

CHAPTER 3
NONEQUILIBRIUM MECHANICS AND INITIAL CONDITIONS STRUCTURE *V. CHOLERAE* BIOFILMS

3.1 Background

Microorganisms frequently attach to surfaces and form densely packed communities called biofilms. These communities are of fundamental scientific interest. To begin with, bacterial biofilms represent one of the oldest dominant mode of life on earth, and the biofilm lifestyle is arguably still the most common [1]. Thus, biofilms — particularly bacterial biofilms — have likely had a profound effect on the evolutionary trajectory of all life. This is not only because bacteria are old, arising shortly after the origin of life itself, about 3.5Mya ago [2]. Bacteria also exhibit astounding diversity (millions of species), abundance (10^{30} bacterial cells on earth), and robustness— thriving in the most extreme of environments [3]. Such achievements are attained in large part through cooperative living in densely packed communities. In fact, these communities appear so hearty that astrobiologists suggest that extraterrestrial life will very likely include biofilms. [4, 5]

Of course, there are also enormous practical upshots to the study of biofilms. The National Institute of Health indicated that at least 80% of all microbial infections are associated with biofilm formation, for a combined cost in the billions of dollars [6, 7, 8]. Biofilms bother in other areas as well, such as the food [9], water [10], and oil industries [11]. Biofouling due to microbial biofilms carries an economic impact in the billions of dollars on the global shipping industry alone.[12]

While bacterial biofilms are ancient, pervasive, and expensive, *scientific understanding* of biofilms is not (yet) commensurately mature. This state of affairs arises in part because biofilms are just outright complicated. They can be considered highly spatially

structured ecosystems, with multiple microhabitats housing diverse strains and even taxa, embedded in a background polymeric matrix. Mechanical and mass transport properties are different, and usually more complex and more heterogenous within biofilms than in liquid environments [13]. Of course, this increased physical complexity is both an influence on, and a consequence of biological contingencies that can vary based on the genetic makeup of the community and the phenotypic state of constituent cells- such as the quantity and identities of exopolysaccharides (EPS) produced, the presence of persister cells and other phenotype variants[14], the production of digestive enzymes and other proteins, intercellular signalling mechanisms etc. The more we have learned about biofilms, the more complex our models have become— from single-strain, chemically-uniform films in the 1970s [15], to coupled mechanical-chemical-individual-based Frankenmodels that can account for observed biological and physical behavior like wrinkling, the uptake of water, and co-evoltion [16, 17, 18, 19]. A central theme that has emerged is that important characteristics of biofilms, such as antibiotic resistance [20], arise at least in part due to material properties and the physical embeddedness of bacteria in biofilms— not just genetic and chemical interactions alone [21, 13].

As Evan et al note, the increasing appreciation for the importance of biofilm mechanics is evidenced by the growing number of reviews on the physics of biofilms in recent years. [21, 13, 22, 23, 24] This includes understanding physical forces at the individual bacterium level, such as hydrodynamic forces and adhesion [25], as well as structural properties at macroscopic scale [26].

3.1.1 How physics informs biofilms

Biophysicists who study bacteria have historically focused on mechanics at the single cell level, which, in the biofilm context, certainly affect emergent larger length scale structures. For example, AFM studies with functionalized tips probe the turgor pressure exerted against the cell wall, which bears on both cell shape and the mechanical effects of lysis.

[27]. These properties in turn affect, for example: packing density, wrinkling, and genetic demixing. [16, 28] Other cellular characteristics feed into the overall structure and therefore function of biofilms. Mechanosensitive channels may be involved in regulating growth rates[29, 30, 31], bacterial pili are important active components involved in adhesion and biofilm formation[32], surface motility[33], and local antagonism [34, 28]. Finally and perhaps most importantly, cells in biofilms express different phenotypes than their planktonic counterparts [35], with the most prominent difference being the production and secretion of a suite of proteinaceous and polymeric substances (EPS) [1].

The few single-cell details described above barely begin to scratch the surface of what could be enumerated. The question is then, *which bacterial behaviors and/or properties really dominate the macroscopic material behavior of the collective?* Understanding the micro-to-macro link not only strengthens the predictive power of our macroscopic mechanical models, it potentially opens the door to learning about microscopic details through relatively easy macroscopic measurements. For example, if antibiotic resistance, and generally resistance to chemical challenge [21] arise out of mechanical properties - then can probing mechanical properties reveal antibiotic resistance? Understanding biofilm mechanics would also potentially reveal e.g. biofilm removal or maintenance strategies.

What is already known about the macroscopic behavior of biofilms, and about the micro-macro link? Rheological experiments [36, 37, 38, 39] unanimously show that biofilms are viscoelastic. That is maybe unsurprising. As Wilking, Weitz et al point out soft matter physics can be used to describe biofilm: rigid colloidal-like bacteria are embedded in an extracellular matrix resembling a chemical polymer gel, forming a solid composite biomaterial. [40]. What is less obvious is whether biofilms — notoriously heterogenous — share anything further in common than falling into this quite broad class of rheological behavior. In addition to viscoelasticity, one of the most obvious unique ingredients for a universal mechanical model of biofilms is growth. In this vein, there has been some progress toward thinking of biofilms as “active hydrogels plus growth” [13, 41]. There are also similari-

ties between the physics of biofilms and the physics of eukaryotic cellular aggregates like tumors or other tissues [42, 43]. There, cells act as elastic components and the whole tissue becomes fluidized due to cellular activity. Of course, in tissues cells are generally genetically identical and competitive dynamics are unlikely to alter the mechanical behavior of the collective. Biofilms, however, are usually polymicrobial and population structure can spontaneously emerge. Patches of different lineages can behave differently (e.g. by secreting different compounds, having different cell shapes and stiffnesses, etc.) Furthermore, spatial structure can effect evolutionary dynamics, leading to a feedback loop where structure affects competition which in turn loops back to affect structure.

So while there are promising avenues for development, ultimately the physics of biofilms is still largely under construction, with several outstanding uncertainties such as: how to relate cell-level activity to macroscopic observable quantities, to what extent biofilms can be compared to tissues, which details are most important to collective biological and mechanical properties, how initial conditions and dispersal affect biofilm form and function, and how population dynamics feeds back into all of the above. There are similarities to tissue mechanics and hydrogel physics, which means we may be able to apply or transfer some of what we've learned from those systems to understanding biofilms. On the other hand, bacterial biofilms are a readily available experimental system, so that elucidating the physics involved in biofilms may shed light on similar active systems like tissue mechanics and active hydrogels.

3.1.2 How biofilms inform physics

In fact, the idea that bacteria can teach us about physics is nothing new. As Evan et al [13] point out, studying bacteria has inspired advances in physics from super-fluidity to topological defects. [44, 45] Bacteria have probably had the most influence on the development of active matter physics, where their collective dynamics are quite well explored [46, 47]. Bacteria are treated as "active brownian particles" with superdiffusive behavior and model

B phase separation [48, 49], or active nematics leading to liquid crystalline states with active defects [50, 51], or active colloid-like components in "active gels" [52, 41].

Active matter physics is a rapidly developing branch of nonequilibrium statistical physics with a firm theoretical grounding [52], where constituents locally convert potential energy into activity and thus break detailed balance [53, 54, 55]. However, most researchers focus on activity that arises from particle mobility. Can the framework of active matter physics be used to successfully describe biofilms, where cells are typically immotile and activity arises from lysis and reproduction?

3.2 Immotile active matter

The rheology of a material is intimately related to its thermal and mass-transport properties like diffusion constant(s). Both diffusion and viscous flow, for example, involve structural rearrangements, which is why the Einstein/Smoluchowski observation that diffusion depends on viscosity should not be surprising. In fact, the whole idea of passive microrheology is to take advantage of the inherently mechanical nature of thermal energy to drive a tracer probe and track diffusion, and then relate diffusion back to macroscopic mechanical properties like viscosity.

Of course, we can simply measure various moduli of biofilms in e.g. a rheometer, but can we relate the microscopic details of constituent motion and activity to these measured moduli similarly to how we can for conventional materials? In other words, can we play the same trick? Is there some sort of effective temperature that can play the role that thermal temperature does in passive materials?

To answer these questions we built on previous work on the mechanics of tissues [42, 43]. Ranft et al developed a continuum description of an elastic tissue that is then perturbed by stresses induced by cell division and apoptosis (i.e. cell birth and death). For a conventional continuum model of a non-living material there is no change in global constituent number, so a continuity equation can be written for the density: $\partial_t \rho + \nabla \cdot (\rho \vec{v}) = 0$. If

there's a change in the density of material then it had to come from or go to somewhere else! Ranft et al consider density fluctuations arising from cell death and reproduction as source and sink terms to this continuity equation $\partial_t \rho + \nabla \cdot (\rho \vec{v}) = (k_d + k_a)\rho$, for division and apoptosis rates k_d and k_a, respectively. These density fluctuations are felt as stresses, and under force balance, they find that the tissue effectively behaves as a viscoelastic material with a relaxation time set by k_d and k_a.

This was a powerful piece of theoretical work, and not only strengthens our understanding of tissue mechanics but potentially allows for macroscopic characterization of microscopic activity in a tissue. For example, by subjecting a slab of tissue to a sustained shear and measuring the "creep" over time one could measure the effective relaxation time and infer the internal activity rates. Ranft et al even propose that their theory could potentially lead to developments in characterization of tissues in the future. Of course, this sort of mechanical measurement is not typically as accessible for tissues as it might sound at first. The timescales involved to see viscous behavior in tissues is quite large, and keeping tissues well fed and behaving normally under laboratory conditions while simultaneously applying mechanical stresses is nontrivial. Recently, Risler et al extended the work of Ranft et al, making predictions about how death and reproduction affect surface height fluctuations in a thin semi-infinite tissue in the homeostatic limit. By observing the surface height fluctuations of a tissue it should then be possible to make inferences about internal cellular activity, which they show can be characterized by a wave-number dependent effective temperature.

However, while observing the surface of a tissue is less invasive, there are still experimental challenges when using tissues. In short, tissues are difficult to keep happy in laboratory conditions, and trying to genetically adjust specific cellular behaviors of interest, like apoptosis rate, is likely to trigger many other downstream changes that could be difficult to keep track of, and complicate the interpretation of any experimental findings. Biofilms, on the other hand, are a natural model system to test the theoretical predictions of

Risler et al. Genetic manipulation of bacterial cells is much more advanced, and biofilms are (relatively) easy to prepare and control in laboratory conditions.

Experimental validation of Risler et al's predictions in a biofilm represents significant progress toward understanding the physics of biofilms. The theory was developed for a genetically and physically homogeneous, elastic, slab of tissue with apoptosis and cell division distributed randomly throughout the tissue. Bacterial biofilms are genetically and physically heterogenous, viscoelastic consortia of cells embedded in a background polymeric matrix, wherein lysis and cell division are unlikely to be distributed uniformly. Can a simple physical theory that emphasizes death, division, and mechanical equilibration capture the behavior of such a messy system?

We used a model system of a biofilm composed of two strains of *V. cholerae* that are genetically identical except for their ability to kill the other strain but not their kin (see appendix for details). Biofilms were grown to the homeostatic limit and then their surface was scanned with a nanometer resolution interferometer to extract surface height profiles. These "mutual killer" biofilms were compared to control experiments wherein biofilms composed of nonkiller bacteria were measured in a similar manner. The results of these experiments are shown in Fig 3.1.

By measuring height correlation functions on the surface of biofilms we can extract $C(q) = \mathcal{F}[\langle h(\vec{r})h(\vec{r}+\vec{r}_0)\rangle]$, where $\mathcal{F}$ denotes the Fourier transform, the angled braces $\langle ...\rangle$ denotes average over all $\vec{r}_0$, and $h(\vec{x})$ is the difference in biofilm height at point $\vec{x}$ from the homeostatic biofilm height. The prediction given by Risler et al is that (to leading order)

$$C(q) = \frac{\eta\lambda_{act}}{\rho\left(\gamma q^2 + \kappa q^4\right)} \tag{3.1}$$

$$C(q) = \frac{k_B T_{eff}}{\left(\gamma q^2 + \kappa q^4\right)} \tag{3.2}$$

Here equation 3.1 is a zero-free-parameter expression with mechanical properties of the

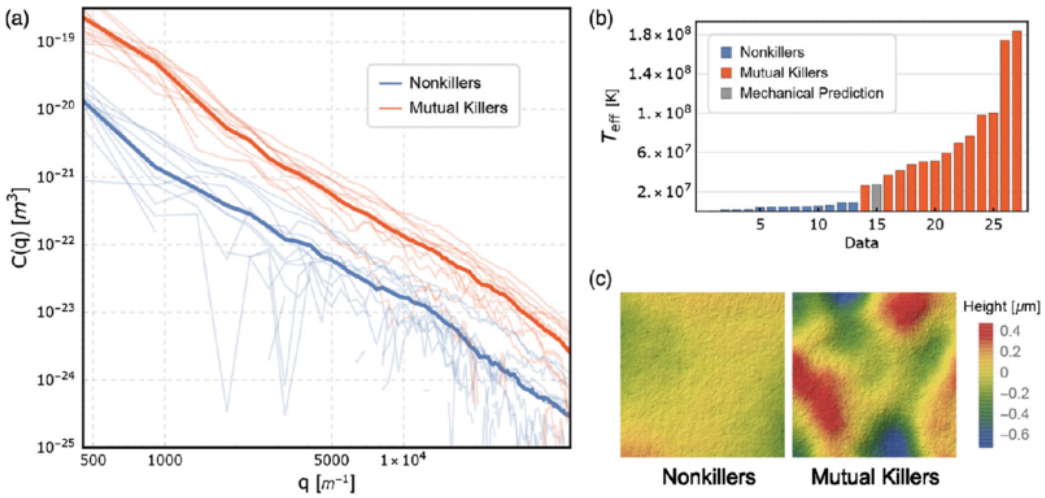

Figure 3.1: reprinted from [56]: (a) A log-log plot of the Fourier transformed correlation functions $C(\mathbf{q})$, obtained via interferometry, shown as faint blue (nonkiller) and faint red (mutual killer) lines. Full-opacity lines are averages over 13 nonkiller samples and 13 mutual killer samples. (b) A bar plot of all extracted effective temperatures for nonkiller and mutual killer biofilms. Nonkillers and mutual killers are entirely separated from one another. The mechanically predicted T_{eff} is shown in gray. (c) Selected surface relief plots of the homelands of nonkiller biofilms and mutual killer biofilms. The mutual killer biofilm topographies are all rougher than their nonkiller counterparts. Each relief plot is $700 \times 700\,\mu\mathrm{m}$

Table 3.1: Mechanical properties of biofilm

symbol	**meaning**	**measurement**
γ	surface tension	*Forgacs et al*
κ	bending rigidity	*Landau and Lifschitz*
η	viscosity	stress relaxation (shear viscosity)

biofilm given in table 3.1, along with the cellular activity rate λ_{act} and the cellular number density ρ. Equation 3.2 is the expected height fluctuations of a thin membrane in a thermal bath of temperature T_{eff} with surface tension and bending rigidities given by γ and κ, respectively.

By fitting the data in Fig 3.1 **(a)** to the functional form of Eq. 3.2, an effective temperature can be inferred. Independent mechanical measurements of all the parameters in Eq. 3.1 were made in order to generate the T_{eff} "mechanical prediction" shown in Fig. 3.1 **(b)**. We find that qualitatively, the effective temperature behaves as expected. The mutually killing biofilms have a larger activity rate and thus have rougher surfaces (Fig. 3.1 **(c)**), and larger effective temperatures (Fig. 3.1 **(b)**).

To gain more mechanical insight into the surface roughening process, and test whether a biologically minimalistic model can be responsible for the effective temperature difference observed, we turned to individual based simulations. Briefly, The model is a physically motivated, biologically minimal framework that focuses on the active matter aspects of biological solids. Member cells interact mechanically as repelling, elastic spheres embedded in a viscous medium. Cells undergo growth, division, and death but are otherwise biologically inert. Death can be induced by interstrain contact killing or can occur naturally (see Appendix for simulation details). While the "low killing" simulation deviates substantially at large wavenumbers due to finite time effects, the high killing simulations and measured $C(q)$ agree very well with the independent mechanical prediction.

The agreement between these simulations, experiments, and the Risler et al theory is surprising. As noted above, the theory was developed for a genetically and physically homogeneous, elastic, slab of tissue with apoptosis and cell division distributed randomly

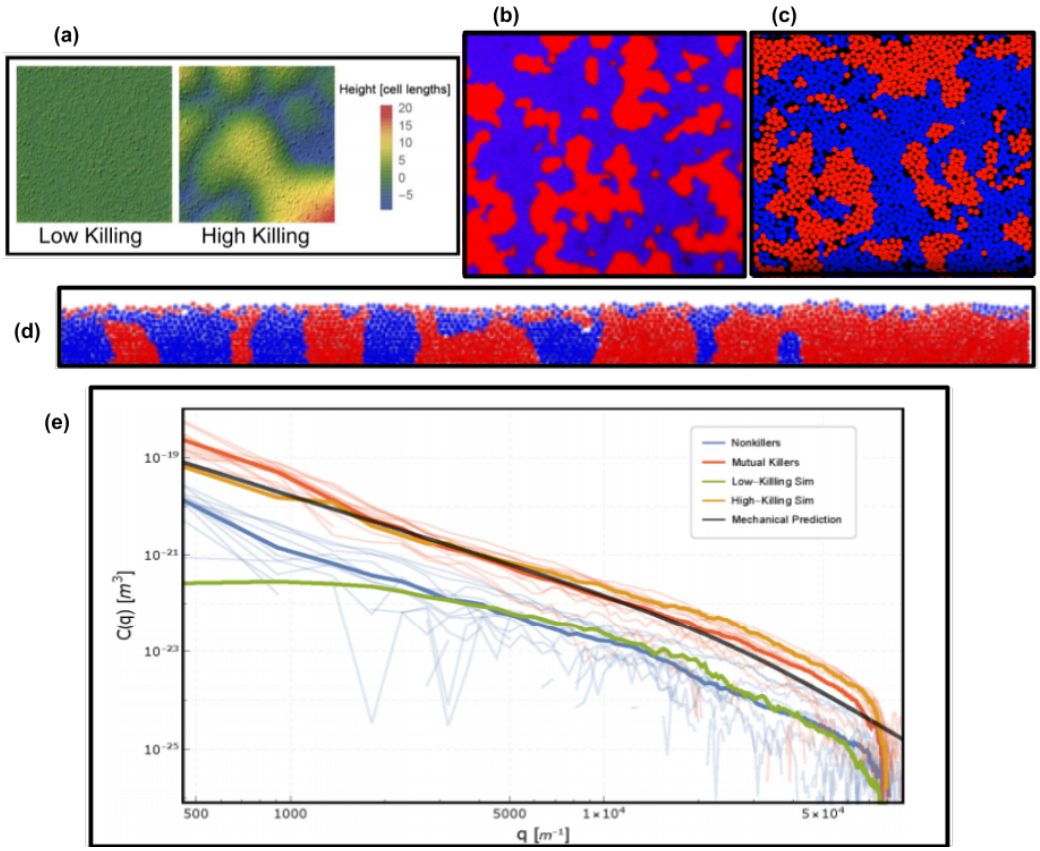

Figure 3.2: (a) Surface relief plot showing simulated biofilm surfaces for low killing (c.f. nonkillers) and high killing (c.f. mutual killers). (b) Typical experimental mutual killer biofilm confocal microscopy image, and (c) top view of simulated biofilm. (d) A log-log plot of the Fourier transformed correlation functions $C(\mathbf{q})$, obtained via interferometry, shown as faint blue (nonkiller) and faint red (mutual killer) lines. Full-opacity lines are averages over 13 nonkiller samples and 13 mutual killer samples. Solid black line shows the mechanical prediction based on measurements made as described in table 3.1. Green line shows the $C(q)$ for low killing simulations and orange line shows it for high killing simulations. (e) A typical side view of a simulated biofilm.

throughout the tissue. Our simulated and lab-grown biofilms are genetically and physically heterogenous consortia of cells, wherein lysis and cell division are concentrated near strain/strain interfaces. Furthermore, the theory describes a collection of elastic components that develops an *effective* viscosity. A closer look at the mechanical prediction Eq 3.1 reveals an ambiguity— what value should be used for the viscosity η?

3.2.1 Adding viscoelasticity

The experiments, simulations, and theory tested above were all in the elastic regime. The lab grown biofilms tested therein were somewhat artificial in that sense. Usually biofilms comprise elastic rod-like cells *and* extracellular polymeric material, whereas the bacterial strains we used were engineered to produce no such material. Our simulations neglected extracellular matrix as well. Finally, the Ranft et al theory is for an elastic tissue without extracellular matrix. However, viscoelasticity in biofilms is crucial. Since the viscoelastic properties of biofilms are hypothesized to account for many of their anomalous biological properties, like antibiotic resistance, the natural next step is to add viscoelasticity to our analysis.

We start with a simplified simulation framework. To capture the viscoelastic character of biofilms, we model them as chains of cells coupled by Voigt-Kelvin elements. Reproduction and death are assumed to be Poisson processes with an activity rate λ_{act} (Fig. 4a); the time-step between events is chosen from an exponential distribution $dt \sim e^{-\lambda_{\text{act}} t}$. Each event corresponds, with equal probability, to the step-strain resultant from reproduction or death of a cell at a random position in the biofilm, and as such imposes a step stress $\pm\sigma_0$ felt instantaneously throughout the biofilm. Finally, after each event the velocities and positions of all the cells are updated according to the current state of stress in the biofilm and the constitutive equations $\sigma(t) = E\epsilon(t) + \eta\frac{d\epsilon(t)}{dt}$, using backward-Euler integration, where E is the elastic modulus, η is viscosity and ϵ is strain. We noticed a surprising result; *diffusion of cells in this simulation is independent of the viscosity of the dashpots!*

To test this result on experimental biofilms we first used height correlation functions to extract effective temperatures from biofilm surface roughness according to Eq. 3.2. We measured effective temperatures for two biofilms with equivalent activity rates but different levels of extracellular matrix production— leading to different measured shear viscosities. We call these Matrix+ (high levels of extracellular polysaccharide production) and Matrix- (nearly zero extracellular polysaccharide production). The Matrix- strains are identical to the ones used earlier. We took these effective temperatures seriously, as *temperatures*, and used them in the Generalized Stokes-Einstein relation [57] to compute effective diffusivities. We find that the effective diffusivities, describing cellular diffusive motion, are nearly identical, despite the difference in measured viscosity! Fig. 3.3 showcases these results. The question then, is whether it is valid to treat extracted effective temperatures measured from a curve fit of height correlations versus wavenumber for a membrane in a thermal bath, as relevant for diffusive motion of bacteria cells embedded in a viscoelastic medium. In other words, does this fit parameter play all the roles that a proper temperature ought to play?

To gain insight into the relationship between the effective temperature and the diffusive motion of cells in a viscoelastic biofilm we take a closer look at the form of the effective temperature predicted in Risler et al, and at the fluctuation dissipation relation that relates temperature and diffusion.

3.2.2 Effective temperature

As mentioned above, Ranft et al [42] and Risler et al [43] studied cell migratory behavior due to death and reproduction, and have used an effective temperature formulation in order to recover fluctuation-dissipation like behavior. We use an effective temperature which agrees with theirs to leading order, but in this section I rewrite it in a different form for

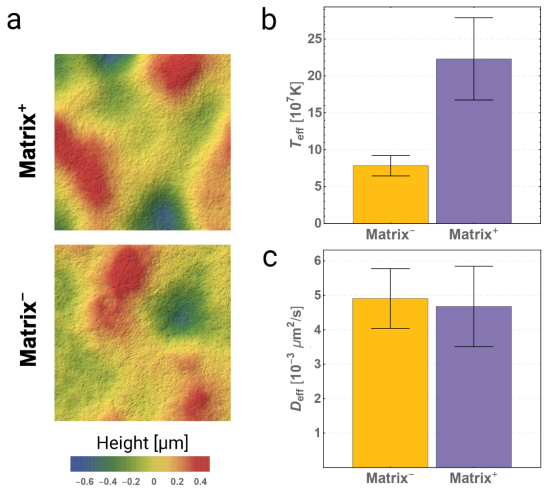

Figure 3.3: **a.** Demonstrative surface topographies of Matrix- and Matrix+ biofilm homelands measured via interferometry. **b.** While the topographies appear quite similar by eye, extracted effective temperatures (shown with standard error) are significantly different across many samples. **c.** However, diffusion constants calculated using the aforementioned effective temperatures and viscosities are nearly identical between Matrix- and Matrix+ samples.

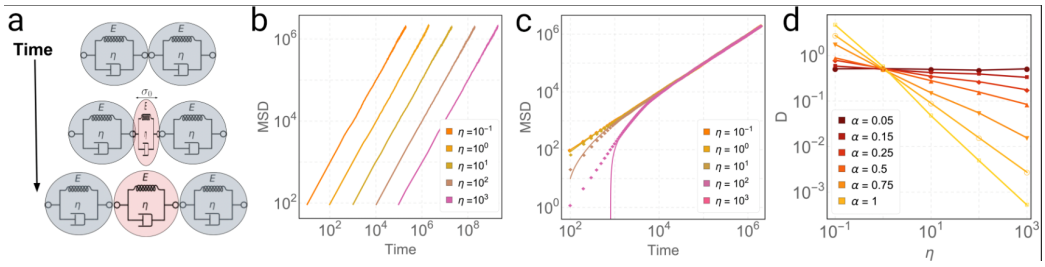

Figure 3.4: **a.** A visualization of the simulation setup. Cells are separated by Voigt-Kelvin elements and begin reproducing and lysing. Reproduction applies a stress σ_0 to neighboring cells. **b.** MSDs from simulations where $\alpha = 1$ (standard diffusion). **c.** MSDs from simulations where $\alpha = 0$ (free diffusion). The solid black line corresponds to an independent analytical prediction based on a generalized Langevin equation approach. **d.** Extracted diffusion constants as a function of viscosity from simulations with different values of α.

convenience. Ranft et al report an effective temperature that scales as

$$k_B T_{eff} \propto \frac{\lambda_{act}\eta}{\rho}, \tag{3.3}$$

with the cellular activity rate λ_{act}, the effective viscosity η, and the cell number density ρ. Previous work has focused on elastic cells that develop an *effective* viscosity due to the fluidization effect of activity. Here, we've used, as η, the measured viscosity of laboratory grown biofilms. Viscosity is nothing more than a material's energy density multiplied by a timescale associated with structural rearrangements [58]. We can write $\eta = \frac{u}{V}\frac{1}{\gamma}$, for an energy u, a volume of material V, and a relaxation rate γ. Next we can write the inverse cellular number density as $\frac{1}{\rho} = \frac{V}{N}$ for N cells. Combining these terms in equation 3.3, we have

$$k_B T_{eff} = \frac{\lambda_{act}}{\gamma} \cdot \frac{u}{N}$$

$$k_B T_{eff} = \langle E_{const} \rangle \cdot \frac{\lambda_{act}}{\gamma} \tag{3.4}$$

where $\langle E_{const} \rangle$ describes the average energy per constituent. For a passive material at equilibrium, the timescales associated with activity and structural rearrangement are equivalent (for example they might both arise from molecular collisions), $\lambda_{act} = \gamma$, and the mean energy per constituent follows from equipartition $\langle E_{const} \rangle \propto k_B T$ (up to a constant depending on the number of degrees of freedom of the constituent). Therefore at equilibrium for a passive material $k_B T_{eff} = k_B T$, as one would hope. In our experiments $\langle E_{const} \rangle$ is associated with cellular motion, and so T_{eff} measured in Kelvin is enormous compared to temperatures typically associated with atomic or molecular motion in daily experience.

3.2.3 Conventional diffusion and viscosity independent diffusion

The traditional Langevin equation for Brownian motion can be used to relate the effective temperature and the diffusive motion of cells here, as described for instance in [59]. We start by writing Newton's second law for a particle in one dimension subject to viscous damping and a force which is random in time, $R(t)$. The trajectory of a particle will therefore be stochastic; we are restricted to investigating probability distributions and averages over many particles' trajectories, each with different realizations of the random force $R(t)$.

$$m\dot{v} = -m\gamma v + R(t),$$

where $R(t)$ is random but has the following known properties:

$$\langle R(t) \rangle = 0$$
$$\langle R(t)R(t+\tau) \rangle = \kappa\delta(\tau)$$

where, in equilibrium for a passive fluid $\kappa = 2k_BTm\gamma$, the angled braces $\langle ... \rangle$ denote averages over many realizations, and $\delta(...)$ is the Dirac delta function. We follow a typical derivation to find the diffusion constant, except that we leave our solution in terms of T_{eff} instead of T. Again, for a passive fluid in equilibrium T_{eff} simplifies to T. Dividing through by m and letting $\xi(t) = \frac{R(t)}{m}$, yields

$$\dot{v} = -\gamma v + \xi(t),$$

which can be solved using standard techniques as

$$v(t) = v_0 e^{-\gamma t} + e^{\gamma t} \int_0^t dt' e^{\gamma t'} \xi(t')$$

Without loss of generality (at least when finding diffusion constants), we can set $v(0) = 0$ and $x(0) = 0$ then

$$v(t) = e^{\gamma t} \int_0^t dt' e^{\gamma t'} \xi t')$$
$$x(t) = \int_0^t e^{\gamma t'} \int_0^{t'} dt'' e^{\gamma t''} \xi(t'')$$

Squaring, taking the average over many solutions (i.e. for many realizations of the stochastic function ξ), and using the relation $\langle \xi(t)\xi(t+\tau)\rangle = \frac{2\gamma k_B T_{eff}}{m}\delta(\tau)$ yields (after much rearranging):

$$\langle v^2 \rangle = \frac{k_B T_{eff}}{m}(1 - e^{-2\gamma t}) \tag{3.5}$$
$$\langle x^2 \rangle = \frac{k_B T_{eff}}{2m\gamma^2}\left(2\gamma t - 3 + 4e^{-\gamma t} - 2e^{-2\gamma t}\right) \tag{3.6}$$

In the long-time limit this becomes

$$\langle v^2 \rangle = \frac{k_B T_{eff}}{m} \qquad \text{Equipartition} \tag{3.7}$$
$$\langle x^2 \rangle = \frac{k_B T_{eff}}{m\gamma} t \qquad \text{Diffusion} \tag{3.8}$$

As discussed above, eq 3.4 simplifies to $k_B T$ for a passive fluid at equilibrium. So replacing $k_B T_{eff}$ with $k_B T$ in eq 3.8 yields a textbook result (see appendix). This is because we've set the timescale for damping equal to the timescale associated with thermal kicks—γ appears in the noise strength as well as in the damping term. Also, the energy of each constituent is again set by the strength of thermal kicks, so that equipartition holds.

On the other hand, when the timescales governing the source of constituent motion and damping of constituent motion are separated, Einstein's classic results no longer necessarily hold. In our case, when considering active, reproducing but immotile, constituents embdedded in a viscoelastic medium, it is most natural to set the inverse damping timescale

γ to the viscoelastic relaxation rate $\frac{E}{\eta}$. The energy scale, however, is associated with cellular motions due to *active* kicks (i.e. step stresses from reproduction and death), and so we can write $\langle E_{const} \rangle = m \left(\frac{d\sigma_0}{\eta} \right)^2$, with cellular diameter d. The reproduction/death rate is identified with the activity rate λ_{act}. We then have

$$\begin{aligned}
\langle x^2 \rangle &= \frac{k_B T_{eff}}{m\gamma} t \\
\langle x^2 \rangle &= \frac{\langle E_{const} \rangle \lambda_{act}}{m\gamma^2} t \\
\langle x^2 \rangle &= \frac{m \left(\frac{d\sigma_0}{\eta} \right)^2 \lambda_{act}}{m \left(\frac{E}{\eta} \right)^2} t \\
\langle x^2 \rangle &= \left(\frac{d\sigma_0}{E} \right)^2 \lambda_{act} t \\
\langle x^2 \rangle &= \ell^2 \lambda_{act} t
\end{aligned}$$

Here $\ell = d\frac{\sigma_0}{E}$ is the change in length that the spring in the Voigt-Kelvin element of length d would experience instantaneously if subjected to a force σ_0. In other words, we can think of it as the "step-size" in a discrete 1D random walk, where steps are taken at a rate λ_{act}. The above is the long-time result. The equation we use to compare with simulations at all times is simply:

$$\langle x(t)^2 \rangle = \frac{\lambda_{act} \ell^2}{2\gamma} \left(2\gamma t - 3 + 4e^{-\gamma t} - 2e^{-2\gamma t} \right) \tag{3.9}$$

Comparison with simulations The diffusion of cells in our viscoelastic simulations aligns well with the predictions of a simple modification to the classic Langevin equation model for the Brownian motion of a particle: $m\frac{dv}{dt} = -m\gamma v + R(t)$. Here, γ is the inverse time scale associated with Stokes drag and $R(t)$ is a white noise term with zero mean and strength given by $\langle R(t)R(t+\tau) \rangle = 2m\gamma k_B T_{\text{eff}} \delta(\tau)$, $k_B T_{\text{eff}} = U_0 \lambda_{\text{act}} / \gamma$, where λ_{act} is the driving force activity rate, and U_0 is the energy scale of the driving force. When

λ_{act} is identified with the inverse time-scale associated with damping (γ) and the energy scale is set to $U_0 = k_B T$, then the ordinary form of viscosity-dependent Brownian motion is recovered. On the other hand, when γ is set to the viscoelastic relaxation rate (E/η), and the energy scale is associated with cellular motion $U_0 = m(d\sigma_0/\eta)^2$, with cellular diameter d, we find that this Langevin equation agrees numerically with our simulations, and predicts viscosity independent diffusion in the long time limit and (Fig. 3.4c).

To further compare the simulations and theory, we set the simulated cellular reproduction and death rate to be a function of E and η: $\lambda_{\text{act}} = \lambda_0 \left(\frac{E}{\eta}\right)^{\alpha}$ for a value of α between 0 (λ_{act} is totally independent of viscosity) to 1 (λ_{act} has the traditional dependence on viscosity). Theory predicts that $D \propto -\alpha$; indeed, this is observed for several values of α (Fig. 3.4D). It is worth noting how surprising it is to recover the theoretically expected scaling between D and α in simulations. The simulation is a viscoelastic mechanical model in which the only ingredients are death, reproduction and mechanical properties, and makes no explicit mention of effective temperatures or relaxation rates. Therein, we find that the mechanical properties play *no* role in how cells move around in the long time limit, i.e. how the diffusion constant scales, *unless* the rate of division and death is a function of those mechanical properties. And if the rate of division *is* set to be a function of mechanical properties, then the behavior of the diffusion constant in simulations is exactly as predicted by a theory that makes no explicit mention of viscoelasticity, mechanical properties, cell death, or cell reproduction. These represent two totally different approaches— mechanical and statistical— that yield the same result only when translated into each others language. This observation offers more evidence that the effective temperature is not simply a thermodynamic analogue but actually relates to kinetics and the mechanical energy of particles, the same way ordinary temperature does. Thus, viscosity independent diffusion appears to be a natural consequence when the driving force time scale arises from a separate physical process as the time scale of viscous damping.

Interestingly, the Langevin equation approach also predicts a diffusion constant, in the

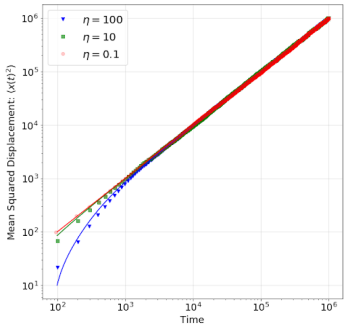

Figure 3.5: solid lines show the analytical predictions and markers are averages over many simulations (error bars negligibly small)

long time limit in 1D, $D = \frac{1}{2}\lambda_{\text{act}}\ell^2$. Here λ_{act} is the event rate, where events are lysis and reproduction, and ℓ is a characteristic length scale. A typical cell division rate for *V. cholerae* is 20 minutes, so in the homeostatic limit the event rate can be approximated as $\frac{1 \text{ event}}{10 \text{ min}}$. A typical cell length is about $1.0\,\mu\text{m}$, so putting together a "back of the envelope" prediction we find $D \approx 1.5 \times 10^{-3} \mu\text{m}^2 \cdot s^{-1}$, on the same order of magnitude as effective diffusivities extracted from colony topography and from tracer beads in Matrix- biofilms.

3.3 Initial conditions: the coffee-ring effect

Despite progress toward physical characterization of biofilms, an oft neglected point is their self-organizing nature. The overall architecture, shape, mechanical properties, phenotype distribution, and genotype distribution within a biofilm could all be dramatically affected by initial conditions. Or alternately, they could all be robust to initial conditions indicating a sort of teleology or "universal growth plan". However, before assessing the impact of initial conditions, one first must determine how biofilm initial conditions arise. This has proven difficult, due to the large number of relevant environments, substrates, and biofilm attachment strategies [60]. Biofilms are highly plastic and can be formed from a single founder cells and remain relatively clonal, or they can arise from whole populations comprising diverse microbial taxa[61]. Thus, we lack a unified picture informing how initial conditions affect biofilm development.

However, there is one exceedingly common system which produces tractable and repeatable initial conditions: a drying drop. A drop of rain, fresh water, or a sneeze aerosol can contain millions of microbial cells [62, 63, 64, 65]; when these drops dry on a surface, they will almost always leave these cells behind in a ring-shaped pattern. This phenomenon, known as the coffee-ring effect[66] [67] [68] [69], creates ring-shaped deposits of anything dissolved or suspended in a drop, from the oils in a cup of coffee [66], to colloidal particles [66] [67] [68] [69], to cells [70] [71] [72] [73]. A gradient in evaporation rate - lowest at the drop center, highest at the drop edge - drives a fluid flow from the center to the edge, carrying anything in the drop to the periphery [66][67][68]. When evaporation finishes, it leaves behind a deposit that is denser at the edge than in the interior. Cells deposited in the densely packed ring immediately interact with each other, while cells in the interior grow from sparser initial conditions. This coffee-ring-determined spatial variance of initial cell concentration may play a large role in mediating the local interactions between deposited cells, directly impacting fitness and biofilm structure. Further, along with natural occurrences, this effect is likely present in most laboratory experiments wherein agar slabs are inoculated with small drops of liquid culture 3.7.

In this section we explore two important paradigms of bacterial competitive behavior: “scramble” and “contest” [74][75]. The scramble scenario prioritizes gaining privileged access to nutrients and free space, whereas the contest scenario involves direct antagonism of competitor strains. Initial conditions can alter, or even totally determine, the outcome of both types of competitions. Interestingly, the coffee-ring effect spreads cells out to the edge of the drying drop–which we show plays a critical role in quickly acquiring territory during colony growth into free territory–but also packs cells densely in the ring–which we show affects density dependent processes like type VI killing [76] and quorum sensing [77].

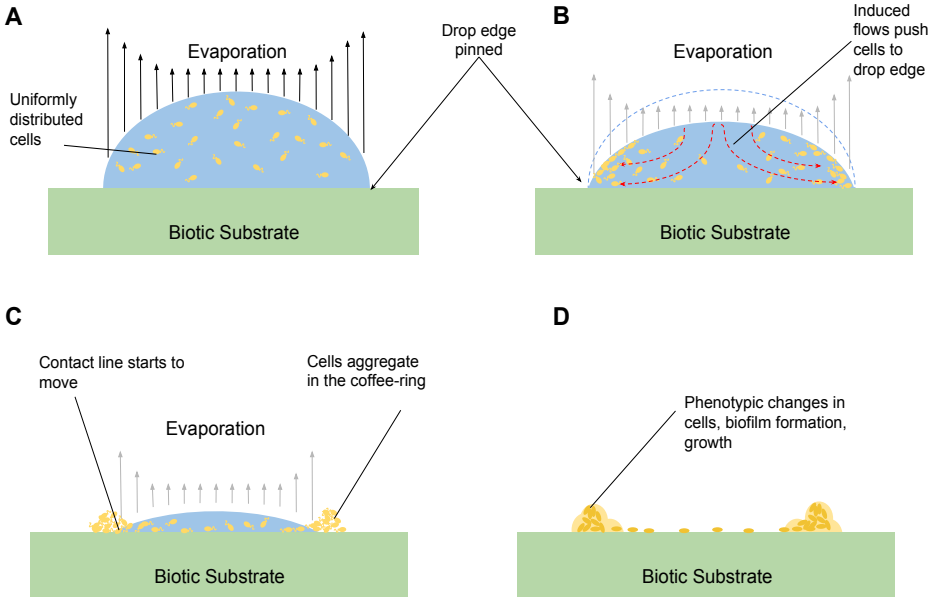

Figure 3.6: The coffee-ring effect deposits cells non-uniformly. **A** After a drop containing uniformly distributed microbes is deposited, the edge of the drop becomes pinned in place due to surface roughness. **B** Evaporation depletes fluid from the edge of the drop more quickly than the interior, inducing a fluid flow with its radial component directed outward from the center of the drop (dotted red lines). This induced flow carries along with it any suspended microbes, which are deposited at the pinned drop edge. **C** As evaporation continues the drop shape deforms, and the contact angle at or near the pinned drop edge becomes increasingly severe. Eventually surface tension overcomes the pinning force, and the contact line begins to move. The contact line may later become re-pinned, forming a new droplet of smaller radius. "This stick-slip" motion sometimes repeats several times before evaporation finishes. **D** In the end, cells are deposited at higher density in a ring-shaped build-up called the "coffee-ring". When deposited on a biotic substrate, cells are left to grow, divide, and otherwise carry on their usual business. However, the initial environment experienced by a bacterium in the coffee-ring differs from that experienced by his brother in the sparsely inhabited interior. Cellular behavior such as biofilm production might therefore be expected to vary by position.

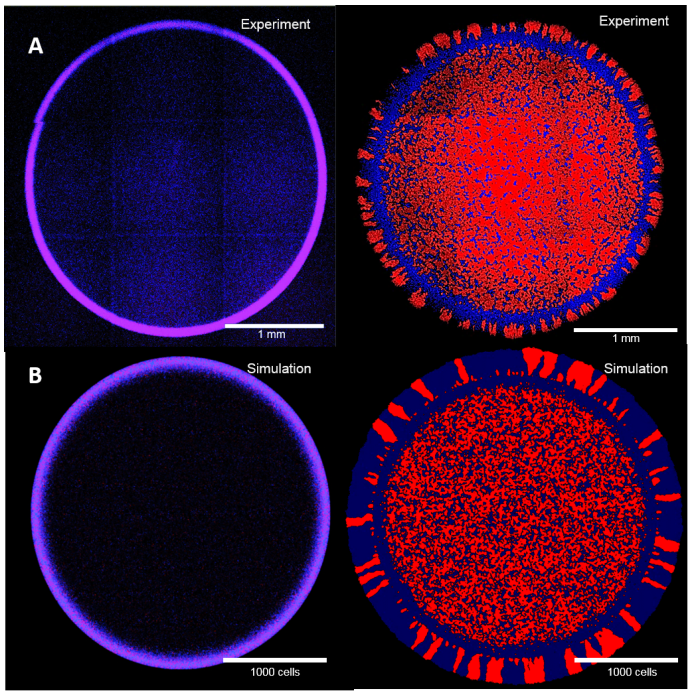

Figure 3.7: **A**: Left: Fluorescence image showing the distribution of the two strains 2 minutes after inoculation, just after the coffee ring has formed. Right: approximately 24 hours after inoculation. **B**: Left: Initial condition of the simulation. Cells were seeded randomly, according to the measured initial concentration profile $x(r)$ in (**B**), at 4:1 blue to red, matching the initial distribution in (**B**). The total number of simulated cells is approximately commensurate with the experiment (**B**). Right: Simulated biofilm after 75 timesteps. Simulation parameters used were $p_{bk} = 0.77 p_{rk}$, and $p_{bd} = 0.95 p_{rd}$.

3.3.1 Bacterial Coffee-Ring Effect

To understand intrabiofilm competition we performed experiments and simulations where agar plates were inoculated with drops of liquid culture containing two 'mutual killer' strains of *V. cholerae*. (see appendix for details). One strain is a 2-fold better killer, as measured by the number of surviving *E. coli* cells in a killing assay [34]. When the two strains compete with equal initial cellular numbers, the better killer totally dominates the competition; thus, we also gave the inferior strain an advantage in initial cell count (4:1 by number). After these drops dried, we imaged biofilms using brightfield and fluorescence microscopy, and observed clear coffee-ring deposits of cells (figure 3.7 A, left).

After 24 hours of growth from coffee-ring initial conditions, biofilms composed of two

mutually killing strains reproducibly exhibit three regimes of cellular arrangement (Figure 3.7 A, right, and Fig. 3.8.) In the interior of the biofilm, T6SS mediated warfare causes clonal phase separation, as described in [28]. On the biofilm periphery, outside of the blue annulus, cells undergo range expansion into uncolonized territory, also in clonal patches through a process known as "gene surfing" [78]. Surprisingly, while the frequency of the red strain with superior T6SS weaponry increases throughout in the center and in the range expansion, it actually decreases in the coffee-ring, leaving a blue ring.

To investigate the impact of coffee-ring initial conditions, we used a lattice individual based simulation (see appendix for details). Simulations seeded with spatially uniform concentrations do not replicate the three observed regimes ([28]–see SI Figure 2). However, a simulated biofilm seeded with the experimentally observed initial cellular concentration profile (Figure 3.7 B) showed the distinct morphological features of the experimental biofilm that had been incubated at 30° C for 24 hours (Figure 3.7, right).

To investigate how a strain with a lower growth rate, lower killing rate, or both, can drive its competitor to extinction in the coffee-ring, we performed further simulations to probe how the following parameters impact competition.

We first investigated the effect of the initial proportion of inferior killers, r_i, on competition outcomes. Simulations began with completely full square lattices randomly seeded with red and blue cells corresponding to different r_i (see e.g. the blowup in Figure 3.9 A); after $t = 100$, the final proportion of red cells, r_f depends logistically on the initial proportion (Figure 3.9 A). We tracked the proportion of red cells over time and declared the "winner" of the competition to be the strain which occupies more territory (which corresponds to cell number in a 2D lattice) at the end of the simulation. For example, for strains with equal killing and growth rates, the transition from one winner to the other occurs at a proportion of $r_i^* = 0.5$ (Figure 3.9, rightmost curve with triangles). This is unsurprising, as whichever strain has even a slight initial numeric advantage is expected to win this competition.

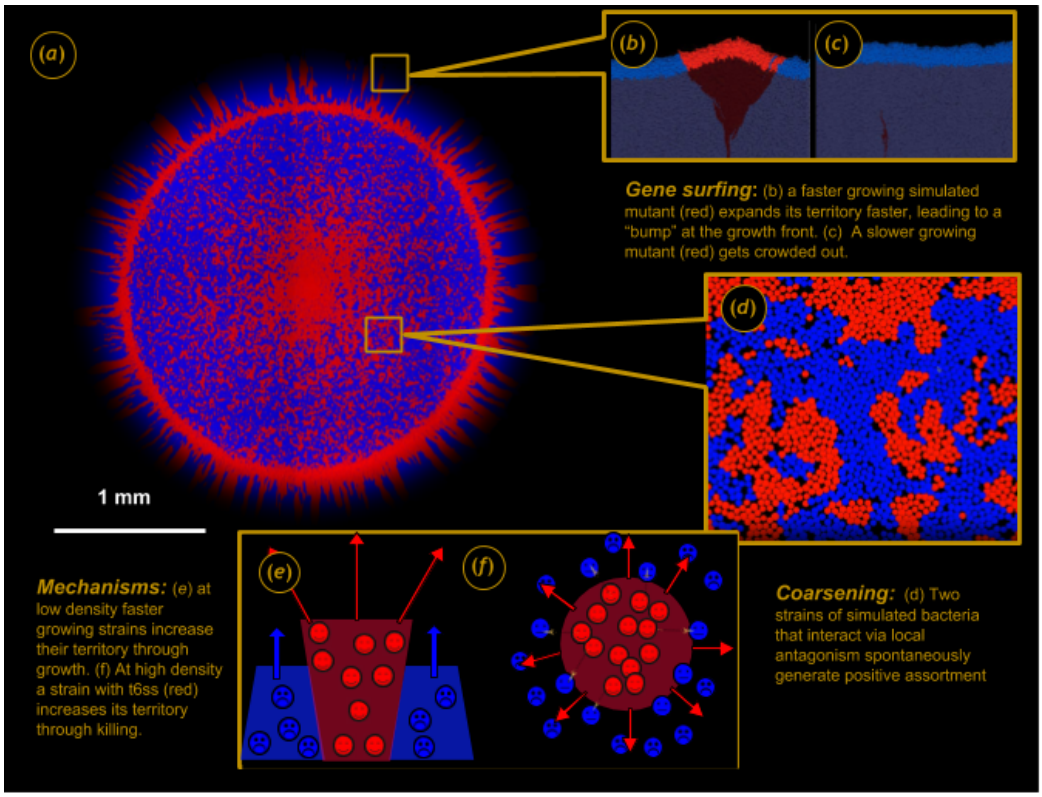

Figure 3.8: (a) A colony showing the three regimes of genetic structuring. (b) and (c) gene surfing. (d) clonal phase separation a la McNally et al [28]. (e) and (f) are cartoons explaining these mechanisms. The blue annulus arises due to the effect of initial conditions.

Next, we investigated the role of the red strain's relative kill rate, $k_R = \frac{\text{rate red kills blue}}{\text{rate blue kills red}}$, on competition outcomes. We again started with completely full lattices, but this time varied k_R, along with r_i. Varying k_R affects the transition proportion, r_i^*; increasing k_R shifts the entire trend to the left without otherwise effecting qualitative changes (Figure 3.7).

Finally, we investigated the effect of the overall initial cell density, x_0. The effect is readily visualized in Figure 3.9 D, where a competition was initialized with cell density decreasing from 100% (left) to 0% (right). Blue cells (an inferior killer that is initially more abundant: $k_R = 2$ and $r_i = 0.25$) fare better in initially high concentration regimes. Conversely, low initial cell density favors the strain with the killing advantage, even when it is initially out-numbered by a significant margin. This effect is quantified in Figure 3.9 B. Here, we generate a family of logistic curves like the one shown in Figure 3.9 A by repeating all of the simulations as described above, but seeded with a particular initial concentration of cells, x_0. For each data point, we discern the minimum proportion of red cells needed to win the competition, r_i^*, for a given k_R and x_0 (Figure 3.9 B). We find that large initial cell densities favor the strain with a numeric advantage, even though it has a significantly inferior killing rate (like the blue strain in Figure 3.9 D), while small initial concentrations of cells favor the strain with a killing rate advantage.

The mechanism behind this counter-intuitive density dependence can be understood by considering the local environment a cell experiences at early times. We measured the average **local** fraction of red cells ~ 1 time-step after the start of each simulation, $< \widetilde{r}_i >$, and plotted the value of $< \widetilde{r}_i >$ when red cells win the competition as a function of x_0 and k_R. This collapses the curves of Figure 3.9 B onto a single trend line. When a superior but outnumbered cell is deposited into a crowded area it is immediately confronted with its minority status, and any local frequency-dependent selection effects are likely to diminish its long term success. For example, even a strain that kills at twice the per-cell rate as its competitor is nevertheless at a competitive disadvantage if it immediately faces three times as many enemies within killing range. However, a superior but outnumbered

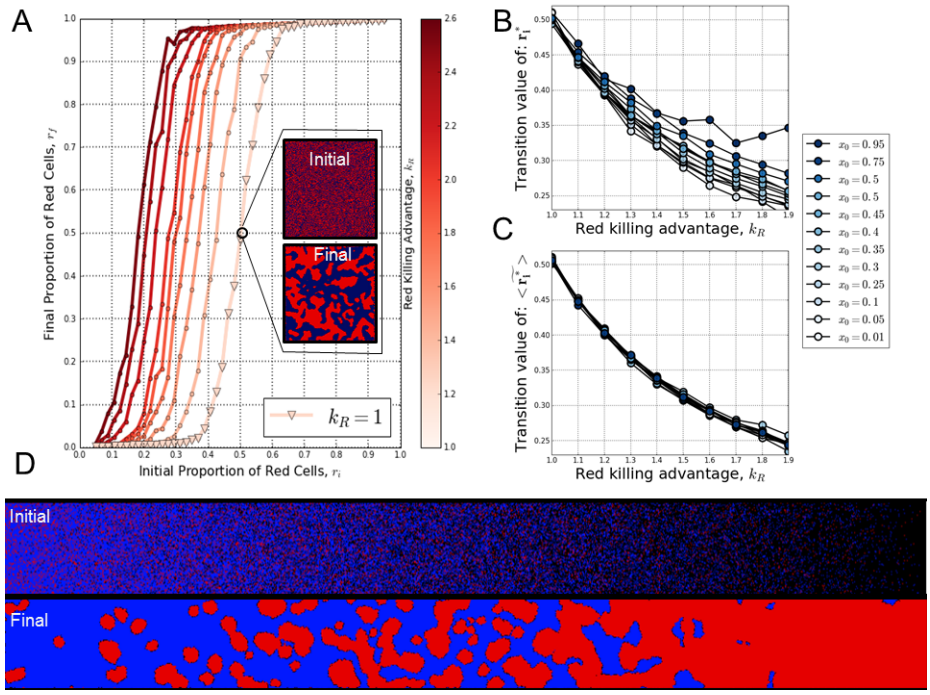

Figure 3.9: The coffee ring effect impacts bacterial competition in simulations. Caption continued on subsequent page.

cell that is deposited into a sparse area undergoes initially unimpeded clonal outgrowth and soon establishes a local majority wherein frequency dependent effects enhance its viability. Even if the global number ratio of red to blue cells is equivalent in a sparse or dense inoculate, differences in the local number ratio—ultimately the relevant parameter for local interactions—-can effect different outcomes.

3.3.2 Quorum Sensing

The above results demonstrate that the coffee-ring effect impacts density-dependent antagonistic competitions. Next, we investigated how the coffee-ring effect affects density-dependent gene regulation–via quorum-sensing. Quorum-sensing bacteria produce chemical signals that can be sensed by nearby bacteria, thus altering their gene expression and behavior [77]. Quorum-sensing is quite common[79] and is thought to be a crucial social trait underlying cooperation and conflict in bacterial biofilms [80].

To determine whether coffee-ring initial conditions have an impact on timing and het-

Figure 3.9: The coffee ring effect impacts bacterial competition in simulations. **A** The final proportion of red cells, r_f, after a 100 generation competition between red and blue cells in a square lattice of size 400^2 cells, depends logistically on the initial proportion of red cells: $r_f = \frac{1}{1+e^{(-\beta(r_i - r_i^*))}}$. r_i^* can be understood as the initial proportion of red cells required to "win" the competition. Varying k_R changes the relative rate of killing between the two strains, and affects r_i^*. This is plotted in **A** as solid lines representing the variation of k_R, from $k_R = 1$ (far right curve with triangles) to $k_R = 2.7$ (far left curve in red with circular markers). The blowup shows an example of the type of simulation from which r_f is extracted, in this case $(r_i = 0.5, r_f = 0.5)$. r_i^* decreases as k_R increases; it takes fewer red cells initially to win the competition if each red cell is more competitive. The effect of varying the overall initial concentration of cells (of both types), x_0 is visualized in **D**, where a simulation was seeded with cells where blue outnumbers red 4:1 throughout ($r_i = .25$), but red is twice as effective at killing, ($k_R = 2$), but where x_0 varies from 1 at the far left where all the sites are occupied by cells initially to 0 at the far right where all the sites are initially empty. The state of the simulation after 100 generations is shown on the bottom. **B** quantifies this effect. The darkest circles were generated from the family of curves shown in **A**, while the rest of the data in the top panel of **B** were generated in a similar manner. As x_0 decreases, for a given r_i and k_R, the individually superior but outnumbered strain fares better. These curves collapse if we plot against the variable $< \widetilde{r_i^*} >$, **C**. Whereas r_i describes the global proportion of red to blue cells throughout the entire lattice at time zero, $\widetilde{r_i}(x, y)$ describes the initial[†], *local*[‡] proportion of red to blue cells at a position in the lattice (x, y). Taking a spatial average yields $< \widetilde{r_i} >$, the transition value of which is $< \widetilde{r_i^*} >$.

[†] In fact $\widetilde{r_i}(x, y)$ is measured at early but non-zero time ($t = 0.2$ generations).

[‡] Here, by local we mean the nine-automaton neighborhood centered at (x, y).

Table 3.2: The mean brightness ratio, $\langle b \rangle$, and variance in brightness ratio, $\langle b^2 - \langle b \rangle^2 \rangle$, for a population of 14 wild type biofilms and 12 bright strain biofilms.

Wild Type	Bright Strain
$\langle b \rangle = 1.773$	$\langle b \rangle = 1.453$
$\langle b^2 - \langle b \rangle^2 \rangle = 0.203$	$\langle b^2 - \langle b \rangle^2 \rangle = 0.023$

erogeneity in gene expression, we inoculated agar plates with three strains of *V. harveyi*. The expression of bioluminescent luciferase in *V. harveyi* is regulated by a self-produced transcription factor [81]. At high densities, this produces visible bioluminescence, making these organisms ideal for studying the effects of initial conditions on gene expression in biofilms. In a preliminary trial, we inoculated agar plates with three strains of *V. harveyi*. One strain is a wild-type isolate that exhibits quorum-sensing-dependent bioluminescence. Another strain is 'dark;' it is a *lux-O* mutant that is unable to sense its own autoinducers and therefore does not produce luciferase. The final strain is 'bright;' it is a **lux-R** mutant that constitutively expresses luciferase, i.e., whether or not there is a quorum present. After incubating colonies of each of these strains at 30° C on LB agar for ~ 2 hours we photographed them in a dark room and analyzed the brightness distribution in bright and wild-type strains and calculated a "brightness ratio" as the mean bioluminescent brightness in the coffee-ring region divided by the mean brightness in the interior.

Wild-type colonies show a larger variance in brightness ratio, as well as a larger mean (Table 3.2). This difference was statistically significant ($p < .05$) when compared using a one way f test: (f-statistic = 5.11, p=0.033, N = 26. Bright-type cells produce the same amount of luciferase independent of location in the colony, but they typically still have a brightness ratio > 1 due to the simple fact that there are still more cells per unit area in the coffee-ring than in the interior. Therefore the bright-type brightness ratios can be used as a control population to represent the null-hypothesis that there is no change in relative light emitted per cell between the interior and coffee-ring of a colony, and that any deviation in the brightness ratio from 1 comes *only* from cell distribution in a colony.

We found significant evidence to reject the null, suggesting that the increased mean in

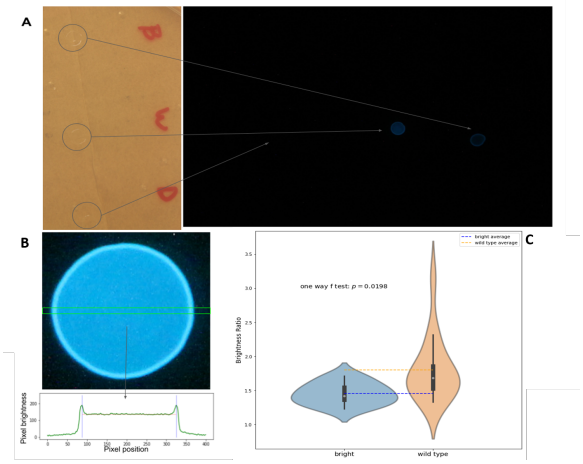

Figure 3.10: The coffee ring effect impacts quorum sensing. Caption continued on subsequent page.

the wild-type population can be attributed to changes in the relative brightness per cell in different locations of the colony. This implies changes in gene-expression; cells of wild-type that are deposited in the coffee-ring sense increased cell density through quorum sensing, and so initially produce more luciferase per cell than cells in the interior of wild-type colonies. The difference in colony morphology described above would tend to *increase* the brightness ratio of the bright-type strains, which means that the effect of the coffee-ring on quorum sensing in the wild-type strains is even stronger than suggested by the brightness ratios shown in figure 3.10.

3.4 Conclusion

Through experiments, simulations, and theory, we show that diffusion mediated by death and reproduction is independent of viscosity. This surprising result arises from the separation of the origin of viscous relaxation and driving force time scales. Reproduction and death events induce step-strains that, in turn, induce stresses. These stresses relax much more rapidly than the time between step-strain events, making the material essentially a memory-less fluid on long time scales. The accumulated motion that a cell undergoes as a result of these strains amounts to a random walk governed entirely by the active driving

Figure 3.10: The coffee ring effect impacts quorum sensing. A: (Bottom) Image of three colonies of *V. harveyi* growing on LB agar in a petri dish. The colonies are labeled B for "bright", W for "wild type", and D for "dark". Colonies are formed by dropping 2 microliters of overnight culture onto the agar. The cultures were normalized to uniform optical density prior to inoculation. Colonies are then incubated for 2 hours at 30O C before being photographed. : (Top) Immediately after photograph in the bottom was taken, the dish was taken to a dark room for high exposure photography (30 second exposure with F-stop = 4.0 and ISO = 3200 on a Canon EOS Rebel SL1). The vast majority of light collected in the photograph on the right originates from luminescent emission of luciferase in the colonies rather than scattering, which is why the dark strain does not appear here. B Another plate with wild-type and bright strains. When conducting our brightness ratio assays the positions within the petri dish of the bright and wild type colonies were randomized to control for any position-dependent effects such as access to nutrients or moisture. D (top) Overall brightness was calculated along a ten pixel wide strip across the midline of each colony, indicated by the green rectangle. Brightness in the strip was averaged across all three color channels and across the ten pixels of the width of the rectangular strip and the resulting intensity profile is plotted as a function of pixel x position (bottom). These profiles show two peaks in brightness corresponding to the position of the coffee-ring The brightness ratio for each colony was calculated as the mean brightness at the peaks divided by the mean brightness in the interior. C shows a violin plot of the brightness ratios for all of the bright type colonies on the left and all of the wild-type colonies on the right. These distributions have a statistically different mean p¡.05, suggesting that the coffee-ring effect enhances production of luciferase. Initial conditions affect bacterial gene expression well into the development of a biofilm. E Two simulated images that have brightness ratios representative of the bright and wild type strains, respectively.

force.

Furthermore, this cellular diffusive behavior can be captured by an effective temperature that relates to macroscopic observables — namely the presence of a quantitative relationship between surface topography and cell death. This relationship opens new avenues for studying both physical and biological properties of biofilms. Just as measuring fluctuations in equilibrium materials permits the calculation of mechanical response functions [39], mechanical and structural measurements of biofilms and tissues can be used to infer death and reproduction ratesquantities that are difficult to measure in densely packed cellular solids.

We find that death and reproduction mobilize cells within biofilms; cells travel their own length in 40 minutes. While this motion is not fast, it allows biofilms to constantly modify their structure, and explore new configurations which could be beneficial (or detrimental). The mechanical properties of biofilms are critical for many biological properties [82]; the independence of cellular diffusive motion – important for biofilm growth and remodeling – on biofilm mechanics suggests that biofilm viscoelasticity can vary without incurring a trade-off with regards to cellular diffusion.

While cell death and reproduction actively remodel biofilms even in a state of zero net growth, the microstructure of these communities (and thus the macroscopic mechanical behavior) is also sensitive to initial conditions and early growth. We highlight this sensitivity using the coffee ring effect.

When a drop dries, it deposits bacteria in a ring shaped pattern through the coffee-ring effect. Using bacterial model systems, we show how the deposition of cells in the classic 'coffee ring' pattern changes bacterial competitions and gene expression - thus impacting ecological and evolutionary outcomes. This has fundamental implications for understanding the spatial ecology of microbes. We anticipate the coffee-ring effect will be relevant to a broad swath of microbes that possess frequency and density dependent interactions.

CHAPTER 4
HACKED INTERNET CONNECTED VEHICLES POSE CYBERPHYSICAL RISKS

4.1 Introduction

When we talk about active matter physics, we usually refer to the individual constituents (cells, birds, or even humans) as "particles." Treating such complicated entities as atomic "simples" and offloading system complexity onto (often deterministic) interactions between them amounts necessarily to a simplified and abstract representation, but nevertheless often captures most of the important dynamics. When dealing with human behavior we need to be particularly careful. Obviously ignoring free will significantly simplifies our analyses, but humans only behave like particles under certain circumstances. Our collaborator Jesse Silverberg has expertise in identifying the boundaries of these circumstances, and developing appropriate active matter models. For example, in the physics of mosh pits and crowds [83] there are some regimes where humans behave like, well, *humans*, while there are other regimes where humans behave like particles subject to the social forces that govern pedestrian traffic. There is even a certain crowd density where the physicality of the human body dominates behavior and people just bounce off of each other subject to actual physical forces. With his expertise in modeling human social forces in pedestrian traffic, he naturally pivoted to an interest in vehicular traffic. Could an active matter model of vehicular traffic add anything to our understanding of vehicular traffic? In particular, it seems inevitable that there is an opportunity to uncover "new physics" with the advent of new types of drivers— fully autonomous computer drivers.

It turns out there *is* a lot that physicists can still offer, but there is also already an enormous literature on modeling vehicular traffic flow [84]. Before we return to active

matter physics and self driving cars, it is important to give an overview of what is already known about the physics of human vehicular traffic.

4.1.1 Organization

In section 4.2 a brief overview of the very basic empirical facts about traffic flow is presented along with a bit of relevant history. Next, section 4.3 covers some well known and successful models of traffic flow, including one developed by Jesse Silverberg (along with Skanda Vivek, myself, and Peter Yunker). I will use this model to highlight some general features of traffic flow that are made plain by all successful traffic models. One key result is that stop-and-go traffic, or so called "phantom traffic jams" arise -in all models- as an inevitable result of our human limitations as drivers. Finally, section 4.5 discusses some of the traffic flow benefits and cyberphysical risks of introducing autonomous vehicles into our roadways.

4.2 Basic empirical facts of traffic flow

There are obviously many empirical facts of traffic flow, even in the absence of bottlenecks, intersections, and other complications. For a thorough review, see for example Helbing [84]. However, there are a few key features of traffic flow that are especially relevant to this work and which every successful traffic model should recapitulate.

Fundamental Diagram

A question that immediately arises for civil engineers and urban planners is " how many vehicles per unit time can flow on this roadway?". Since the flux of vehicles is such a crucial quantity to be able to understand and predict, and also since it is and has been quite easily measurable for some time, the relationship between flux and vehicle density was established relatively early. It is known as the "fundamental diagram" of traffic flow. The very old-fashioned way to measure flux, interestingly, was to lay a hollow rubber pipe

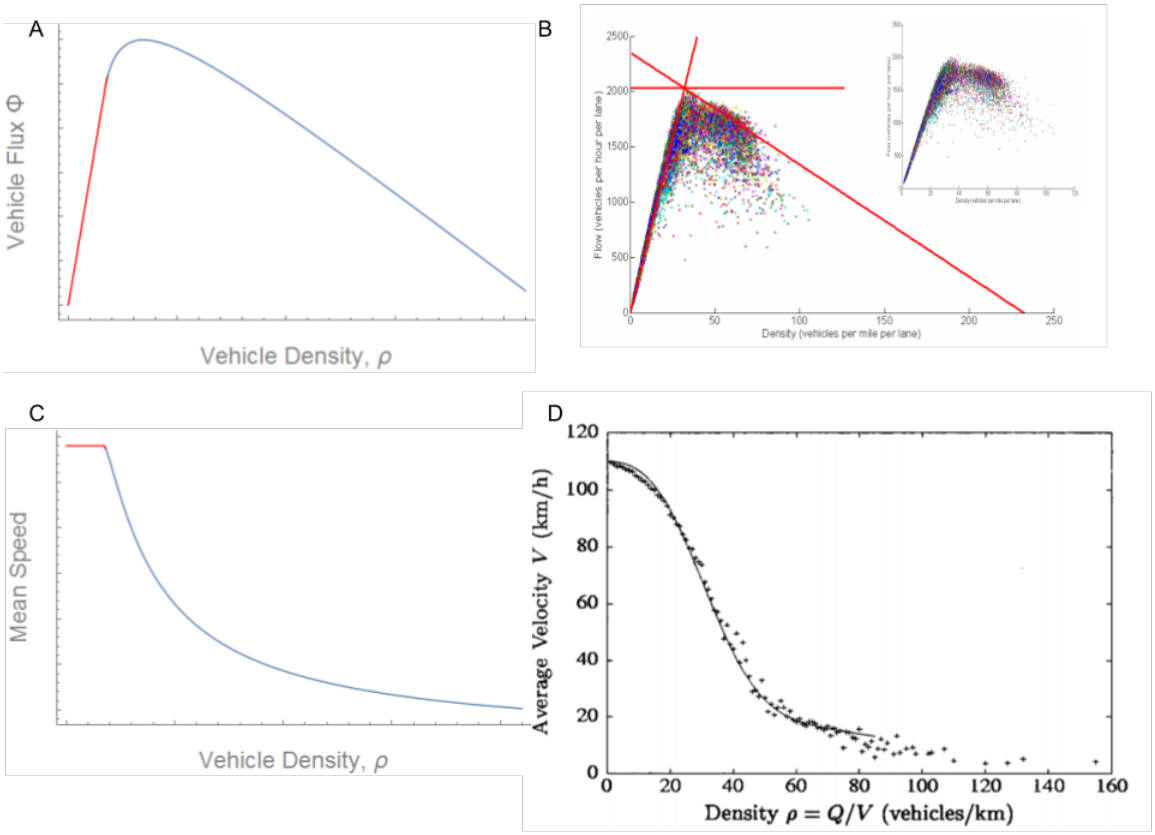

Figure 4.1: A) Schematic of flux vs density fundamental diagram of traffic flow, and C) mean speed vs density. B) Real data from 92 days of traffic flow on I880 near San Francisco, published in [85]. D) Empirical velocity vs density relationship from traffic flow on a freeway near Amsterdam, published in [86].

across a roadway with a mechanical counter positioned near either end. When a car drives over the rubber, a rush of air shoots out and triggers the mechanical counter. These days a single induction-loop counter is typically used. By counting the number of vehicles passing and simultaneously keeping track of time, flux can be measured, $\Phi = \frac{N}{t}$, the number of vehicles per unit time.

There are a several traffic flow regimes visible in the fundamental diagram. First, at low densities, the flux Φ is linear in the density ρ. In this regime (red part of figure 4.1 A), everybody on the road is travelling as fast as they would like and flux increases linearly as you add more cars. Next is a region of synchronized flow where the density of cars is quite

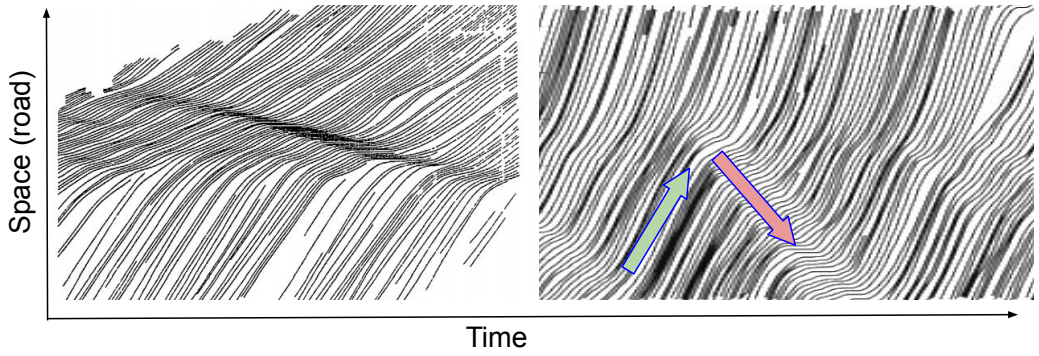

Figure 4.2: Left: vehicle trajectories extracted from aerial photography of two urban roadways in Columbus Ohio circa 1975 [88], figured modified from [87]. Right: vehicle trajectories from a simulation of traffic flow using the SVYY traffic model. Green arrow indicates the direction of traffic flow along the road. Red arrow indicates the direction of propagation of a phantom traffic jam.

large yet everyone is still travelling quite fast. This corresponds to the peak Φ in figure 4.1 A. In fact, this situation rarely occurs for very long and the curve of the fundamental diagram acts more like an upper bound, with most real traffic flowing at significantly lower Φ, as shown in figure 4.1 B. It is in this regime that we typically observe the "Phantom traffic jams" discussed in the next section. Finally, at very high densities Φ drops to near zero in the bumper-to-bumper standstill we all know and love.

"Space-time" diagrams and "Phantom traffic jams"

With modern video-tracking capabilities it is possible to easily track the position of every vehicle on a stretch of highway as a function of time. When we do so, we can visualize a so-called "space-time" curve. Nagel and Schrekenberg [87] relied heavily on these visualizations in their seminal cellular automata model of traffic flow. Figure 4.2 shows a space-time diagram for real traffic as well as a space-time diagram generated by simulated vehicle trajectories in heavy synchronized traffic flow, near the peak of the fundamental diagram.

Space-time diagrams make apparent the phenomenlogy of "phantom traffic jams". Each line on the diagram represents a single vehicle's trajectory, and as such each line should al-

ways maintain a non-negative slope. Furthermore, lines should not intersect; that would typically correspond to an accident, although on multi-lane roads it could simply be one car passing another. For this reason these diagrams should always be made for a single lane. The phantom traffic jam phenomenon is indicated by a red arrow in figure 4.2 on the right; a wave of slow-moving flow spontaneously appears and grows in size as it travels "upstream". These traffic waves have been studied extensively, and have even been suggested as evidence of self-organized criticality [89]. The salient point for this work is that they tend to reduce overall traffic flow and that they arise spontaneously "out of the nothing". Furthermore, they can act similar to nucleating sites for larger more catastrophic traffic jams in which mean velocity drops almost to zero for miles at a time.

4.3 Traffic flow models

To understand traffic waves and the fundamental diagram (among other aspects of traffic flow), a few broad categories of traffic models have been proposed and adopted by the engineering community. It has been suggested that over 100 traffic models have been developed [84], but they are mainly variations on one of four themes: macroscopic fluid-dynamic models, mesoscopic gas-kinetic models, microscopic car following models, and cellular automaton rule-based simulations. Of these, cellular automata and microscopic models have most recently been dominant. Microscopic models are considered the most realistic and richest in terms of capturing human driving behavior, while cellular automata are simple and, when properly implemented, generate extremely versatile simulations blazingly fast. As such, cellular automata are often used by engineers interested in evaluating flow in large complicated traffic networks.

4.3.1 Cellular automata models

Originally conceptualized by Von Neumann and others and later popularized by Stephen Wolfram, a cellular automaton generally consists of a grid of cells occuring in some particu-

lar state within a finite state space, that is evolved according to an unchanging deterministic update rule. Wolfram's automata were remarkable for being able to generate rich behavior ranging from fixed points, periodic states, and outright chaos from such a simple set of fixed rules. Traffic cellular automata on the other hand, are almost the opposite. They rely on inherent stochasticity and generate a fairly consistent phenomenology under a broad range of update rules and initial conditions. Nonetheless, they count as stochastic cellular automata. In any event, they are in widespread use now, and shed light on the important microscopic ingredients in any successful traffic model. Furthermore, we validate all of our results in this work with multiple traffic models and multiple overall modeling approaches, including the Nagel-Schrekenberg cellular automata model.

The Nagel-Schrekenberg cellular automata model is the paradigm for traffic cellular automata, was introduced by Nagel and Schrekenberg in 1992 [87], and consists of a very simple set of rules, which I'll quote directly:

"

- **Acceleration**: if the velocity v of a vehicle is lower than v_{max} and if the distance to the next car ahead is larger than $v + 1$, the speed is advanced by one $[v \rightarrow v + 1]$.
- **Slowing down (due to other cars)**: if a vehicle at site i sees the next vehicle at site $i + j$ (with $j < v$), it reduces its speed to $j - 1$, $[v \rightarrow j - 1]$.
- **Randomization**: with probability p, the velocity of each vehicle (if greater than zero) is decreased by one $[v \rightarrow v - 1]$.
- **Car motion**: each vehicle is advanced v sites.

"

Each site is a fixed length d_s, and usually periodic boundary conditions are used. In this work, we performed simulations corresponding to two different cell lengths, 4.5 and 7.0 m respectively. The maximum velocity of vehicles are in units of d_s m/s, where d_s is the cell

length. For a 1000 m road, these distances correspond to ≈ 143 and 222 sites. Additionally, we set the maximum velocity v_{max} to 7 units per time step, which translates to 29 m/s (65 mi/h).

4.3.2 Microscopic models

Microscopic models typically couple a given car to the car in front of it, and so they are called "car following models". The basic idea is to treat the interactions between cars as forces, and the cars themselves as particles without any agency aside from dutiful reaction to these forces. Such a force-based approach to social interactions has been quite successful not only in vehicular traffic modeling but also flocking behavior, human pedestrian traffic, and in self-driven many particle systems in general [90, 83].

The car-following models all need at least two ingredients, which are similar in nature to the first two rules of the Nagel-Schrekenberg cellular automaton model: a term that induces acceleration along the roadway and a term that causes slowing down to avoid collisions. The basic form of car-following models then, for the n^{th} car, is

$$\frac{d}{dt}v_n(t) = h_n(t) + \frac{g_n(v_n(t))}{\tau} + F^{\text{repulsive}}_{n,n+1}(t) \tag{4.1}$$

$F^{\text{repulsive}}_{n,n+1}(t)$ should be negative and prevents collisions, $g_n(v_n(t))$ should be a positive term that propels cars toward a preferred speed, and $h_n(t)$ captures everything else, including noise. Notable examples of this type of model are the "optimal velocity model" [91], as well as the two models covered below: the "intelligent driver model" (IDM) [92, 93] and the Silverberg-Vivek-Yanni-Yunker (SVYY) model.

Intelligent Driver Model

The intelligent driver model is perhaps the capstone of traffic modelling in terms of capturing driver behavior. It is free of accidents (which cannot be said of the optimal velocity

model or the SVYY model), it reproduces realistic microscopic behavior like acceleration and braking times as well as macroscopic behavior like the fundamental diagram, and it has enough parameters to be flexible enough to fit to real traffic quite well. Its only weaknesses as a research tool are that it contains several fit parameters, some of which have no apparent physical meaning, and is unwieldy to work with analytically.

The rules for IDM simulations are:

$$\begin{aligned} \dot{x}_n = \frac{dx_n}{dt} &= v_n, \\ \dot{v}_n = \frac{dv_n}{dt} &= a\left[1 - \left(\frac{v_n}{v_0}\right)^{\delta} - \left(\frac{s^*(\Delta v_n, v_n)}{s_n}\right)\right], \\ s^*(\Delta v_n, v_n) &= s_0 + v_n T + \frac{v_n \Delta v_n}{2\sqrt{ab}}, \end{aligned} \tag{4.2}$$

where x_n and v_n denote the position and velocity of the n^{th} vehicle, and s_n is the distance between n^{th} vehicle and the vehicle in front of it on the same lane. We choose parameters [93]: $v_0 = 120$ km/h is the velocity a vehicle would drive in free traffic; $s_0 = 2$ m is the minimum acceptable gap maintained from the front bumper of one car to the rear bumper of the car in front of it in dense, standing traffic [94]; $T = 1.6$ s is the minimum possible time for a vehicle to reach the current position of the vehicle in front of it; $a = 0.73$ m/s^2 is the maximum acceleration; $b = 1.67$ m/s^2 is the comfortable deceleration. The exponent δ is a fit parameter and describes how quickly cars accelerate from a stopped position with open road ahead of them. In all of our simulations we have used the value $\delta = 4$.

4.3.3 The Silverberg Vivek Yanni and Yunker model

The final model to introduce is one proposed by Jesse Silverberg and subsequently developed by Skanda Vivek, myself, and Peter Yunker.

We chose a force-based approach[83, 95, 96] that represents each vehicle by their posi-

tion x at time t on a straight road of length L. The main appeal of this type of model is the rich complexity of interesting collective behavior that can be generated by its simple set of equations and correspondingly small set of parameters. The position of each vehicle is evolved using a self-propulsion force $F^{\rm propulsion}$, and a repulsive collision-avoidance force $F^{\rm repulsion}$ according to

$$\begin{aligned} \ddot{x} &= F^{\rm propulsion} + F^{\rm repulsion}, \\ F^{\rm propulsion} &= \tau_\alpha^{-1}(v_\alpha - \dot{x}), \\ F^{\rm repulsion} &= \begin{cases} \epsilon_\alpha \left(1 - \delta x/R\right)^{3/2}, & \delta x < R \\ 0, & \text{otherwise} \end{cases} \end{aligned} \tag{4.3}$$

where $\dot{x}$ and $\ddot{x}$ are the velocity and acceleration of a given vehicle. Each vehicle has a preferred speed v_α and a characteristic response time τ_α that it takes to equilibrate to this speed. In the limit of a single vehicle without interactions, $F^{\rm repulsion} \equiv 0$ and direct integration shows $\dot{x}(t) = v_\alpha(1 - e^{-t/\tau_\alpha})$. As the number of vehicles increases and they begin to interact, the repulsive force slows a given vehicle down as it approaches another vehicle from behind. The strength of this force increases smoothly from zero as the vehicle-vehicle separation δx becomes smaller than the interaction threshold distance $R = (29\ \mathrm{m/s}) \cdot (2\ \mathrm{s})$. This threshold models the 2-second rule on highway-like conditions, which states a minimum safe distance between two vehicles is the distance traveled during 2 seconds at typical speeds of 29 m/s (65 mi/h). The functional form of the repulsion force in Eqs. (4.3) follows from the compression of two elastic spheres[97], and only applies to the trailing vehicle, as drivers respond to traffic ahead of them more strongly than behind (if at all). Under these conditions, we balance propulsion and repulsion forces when two vehicles are bumper-to-bumper, and set $\delta x = r \equiv 4.5$ m as the typical size of a vehicle to find $\epsilon_\alpha \equiv [(29\ \mathrm{m/s})/\tau_\alpha](1 - r/R)^{-3/2}$. Thus, the distance between vehicles δx is always larger than the size of a vehicle r, but the interaction between vehicles is only experienced when $r \leq \delta x < R$.

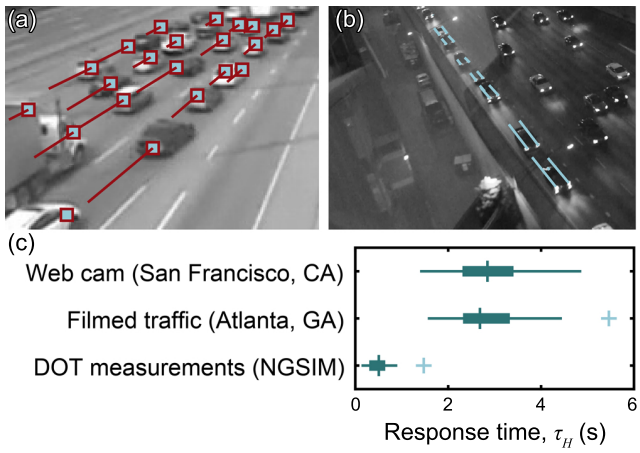

Figure 4.3: Empirical measurements of a human-driven vehicle's response time τ. (a) A live streamed web cam provides daytime video data on traffic flow (northbound 101 at N 1st street, San Francisco/Oakland Bay, CA). Individual vehicles (squares) and their trajectories (lines) illustrate measurements of $x(t)$. (b) Nighttime highway traffic was filmed and analyzed using the same methods (southbound I85 exit 249C, Atlanta, GA). (c) Fitting velocities during stop-and-go motion allows for measurements of the human-driver response time τ. Box-and-whisker plots show the median value, data quartiles, and outliers (+).

The only remaining free parameter in the equations of motion for human-driven vehicles is the response time τ, which generally varies from 0.5 s to several seconds, depending on attentiveness, driving conditions, visibility, and level of distractions. To empirically measure τ, we analyzed three sources of driving data including a highway webcam [Fig. 4.3(a)][98], digital footage we recorded [Fig. 4.3(b)], and previously published Department of Transportation (DOT) traffic data from Los Angeles, California (southbound US 101; NGSIM June 15, 2005, 7:50 to 8:05 am)[99, 100, 101]. By measuring the velocity in "stop-and-go" traffic and assuming the repulsion force is negligible during the initial "go," we could fit this data to $\dot{x}(t)/\dot{x}(t_f) = 1 - e^{-t/\tau_H}$ resulting in measurements of τ [Fig. 4.3(c)]. In higher-density traffic, we observed drivers tend to accelerate over longer periods of time, whereas in lower-density traffic, drivers tend to react faster. Because Eqs. (4.3) simplifies driver response time to be density-independent, we set $\tau = 2.0$ s, which comes from the average of empirical measurements that were found to be (2.0 ± 1.4) s.

In simulations with $N = 100$ human-driven vehicles on an $\ell = 1$ lane road, $L = 1.0$ km long, we find a brief transient regime that lasts for ≈ 500 integration time steps, followed by steady-state dynamics. Superimposed on this 1D line of traffic, we observe backwards-propagating density waves known as "phantom traffic jams" that cause stop-and-go motion of individual vehicles [Fig. 4.4a]. This emergent collective phenomenon has been extensively studied in other models of vehicle traffic[84, 102, 103, 104, 93, 105, 106], and has been discussed above. Here, we see these density waves as an important validation of our active matter model, as their spontaneous emergence indicates broad consistency with the known phenomenology of vehicle traffic.

MOBIL Lane Changing Rules and the Fundamental Diagram

Going beyond one-lane simulations and reproducing essential features of multi-lane traffic where $\ell > 1$ requires a model for lane changing behavior. Otherwise, quantitative metrics of traffic flow would be dominated by the slowest moving vehicle. One method for realistically capturing these dynamics is the Minimizing Overall Breaking Induced By Lane changes (MOBIL) framework[107, 92], which offers a simple force-based rule to determine when a vehicle should change lanes. Specifically, MOBIL considers whether a vehicle and its neighbors would better match their preferred speeds if a given vehicle changes lanes. Defining the change in acceleration post-lane-change between the next time step $t + 1$ (after the lane change) and the current time step t (before the lane change) as

$$\begin{aligned} \Delta\ddot{x}_i &= \ddot{x}_i(t+1) - \ddot{x}_i(t), \\ \Delta\ddot{x}_{i-1} &= \ddot{x}_{i-1}(t+1) - \ddot{x}_{i-1}(t), \quad \text{and} \\ \Delta\ddot{x}_{j-1} &= \ddot{x}_{j-1}(t+1) - \ddot{x}_{j-1}(t), \end{aligned} \tag{4.4}$$

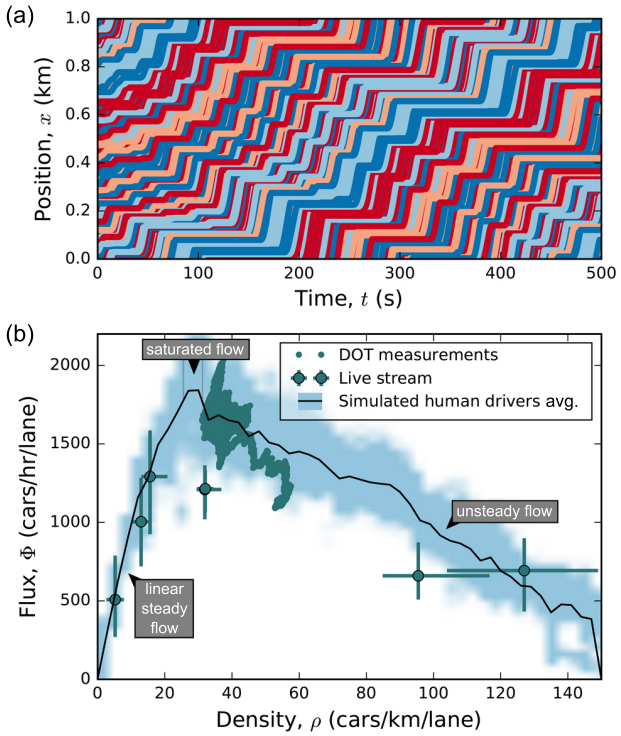

Figure 4.4: Simulations of human-driven vehicles using Eq. (4.3) reproduce empirical data. (a) Trajectory plots of $N = 100$ simulated human drivers on a $L = 1$ km, $\ell = 1$ lane road. Each colored line corresponds to a vehicle that generally increases its position x over time. Horizontal line segments indicate stand-still conditions with no forward motion. Bands of horizontal line segments that move diagonally-down on the plot are phantom traffic jams, which manifest as backwards-propagating density waves. (b) Flux-density relationship for human-driven vehicles on a $L = 1$ km, $\ell = 3$ lane road shows favorable agreement between empirical and simulation results. Error bars on live stream data are the inter-quartile range. DOT measurements are plotted as a continuous series of points with density ρ greater than the critical density $\rho^* \approx 30$ cars/km/lane. Solid line is the simulated mean value of $\Phi(\rho)$ and the shaded band shows statistical fluctuations.

we can express the MOBIL condition as

$$\Delta\ddot{x}_i + p(\Delta\ddot{x}_{i-1} + \Delta\ddot{x}_{j-1}) > 0, \tag{4.5}$$

where the index i corresponds to the vehicle changing lanes, $i-1$ is the current vehicle behind the lane-changing vehicle at time t, and $j-1$ is the vehicle that will be behind the lane changing vehicle at $t+1$ if i changes lanes. The constant p is referred to as the politeness factor; we choose $p = 1$, which corresponds to force minimization of a vehicle and its nearest neighbors.

In simulations with three lanes, the left-most and right-most lanes, can change into the center lane, and at every time step, vehicles in these edge lanes initiates lane changing, only if Eq. (4.5) is satisfied and a random number $r_n \in [0,1] < 0.5$. This additional random variable r_n prevents the emergence of unrealistic large-scale simultaneous lane switching. Vehicles in the center lane choose the left or right lane to change into, depending on whether $r_n < 0.5$ or > 0.5 respectively. Within fluctuations, we find that different values for p do not affect macroscopic flux-densities measurements.

In our implementation, this algorithm effectively minimizes $F^{\text{repulsion}}$ over all vehicles involved, and enables quantitative predictions of traffic flow beyond the qualitative observations of phantom traffic jams [Fig. 4.4(a)]. For example, we use the density-dependent flux $\Phi(\rho)$ as a measure to study the emergent collective properties of multi-lane traffic flow [Fig. 4.4(b)]. In empirical measurements and simulations with $\ell = 3$ lanes, we use a portion of the road $l \approx 500$ m to calculate $\Phi = \sum_i \dot{x}_i/(\ell l)$ and $\rho = \sum_i 1/(\ell l)$, where the index i runs over all vehicles in l, sampled at statistically independent temporal intervals. Comparing observational data [Fig. 4.4(b), green dots] to simulation predictions with MOBIL lane changing [Fig. 4.4(b), black line and blue-shaded band] shows a broad consistency with no fitting parameters. Both in empirical measurements and simulations, we find that when the density is low, $\Phi \propto \rho$ [Fig. 4.4(b), $\rho < 30$ cars/km/lane]. As the density increases

to a critical value $\rho^* \approx 30$ cars/km/lane, the flux peaks, and subsequently declines for increasing ρ. In simulations, we find ρ^* corresponds to an average of one vehicle per 33 m of road per lane. This distance is ≈ 1.1 s of travel time between vehicles, placing them within the repulsive-force interaction distance R. As such, when $\rho > \rho^*$, the system is effectively a 1D continuum with density waves [Fig. 4.4(a), horizontal bands] that produce the decline of Φ at larger ρ.

4.4 The inevitable jam

It is an uncontroversial empirical fact [108], and has even been demonstrated experimentally [109], [110], [111], that when a certain density of cars is reached on roadways uniform flow becomes unstable, and flow is instead dominated by traffic waves. It was previously thought that a bottleneck or accident of some sort was necessary to cause a traffic jam, but modern traffic models explain how traffic waves can emerge spontaneously via instabilities. These instabilities are approached differently in macroscopic [112], cellular [87], and microscopic [91] traffic models, but microscopic models are considered the most realistic in terms of faithfully recapitulating local traffic behavior. The stability analysis for all microscopic "car-following" models follows a similar line of reasoning, and I'll go through the exercise using the SVYY model as an example. This will allow us to highlight some salient features common to all state of the art traffic models. Later we'll introduce effects like lane changing, and vehicle/driver inhomogeneities which exacerbate traffic jams; however, phantom traffic jams can arise even in the absence of such complications.

4.4.1 Self organized jams in the SVYY model

Throughout this derivation we will use a uniform preferred speed for all cars, set to the speed limit of $v_0 = 29\frac{\mathrm{m}}{\mathrm{s}} = 65\frac{\mathrm{mi}}{\mathrm{hr}}$, and a safe separation of $R = 58\mathrm{m}$ set by the speed limit and the two-second rule as described above. Furthermore, we will let $\tau = 2\mathrm{s}$ be the human reaction time, and set ϵ so that at bumper to bumper traffic at zero velocity the self

propulsion force and the leading car repulsive force balance: $\epsilon \approx 16.5$ meters per second squared.

For a very long circular roadway with a single lane and N cars at a number density of ρ then, we have the following system of coupled nonlinear differential equations, with $n \in [1, 2, ..., \mathrm{N}]$, and $\delta x_n = x_{n+1} - x_n$.

$$\ddot{x}_n = \frac{v_0 - \dot{x}_n}{\tau} - \epsilon \left(1 - \frac{\delta x_n}{R}\right)^{\frac{3}{2}}.$$

Ideally, everyone could drive at his preferred speed (the speed limit), and simultaneously feel no repulsive force from the car in front of him. Indeed, when $\rho \leq \frac{1}{R}$ this situation can occur, and is stable. That corresponds to the linear part of the fundamental diagram at densities less than the minimum jamming density. When $\rho > \frac{1}{R}$ though, the cars begin to interact and not everyone can simultaneously be "happy". Here a happy driver is one who feels no repulsive or propulsive forces, driving at his preferred speed. What, then, is the optimal traffic configuration in terms of overall flux when $\rho > \frac{1}{R}$?

Each driver will strive to reach his own equilibrium between propulsive and repulsive forces, i.e. between wanting to drive faster than he is, and simultaneously wanting to avoid collision with the car in front of him. When these forces balance, the larger the distance to the leading car, the faster the driver can drive. Call the difference between the driver's preferred and actual speed his frustration. A driver's frustration will be reduced when the distance to the car in front of him is reduced. However, when $\rho > \frac{1}{R}$, the total frustration of all drivers must be greater than zero. Furthermore, since we have a conserved length of open freeway and a nonlinear repulsive term, any reduction in the frustration a given driver feels results in an even greater *increase* in the frustration of another driver. The optimal situation, in terms of frustration and overall flux, turns out to be when every driver is equally (minimally) frustrated.

We want to consider the stability of this scenario in which all cars are evenly spaced

and travelling the same speed (i.e. maximum flow free of traffic jams). When we are near that equilibrium we can make the following approximation

$$\frac{\langle \delta x \rangle}{\langle v \rangle} \approx \frac{\delta x_n}{\dot{x}_n},$$

which allows us to rewrite our system of equations so that the acceleration of the n^{th} car only depends on the distance to the car in front of it. Recognizing that $\langle \delta x \rangle = \frac{1}{\rho}$, the inverse vehicle number density, we have

$$\ddot{x}_n = \frac{v_0 - \rho \langle v \rangle \delta x_n}{\tau} - \epsilon \left(1 - \frac{\delta x_n}{R}\right)^{\frac{3}{2}}. \tag{4.6}$$

We can then find an $\ell = \delta x_n$ for all n such that the propulsive and repulsive forces balance and every driver experiences the same minimal frustration.

$$0 = \frac{v_0 - \rho \langle v \rangle \ell}{\tau} - \epsilon \left(1 - \frac{\ell}{R}\right)^{\frac{3}{2}} \tag{4.7}$$

ℓ is therefore a function only of the overall flux $\Phi = \rho \langle v \rangle$, and equation 4.7 has multiple real roots when Φ is in realistic ranges for traffic flow above the jamming density. We will consider the linear stability of any choice of ℓ. We can linearize equation 4.6 about $\delta x_n = \ell$ to make an approximation of the dynamics near the equilibrium, jam free, point.

$$\begin{aligned}
\ddot{x}_n(\delta x_n - \ell) &\approx \ddot{x}_n(\ell) + \frac{\partial}{\partial \delta x_n} \ddot{x}_n(\ell) \cdot (\delta x_n - \ell) \\
\ddot{x}_n(\delta x_n - \ell) &\approx -k \, (\delta x_n - \ell) \\
k &= \frac{\rho \langle v \rangle}{\tau} - \frac{3\epsilon}{2R} \left(1 - \frac{\ell(\Phi)}{R}\right)^{\frac{1}{2}}
\end{aligned}$$

Let's now make a change of variables. Define $q_n = x_n - x_n^*$, where x_n^* is the equilibrium

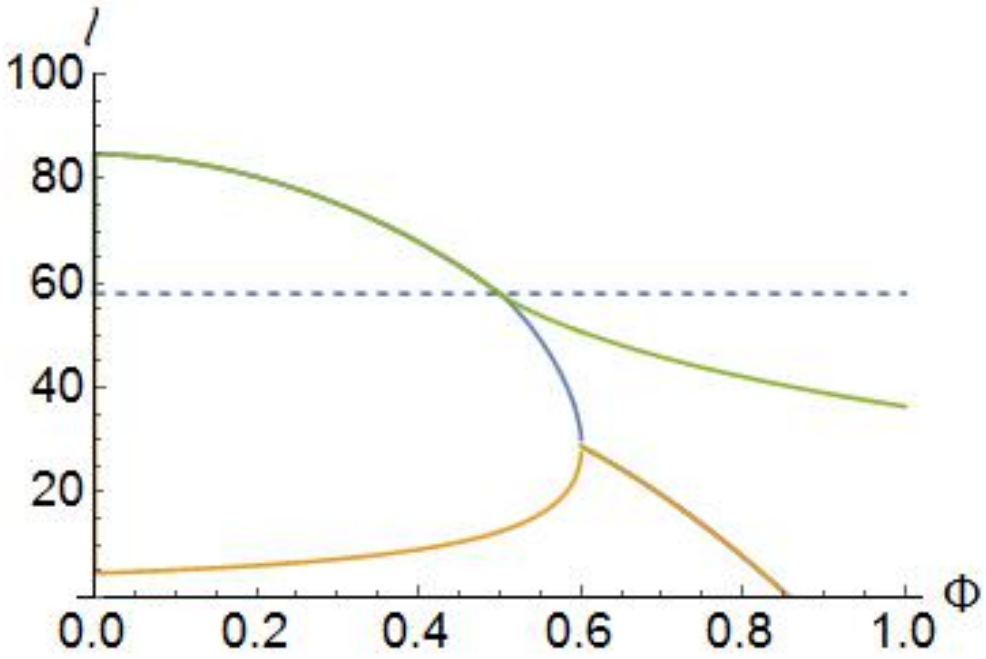

Figure 4.5: ℓ as a function of $\Phi = \rho\langle v\rangle$. Blue horizontal dashed line is at $\ell = R = 58\mathrm{m}$, the maximum interaction distance between two cars (when $\delta x > R$ the repulsive force is zero). When $\Phi = \rho\langle v\rangle$ is small at low density but high mean speeds the system is stable and everyone drives the speed limit. At a critical density of $\rho = \frac{1}{R}$, everyone can drive the speed limit if they are all equally spaced at $\delta x = R$. This corresponds to the point where the blue dashed line intersects the upper green curve. At this point $\langle v\rangle = 29$ meters per second (the speed limit), $\rho = \frac{1}{R} = \frac{1}{2\cdot 29}$ cars per meter, and so $\Phi = \frac{1}{2}$ cars per second. In other words, every car is two-seconds behind its leader, obeying the two second rule. This point also corresponds to the end of the linear regime in the fundamental flux-density diagram. When $\rho > \frac{1}{R}$ the total frustration must be non-zero. The optimal situation would be for everyone to remain equally spaced and follow along the upper green curve. However, that solution is unstable and instead traffic jams ensue. Simulations on a ring-road suggest the system breaks into two sort of "phases", a slow moving high density "jam", at small ℓ, and a fast moving free flowing state with ℓ locally greater than R.

position of the n^{th} vehicle. Then we have

$$q_n = x_n - x_n^*$$

$$\ddot{q}_n = \ddot{x}_n = -k(x_{n+1} - x_n - \ell)$$

$$\ddot{q}_n = -k\left((q_{n+1} + x_{n+1}^*) - (q_n + x_n^*) - \ell\right)$$

$$\ddot{q}_n = -k\left(q_{n+1} - q_n\right)$$

where we used $x^*_{n+1} = x^*_n + \ell$. This almost looks like a familiar one dimensional system of balls and springs with periodic boundary conditions, but these are springs of a peculiar sort! Compare with the conventional system, $\ddot{\tilde{q}}_n = k\tilde{q}_{n-1} - 2k\tilde{q}_n + k\tilde{q}_{n+1}$. The SVYY system (if $k < 0$) corresponds exactly to the system of balls and springs except that each ball is coupled somehow only to the ball in front of it and manages to ignore the influence of the ball to its rear. This violates Newton's third law, and as we'll see, it is not a stable situation for any k. Before moving on though, it's worth pointing out that in every car following traffic model linearized about a similar equilibrium we come to the same result. One feature leading to instability is drivers' ignoring cars behind them (at least to a large extent). Wang et al (including Gilbert Strang of linear algebra fame) noticed this and suggested a "bilateral control" solution for autonomous cruise control systems that couples each car to its leader and follower, leading to a conventional ball-and-spring system that can be stabilized under appropriate choice of parameters (so that k is of the correct sign) [113].

Our system of equations has the form:

$$\frac{d^2}{dt^2}\vec{q} = \mathbf{K}\vec{q},$$

with solutions which are a linear superposition of the following eigenmodes:

$$\vec{q}(t) = \vec{q}(0)e^{i\omega_i t}.$$

Here, ω_i, the i^{th} eigenvalue of the $N \times N$ matrix

$$\mathbf{K}_{ij} = \begin{cases} k & i = j = 1, \\ k & i = j, \\ -k & i = j - 1, \\ -k & i = N, j = 1 \\ 0 & \text{otherwise} \end{cases}$$

The eigenvalues (ω^2) of such a matrix lie on a circle in the complex plane

$$\omega_j^2 = k\left(1 + e^{\frac{2\pi j \mathbf{i}}{N}}\right).$$

(note that j is an index and i is the imaginary number $\sqrt{-1}$.)

If the imaginary part of any of the ω's is negative, then an infinitesimal activation of the corresponding eigenmode will tend to grow exponentially in time. However, for any system with at least a few cars there is always at least one mode with an eigenvalue that has this unstable property. Hence, a perturbation to the traffic-jam-free state will grow exponentially meaning that this state is always unstable (for any such equilibrium state above the threshold density $\rho > \frac{1}{R}$.

So what happens instead? Traffic jams ensue. Simulations on a ring-road suggest the system breaks into two "phases", a slow moving high density "jam", at small ℓ, and a fast moving free flowing state with ℓ locally greater than R. This phenomenology should be familiar to my committee members who live in Atlanta, as stop-and-go traffic.

4.5 Autonomous vehicles and hacking

Human driving behavior has not substantially changed over the last century, and our understanding of how traffic flows on a single road without intersections or bottlenecks is

largely considered "settled" [84]. Most recent advances in the understanding of traffic patterns, and corresponding engineering developments, therefore, have revolved around road design, intersections, traffic metering, and other complications beyond simple traffic flow on a single road. However, the advent of internet connected vehicles and level 1 and above autonomous vehicles (AVs) heralds a fundamental change in traffic flow emerging from alterations to the "microscopic" behavior of individual agents themselves (human drivers and AVs). AVs divergence from human driving behavior could range from subtle increases in safety and efficiency to completely alien and counter-intuitive maneuvers. In any event, the introduction of AVs opens the door to new physics and may also provide an opportunity to avoid phantom traffic jams, which has so far been impossible.

The increase in the level of automation in vehicles, as well as the number of automated vehicles is imminent as massive. In the United States, nearly 50 million Internet-connected vehicles are on the road today, with projections estimating 100 million by 2023 (Fig. 4.6a, gray circles) [114]. Connected vehicle technologies have the potential to transform transportation by preventing accidents, reducing congestion, and even improving in-vehicle worker productivity [115].

However, another trend is on the rise: the widespread hacking of Internet-connected devices, which as of 2015, includes vehicles. While the first proof-of-concept automobile hack was done at the single-vehicle scale, undesirable collective effects can easily arise if this activity becomes more common. In light of the growing number of hacking incidents exposing personal data (Fig. 4.6a, blue circles) [116], cybersecurity experts are working to preemptively resolve similar software vulnerabilities and keep Internet-connected vehicles secure from similarly malicious activity [117, 118, 119]. Nevertheless, in the event of a successful hack, compromised vehicles carry unknown cyber-physical risks, making it difficult to assess the mode and scale of disruption presented by this increasingly plausible scenario [120].

Motivated by these two trends, we explore the phenomena that arise in a mixed hu-

man/autonomous fleet of vehicles on a highway. We use the SVYY model as well as the IDM and the Nagel-Schrekenberg cellular automaton model. To each of these models we incorporate a simplified minimal description of essential differences between human- and autonomous-drivers. We study the emergent collective behavior as the population of vehicles shifts from all-human to all-autonomous. Within this context, we explore a worst-case scenario where Internet-connected autonomous vehicles are disabled simultaneously and *en masse*.

4.5.1 Autonomous vehicles and traffic jams

Of course, if all vehicles on the roadways are autonomous, the task of traffic flow control becomes trivial. If all agents are in communication with one another then an almost train-like array of vehicles can flow seamlessly together at any speed. However, before that, a long period of mixed human AV flow will occur on our roadways. Simulation based studies with AVs that drive basically like humans but with faster reflexes have demonstrated that AV penetration rates above 20% ameliorate traffic jams to some extent. Simulation approaches using the IDM have shown how throughput (flux) increases with AV penetration [121, 122]. In addition, several studies have investigated how string stability (another concept frequently discussed- similar to the stability analysis for a ring road outlined above) changes with AV penetration, or with the introduction of adaptive cruise control [123, 124, 125, 121]. Consistent with the organization of this chapter, we will use the SVYY model to demonstrate the positive effect of AV penetration on flux and increased stability in this chapter. However, the analysis in other works yields qualitatively similar results.

So far, our simulations and analysis of the SVYY model have focused on human-driven vehicles. Incorporating autonomous vehicles amounts to two additional specifications. First, we remove all heterogeneity from AVs' preferred speed— they all prefer to drive the speed limit. Second, we fix the final parameter τ_A, which is the autonomous driver response time. Given these highly computerized vehicles are expected to utilize a combination of lo-

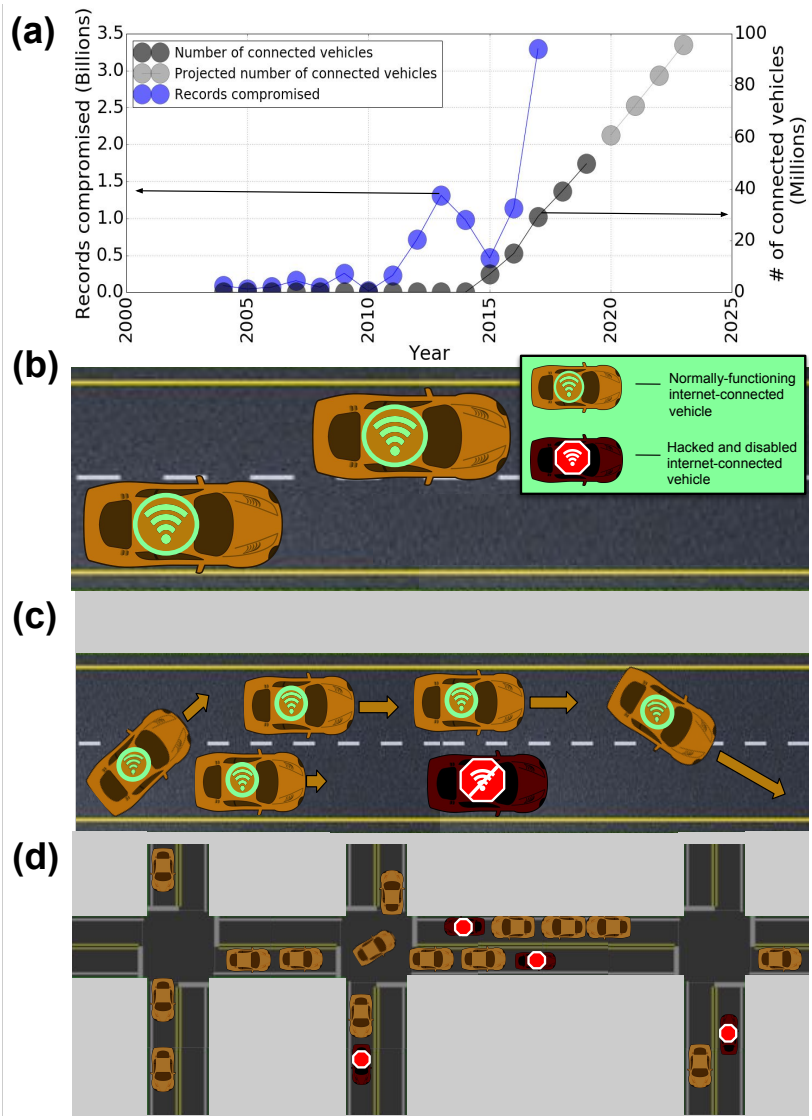

Figure 4.6: Potential cyber-physical disruption from hacking of Internet-connected vehicles. (**a**) Historical annual data for total number of Internet-connected vehicles (dark gray) along with anticipated projections (light gray), and total number of digital records compromised by hacking (blue). (**b**) Schematic of two Internet-connected vehicles traveling unobstructed on a straight 2-lane road. (**c**) Schematic of traffic flow when an Internet-connected vehicle is disabled (red) and other vehicles must navigate around the obstacle. (**d**) Schematic illustrating how multiple simultaneously disabled vehicles disrupts traffic flow on a network of roads.

cal sensor information, wirelessly shared non-local traffic conditions, and cloud-connected AI, we can reasonably assume they will respond to driving conditions more rapidly than human drivers. As an order of magnitude estimate, we set the autonomous vehicle response time $\tau_A = 0.1$ s, which is a fraction of the human response time τ_H, but still larger than the simulation time step. Simulations with all autonomous vehicles immediately show important differences in the flux $\Phi(\rho)$, highlighting a key advantage of autonomous vehicles over human drivers that underlies their anticipated impact on automotive transport. Specifically, $\Phi(\rho)$ still peaks near the same critical density ρ^*, however, with all autonomous vehicles $\Phi(\rho^*)$ is nearly 20% larger [Fig. 4.7(a), upper light-bronze data]. Even with a 50/50 mix of autonomous and human vehicles there are substantial advantages at the highest densities where the flow is steadier relative to results with all human drivers [Fig. 4.7(a), upper light-red data, $\rho > \rho^*$ cars/km/lane]. The combination of higher throughput and steadier flow translate to reduced congestion, reduced fuel consumption, and less time spent traveling between destinations.

Interestingly, $\Phi(\rho)$ in all-autonomous vehicle simulations can be predicted from Eqs. (4.3). Given the uniform preferred speed and rapid response time, $\Phi \approx N_A \dot{x}/(\ell L) = \rho \dot{x}$. Under steady conditions, propulsion and repulsion forces balance so that $\ddot{x} = 0$ and $\delta x = 1/\rho$, which leads to $\dot{x} = v_A - \tau \epsilon_A [1 - 1/(2\rho v_A)]^{3/2}$. The flux is therefore the real part of $\Phi(\rho) = \rho v_A - \rho \tau \epsilon_A [1 - 1/(2\rho v_A)]^{3/2} = \rho v_A \left[1 - \left(\frac{1-1/(2\rho v_A)}{1-r/R}\right)^{3/2}\right]$, where we have used the expression for ϵ_A derived from force balance to find the final equation. Comparing this prediction to simulations shows strong agreement [Fig. 4.7(a), solid black line]. This analysis is similar to the one performed in section 5.1, and is also how the schematic fundamental diagram in figure 4.1 was created.

From the perspective of the flux-density relationship, there are measurable benefits to having an increased number of autonomous vehicles on the road due to the generally increased throughput of traffic. However, as indicated by recent proof-of-concept hacks, Internet-connected vehicles are endowed with enhanced abilities at the cost of new risks.

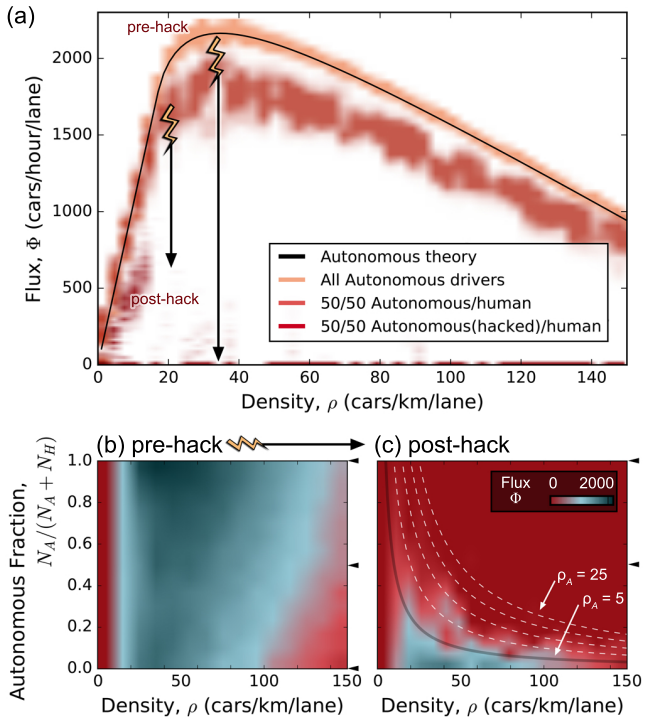

Figure 4.7: While increasing the number of autonomously-driven vehicles generally increases the total flux Φ, a malicious hack disabling autonomous vehicles sends Φ to near-zero values, especially in high-density traffic. (a) Flux-density relationship shows how increasing the number of autonomous drivers from 50% (upper light-red data) to 100% (upper light-bronze data) offers greater vehicle throughput. A hack that disables autonomous vehicles reduces the flux to zero or near-zero values (lower dark-red data). Solid black line is a theoretical prediction for autonomous drivers based on force-balance in Eq. 4.3. (b) Heat map for the flux Φ generally shows increased throughput of vehicles as autonomous drivers replace human drivers. (c) Disabled autonomous vehicles create bottlenecks on the road leading to unsteady and near-zero flow. Gray lines represent contours of constant density of disabled autonomous vehicles $\rho_A = 5, 10, 15, 20,$ and 25.

The worst-case scenario we consider is one in which hacked vehicles are disabled during transit, which in the context of our model, amounts to setting $v_A = 0$ after the simulation has reached steady-state. This type of event has actually been proposed as an active self-defense mechanism for vehicles that detect their systems have been compromised, though it was offered in the context where only a single vehicle was being considered[126]. If we assume this strategy was broadly deployed, a wide-spread hack that compromises many vehicles simultaneously would most certainly give rise to new collective behavior that affects any functional vehicles still on the road. For example, a 50/50 mixture of human and autonomous drivers in this circumstance has a substantial loss of flow with a nearly 60% reduction in the peak flux and a total loss of flow at higher densities [Fig. 4.7(a), lower dark-red data $\rho > 20$ cars/km/lane].

Generating heat maps for $\Phi(\rho)$ with varying fractions of autonomously driven vehicles $N_A/(N_A + N_H)$ offers a more complete view of the benefits of autonomous vehicles [Fig. 4.7(b)] as well as the effects on flow when these vehicles are disabled [Fig. 4.7(c)]. Comparing the pre-hack to the post-hack results show the flow largely collapses when vehicles are disabled, leaving behind unsteady and near-zero flux, even at relatively low fractions of autonomous vehicles [Fig. 4.7(b) and (c), increased size of red region]. In the post-hack scenario we observe the flux substantially drops when the fraction of disabled autonomous vehicles exceeds 10 to 20% [Fig. 4.7(c), boundary of lower green band]. At the same time, this number of self-driving vehicles corresponds to a rather small benefit in the pre-hack scenario relative to bounds at the $N_A/(N_A + N_H) = 0$ and 1 limits [Fig. 4.7(b)]. Evidently, the risks introduced by connected-car technologies have an earlier onset than the benefits, as measured by vehicle throughput.

One method to try to achieve the benefits of AVs without the risks of large scale hacks would be to limit the number of autonomous vehicles on the road and simultaneously increase the level of their "intelligence". Daniel Work's group proposes a solution whereby traffic jams can be eliminated with less than 5% AV penetration [127]. They consider the

stability on a ring road of a fleet of mostly human drivers with a few AVs, and use optimal control theory to show that they can prevent unstable eigenmodes from arising. Similar results have been published using reinforcement learning to teach an AV how to stabilize traffic [128]. It is also highly likely that unpublished work at e.g. Google has already made much progress in this direction. However, it is ultimately unlikely that huge numbers of AVs will be prevented from hitting the roads. There is too much momentum and profit motive, and with 50 million internet-connected vehicles currently on the roads, the cat is already halfway out of the bag.

4.5.2 Compromised vehicles impair traffic

Instead, in this work, we seek at least to begin to quantify the risks associated with hacking of AVs. As mentioned above, we focus on the event in which many AVs are simultaneously brought to a halt. While a full accounting of the risks presented by Internet-connected vehicles remains elusive, this open-ended question hasn't stopped active exploration of the possibilities. Already, a number of scenarios have been outlined to identify how hacking increases the risk of collisions [117, 129, 130] and traffic disruptions [130]. For example: (i) degraded sensor input or distorted control protocols could cause connected-vehicle collisions [129], (ii) self-monitoring anti-virus-like software could cause compromised vehicles to enter a "safe mode" when problems are detected and bring the vehicle to a stop, reducing the likelihood of accidents but increasing localized traffic congestion [118, 131, 132], (iii) similar self-monitoring software could directly lead to human-failure if control of a compromised vehicle was returned to an unprepared or distracted driver [133], and (iv) hacked sensors could be used to falsely report traffic or other objects on the road, thus inappropriately halting motion of compromised vehicles [118, 134]. Furthermore, as driver-assisting and "auto-pilot" technologies continue to be incorporated in modern vehicles, we can anticipate an even deeper integration between mechanical components and software-controlled systems. In fact, some manufacturers already use wireless over-the-air updates to regularly

upgrade and maintain their vehicle's software. Thus, given the increased exposure to potential cybersecurity vulnerabilities, the growing physical control by these cybersystems over vehicular motion, and the historical precedent that "if it can be hacked, it will be hacked," we can foresee the general contours of an emerging threat. In particular, many of the cybersecurity scenarios being considered lead to a common outcome where compromised vehicles cease motion and effectively become traffic-disrupting obstacles (Fig. 4.6b and c). From the physical perspective, we can ask what this outcome means for transportation as we quantify the emergent consequences of this cyber-physical risk.

The scenario we investigate here is one in which a substantial number of vehicles are simultaneously disabled in a single event causing them to become immobile obstacles on the road. To this end, we model hacked vehicles as stopped vehicles blocking road traffic (Fig. 4.6d). This approach allows us to set aside specifics of how cybersecurity vulnerabilities are exploited, and more broadly focus on a variety of scenarios with the same general outcome: hacked vehicles blocking roads. We simulate traffic flow before and after a hack has occurred so that non-compromised vehicles continue to navigate around compromised vehicles wherever possible. Surprisingly, we find a relatively modest density of compromised vehicles can immediately halt all traffic flow. By deriving an analytical model based on percolation theory, we show the underlying cause of this result is the local geometric arrangement of vehicles. Application of our model to Manhattan (New York City, New York, USA) reveals the threshold number of compromised vehicles that causes city-wide gridlock and quantifies how access to emergency services is reduced. We recognize that modeling city-scale traffic patterns post-hack is a challenging problem. Nevertheless, our percolation approach enables quantification of the worst-case city-wide gridlock. Furthermore, the insights provided by our model suggest how the risks of large-scale hacks can be addressed via network compartmentalization and redundancy.

To begin our examination of how hacking targeted at Internet-connected vehicles disrupts traffic, simulate individual vehicles with the Intelligent Driver Model (IDM) [84,

93, 135], a time-continuous car-following set of equations that quantitatively reproduces known traffic dynamics, discussed in section 4. To model lane changing, we use the Minimizing Overall Breaking Induced by Lane changes (MOBIL) framework [107, 92], discussed in section 4. Briefly, a vehicle changes lanes if doing so would allow it and its neighbors to better match their preferred speeds. As a validation for these simulations, we varied the density of vehicles, ρ (number of vehicles/km/lane), and measured the flux, $\Phi(\rho)$ (number of vehicles/hr/lane), on a 3 lane road. These simulations reproduce the classic peaked relationship between traffic flux and density (Fig. 4.8a, green symbols), which has been observationally measured and theoretically reproduced in agent-based and continuum models [84, 136, 105].

A variety of hacking scenarios targeting Internet-connected vehicles lead to the same generic outcome where compromised vehicles stop and become obstacles on the road. We simulate these scenarios by randomly selecting vehicles and marking them as compromised, thus halting their motion. We then simulated post-hack traffic on a straight 3 lane road with periodic boundary conditions to maintain constant total vehicle density. We investigated realistic densities ranging from $\rho = 1$ to 150 vehicles/km/lane, and fraction of compromised vehicles ρ_H/ρ ranging from 0% to 100% of all vehicles. Values for ρ were chosen by sampling between 1 to 150 vehicles/km/lane in increments of 3 vehicles/km/lane, while ρ_H was similarly chosen between 1 and ρ vehicles/km/lane corresponding to different values of ρ. Post-hack, we observe decreased flux at every density (Fig. 4.8a, dark red symbols). Interestingly, these data separate into two distinct regimes. Traffic continues to flow in $\approx$ 15% of the simulations across the entire range of sampled rho, rho_H, albeit at a significantly reduced rate (Fig. 2a, red band centered on $\Phi \approx 400$ vehicles/hr/lane). More strikingly, the remaining $\approx$ 85% of the simulations lead to a complete loss of traffic flow (Fig. 4.8a, red data at $\Phi = 0$ vehicles/hr/lane). Evidently, there are two distinct phenomenologies arising post-hack: one where traffic is slowed, and another where traffic is stopped. The gap between these two $\Phi(\rho)$ curves (Fig. 4.8a, white region where $\Phi \approx 100$

vehicles/hr/lane) is broadly independent of ρ, suggesting a categorical distinction between the two flow phenomena and ruling out a continuous transition between the flow and no-flow states.

To better understand the effects of disabled vehicles on traffic flow, we plot the same simulation data as a flux heatmap with varying density and fraction of compromised vehicles (Fig. 4.8b). Most of the heatmap's area corresponds to zero-flux outcomes (Fig. 4.8b, dark red), echoing the observation that $\approx 85\%$ of the simulations lead to a complete loss of traffic flow. Intriguingly, contours of constant Φ coincide with contours of constant compromised vehicle density, ρ_H (Fig. 4.8b, white solid and dashed lines).

There are two classic flow phenomena that can produce zero-flux in the presence of constrictions: clogging [137, 138, 139] and percolation [140]. In the first case, interactions between objects produce configurations that prevent other objects from flowing past each other, eventually arresting flow. Thus, clogging is a kinetic phenomenon, and the typical time it takes for a clog to form depends on the density of both mobile constituents and obstacles [139]. In fact, clogging is the phenomenological flow we commonly see when a vehicle breaks-down or traffic congestion increases during rush hour; in both cases, traffic flux gradually decreases over an expanding stretch of road. In contrast, percolation occurs when a continuously connected obstruction spans the system, and is therefore a purely geometric phenomenon [140]. Thus, while clogging is a slow build-up to reduced traffic, percolation is a sudden and abrupt transition from flow to no-flow states independent of the density of free-flowing vehicles. Our observations that flux contours are consistent with ρ_H rather than ρ (Fig. 4.8b, white solid and dashed lines) suggests that geometric percolation of compromised vehicles is the underlying zero-flux mechanism in post-hack traffic considered here. To rephrase this conclusion in more physically intuitive terms, the transition to zero-flux occurs when disabled vehicles line-up sideways across all lanes of the road, forming an impassable obstacle that "percolates" across all lanes. The question then becomes how to calculate the likelihood of this configuration occurring for a given set

of road and driver conditions.

4.5.3 Analytical expression for post-hack traffic flow

If post-hack traffic flow is a percolation flow phenomenon, an analytical expression for disabled vehicles to randomly align into geometric blockages should predict the probability of zero-flux traffic. Given the prevalence of zero-flux events post-hack in our highway-like simulations, even when only a portion of vehicles are compromised, we sought to understand whether percolation of compromised vehicles is the dominant phenomenon after a cyber-attack. Percolation of disabled vehicles occurs when, on an ℓ lane road, there is an ℓ-tuple of disabled vehicles positioned across all lanes such that no other vehicle can pass them (Fig 4.8a, lower inset).

To this end, we derived an expression for the probability of a percolated configuration on an ℓ lane road of length L and a per-lane vehicle density ρ, with effective vehicle size d. The effective vehicle size is the length from the rear bumper of one vehicle to the rear bumper of the *next* vehicle in "bumper to bumper" traffic. Of course in bumper to bumper traffic cars' bumpers are not actually in contact, so d is slightly larger than the physical length of a vehicle. In our case $d = 7$ m, which is typically the separation between cars in dense traffic [93].

To determine the probability that compromised vehicles end up in a percolated position, *i.e.* one that would block all lanes of a highway if the vehicles were frozen in place, we first assume that the position of the i^{th} connected vehicle in lane α will be distributed uniformly:

$$X_i^\alpha \sim U(0, L) \;\; \forall i, \alpha.$$

We next define the random variable

$$Z_{ii'} = |X_i^\alpha - X_{i'}^{\alpha+1}|,$$

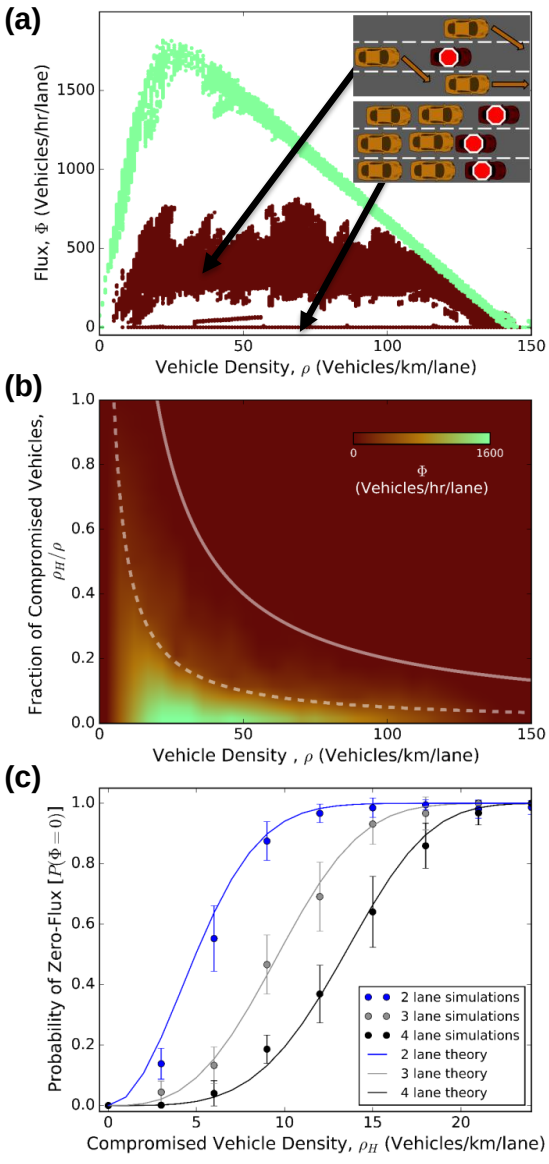

Figure 4.8: Disruption of vehicle traffic caused by hacking on individual roads. Caption continued on subsequent page.

Figure 4.8: Disruption of vehicle traffic caused by hacking on individual roads. (**a**) Vehicle flux Φ for normal driving conditions (light green) compared to the flux after a number of vehicles are disabled by hacking (dark red). Simulations explore $0 \leq \rho \leq 150$ vehicles/km/lane, and a varying fraction of disabled vehicles $0 \leq (\rho_H/\rho) \leq 1$ (dark red). Vehicle flux post-hack causes a bifurcation of the data with $\approx 15\%$ of the simulations having residual flow ($\Phi > 0$ vehicles/km/lane), while the remaining 85% have no flow ($\Phi = 0$ vehicles/km/lane). Insets schematically illustrate the traffic flow patterns. (**b**) Data in (a) plotted as a heatmap. Lines correspond to contours of constant compromised vehicle density with $\rho_H = 5$ (dashed) and 20 (solid) vehicles/km/lane. (**c**) Probability that agent-based IDM/-MOBIL simulations produce a zero-flux outcome (dots) compared to the predictions of percolation theory (solid lines).

which describes the center-to-center distance between two vehicles in adjacent lanes, projected onto the direction of traffic flow. This is the quantity we are interested in, since we want to understand the probability that cars in adjacent lanes are positioned such that a third car can not lane-change between or around them. In other words, we want to know if compromised vehicles in adjacent lanes are a distance no greater than s from each other, where s is twice the effective car length (Fig. 4.9). If $Z_{ii'} \geq s$ for all pairs of cars i and i' in adjacent lanes, then percolation of compromised vehicles did not occur; a configuration that would cause compromised vehicle percolation across two adjacent lanes occurs with probability $P(Z_{ii'} < s)$.

Since $Z_{ii'}$ is a random variable related to the difference between two uniformly distributed random variables with known probability distribution functions, we can directly calculate $P(Z_{ii'} < s)$ using convolution. In fact, we derive this probability for an arbitrary real number z. For example let's consider cars labeled by $i = 1$ and $i' = 2$. The probability distribution functions for their positions, X_1 and X_2, are

$$f_{X_1}(x) = f_{X_2}(x) = \begin{cases} 1/L, & \text{if } 0 \leq \mathrm{x} \leq \mathrm{L}, \\ 0, & \text{otherwise.} \end{cases}$$

We seek the cumulative distribution function for z, because this will give us the probability

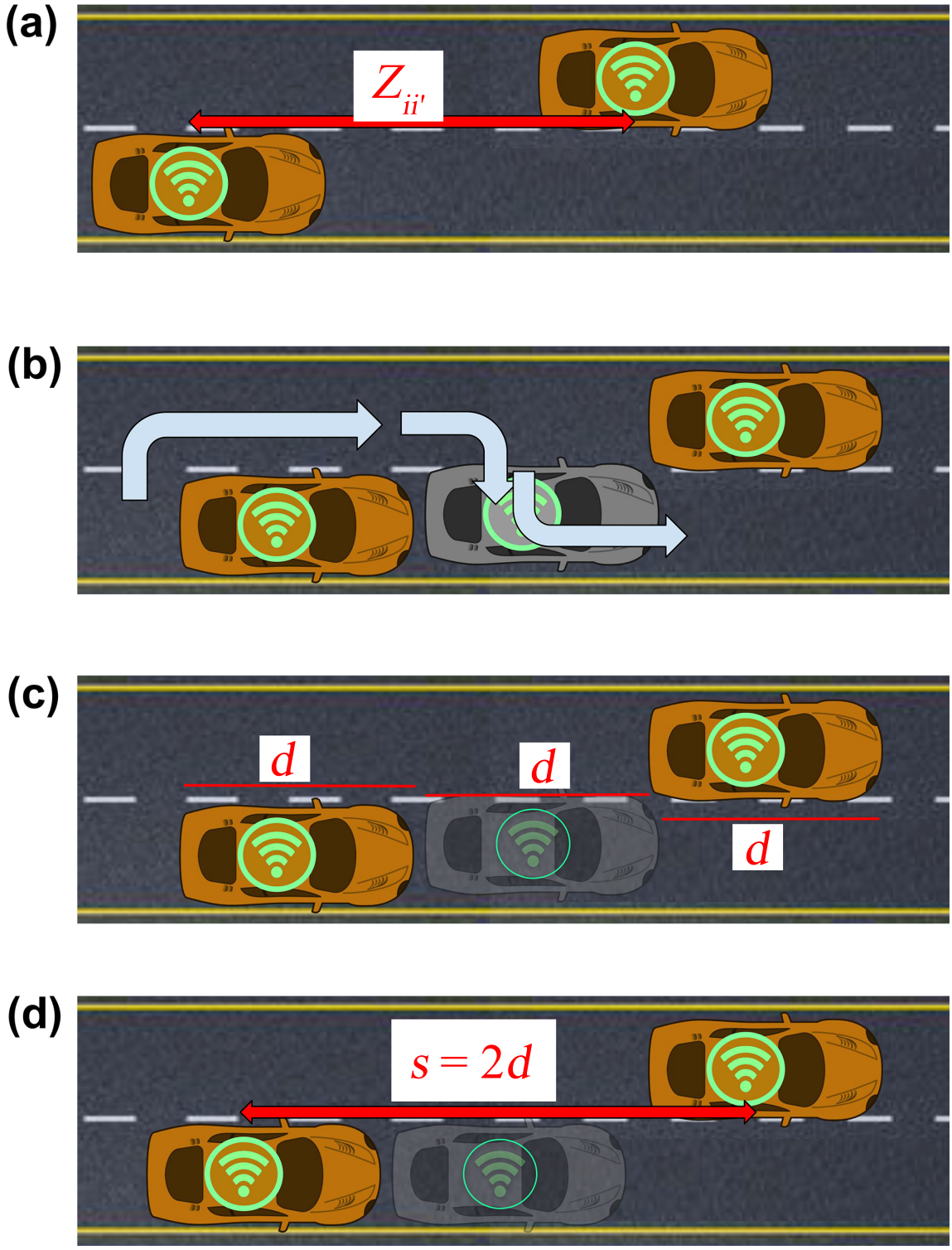

Figure 4.9: Cartoon showing how we define s during the obstacle percolation derivation. Caption continued on subsequent page.

Figure 4.9: Cartoon showing how we define s. **(a)** The center-to-center distance between two vehicles i and i' on lanes α and $\alpha+1$ is considered a random variable $Z_{i\,i'}$. **(b)** In order for the silver vehicle to lane change around the orange vehicle in the right lane, it has to be able to fit between the two orange vehicles, following the path shown. **(c)** If the silver car can just barely fit between the orange vehicles, and each vehicle has an effective size d, then **(d)** the minimum center-to-center distance between the orange vehicles that *wouldn't* cause compromised vehicle percolation if the orange vehicles were suddenly hacked is $s = 2d$. Of course, while the cartoon shows three cars of actual length d tightly packed bumper to bumper, in reality vehicles need a little bit of extra room to maneuver, beyond their physical size. This is why we use the effective vehicle length d of 7 m rather than the actual average length of a vehicle in calculating the minimum center-to-center distance between vehicles to avoid compromised vehicle percolation, s. So s is the minimum required center-to-center distance between vehicles such that they are not in a position that they would cause compromised vehicle percolation upon being disabled by a hack.

that $Z_{i\,i'} < z$ for any arbitrary real number z. The cumulative distribution function is:

$$\begin{aligned} F_{Z_{12}}(z) &= P(Z_{12} \leq z) = P(|X_1 - X_2| \leq z), \\ &= P(-z \leq X_1 - X_2 \leq z), \\ &= P(X_1 - X_2 \leq z) - P(X_1 - X_2 \leq -z), \\ &= F_{X_1 - X_2}(z) - F_{X_1 - X_2}(-z). \end{aligned}$$

By taking derivatives and using the chain rule, we can get the probability distribution functions:

$$f_{Z_{12}}(z) = f_{X_1 - X_2}(z) + f_{X_1 - X_2}(-z)$$

Note that $f_{X_1 - X_2}(z)$ is the convolution of $f_{X_1}(z)$ with $f_{-X_2}(z)$, and that we know X_1 and X_2 are distributed uniformly on the interval $[0, L]$. Then we can write, compactly:

$$f_{X_1 - X_2}(z) = \frac{1}{L^2} \int_0^L \int_0^L \delta((x_1 - x_2) - z)\, dx_1 dx_2,$$

$$= \frac{L - z + 2Lz\Theta(-z)}{L^2}.$$

Where $\delta(\ldots)$ is the delta function and $\Theta(\ldots)$ is the Heaviside step function. This is the standard triangular distribution, sometimes called the uniform difference distribution. The integration must be performed carefully here, because the cases when $z \geq 0$ and $z < 0$, and when $x_1 \geq x_2$ and $x_1 < x_2$ must each be considered separately [141]. We notice right away that this expression is an even function of z and so $f_{X_1-X_2}(z) = f_{X_1-X_2}(-z)$ and so $f_{Z_{12}}(z) = 2f_{X_1-X_2}(z)$. We are only interested in distances, so without loss of generality we focus on $z > 0$. Thus, we can simplify:

$$f_{Z_{12}}(z) = \frac{2}{L^2}(L - z).$$

To find $P(Z_{12} < z)$ we integrate:

$$P(Z_{12} < z) = \frac{2}{L^2}\left(Lz - \frac{1}{2}z^2\right)$$

Nothing on the right hand side of the above equation depends on the vehicle labels 1 and 2. This observation is generally true for any pair of vehicles on adjacent lanes. In addition, this independence is true for any arbitrary real number z. We are interested, however, specifically in the probability that two vehicles on adjacent lanes are separated by a distance less than s, so we define:

$$P_{\text{pair blocks}} = P(Z_{ii'} < s) = \frac{2}{L^2}\left(Ls - \frac{1}{2}s^2\right).$$

This is the probability that a pair of vehicles in adjacent lanes is positioned such that it would *completely block* both of those lanes if the vehicles were frozen in place. For a two-lane road, this would completely block the motion of vehicles. When distributing an ℓ-tuple of vehicles on an ℓ lane road, the probability that the tuple does *not* block the entire road is given by

$$P_{\text{tuple clear}} = 1 - P^{\ell-1}_{\text{pair blocks}}$$

as there are $\ell - 1$ pairs of lanes to consider.

Finally, we can calculate the overall probability that *any* tuple *does* block the highway. To do so, we consider every ℓ-tuple of vehicles that could potentially percolate, and find:

$$P_p = 1 - P_{\text{tuple clear}}^{n^\ell}$$

where n is the number of vehicles in each lane, and there are $\approx n^l$ tuples that could each potentially block the highway. In this last step, we assumed $n_j \approx n_{j'}\ \forall j, j'$, i.e., there are equal numbers of vehicles in each lane. This was not strictly enforced in simulations, yet simulations still agreed with the analytical formula. Collecting all of these terms, and replacing n with $L \cdot \rho_H$ we find the result for Eq. (4.8).

$$P_p = 1 - \left[1 - \left(\frac{s}{L}\right)^{\ell-1} \cdot \left(2 - \frac{s}{L}\right)^{\ell-1}\right]^{(L\cdot\rho_H)^\ell}. \tag{4.8}$$

This mathematical prediction based on the hypothesis of percolation is consistent with simulations we performed varying each parameter, and is also independent of the traffic model used. We simulated post-hack traffic flow using the Nagel-Schreckenberg model as well as the SVYY model with similar agreement (figure 4.10). The advantage offered by this calculation over direct numerical simulations is that it is geometrical and hence model independent, and also that it allows for immediate percolation probability calculations without the need for computationally intensive numerical simulations of agent-based models.

We derived this expression to account for an arbitrary number of lanes, ℓ, the density of compromised vehicles per lane, ρ_H, the length of the road, L, and the minimum center-to-center distance between two vehicles on adjacent lanes that still allows a third vehicle to lane-change between them, s. That is, s is twice the vehicle length, which is held constant for simplicity.

This expression gives the probability that compromised vehicles are positioned in such

a way as to block all lanes of a multi-lane road. While we are interested in varying ℓ, ρ_H, and L to account for different traffic conditions and magnitudes of hacks, the effective vehicle length is fixed at 7 m ($s = 14$ m), which corresponds to the typical separation between cars in dense traffic [93].

We simulated hacking events of different magnitudes, as measured by the number or fraction of vehicles compromised during the hack, and measured the flux to determine whether zero-flux events occur as frequently as predicted by percolation in Eq. (4.8). Indeed, our analytical expression accurately captures the relationship between the probability of zero-flux, the density of compromised vehicles, and the number of lanes (Fig. 4.8c solid lines), with a remarkably high coefficient of determination in each case ($R^2 > 0.99$). This is consistent with our hypothesis that geometric percolation causes standstill traffic in the post-hack conditions we explore; if clogging played a significant role, zero-flux traffic would have occurred more often than predicted by this analytical expression (Supplementary Materials) [138, 137].

Beyond computational simulations, human drivers self-organize on roads forming spatial distributions that may differ from those formed by the combined IDM/MOBIL model. To address this potential concern and validate our percolation formula, we made use of the NGSIM dataset [142], which is a US Department of Transportation-funded measurement of driver spatiotemporal trajectories. Similar to the procedure used to analyze simulations, we randomly selected a subset of vehicles to be hacked, compromised, and disabled (Supplementary Materials). We found our analytical model again captures the percolation probability with high accuracy ($R^2 > 0.99$), even when applied to the empirical NGSIM data.

Percolation of compromised and disabled vehicles across a road or highway represents a particularly concerning scenario, as emergency vehicles can no longer use roads that become totally blocked. Furthermore, this analysis shows that zero-flux can occur with surprisingly low densities of disabled vehicles. For example, with just 6 compromised

vehicles/km/lane ($< 5\%$ of cars in bumper-to-bumper traffic) the probability of percolation across a two lane road is $\approx 60\%$. Fortunately, as percolation is a geometric effect, the probability that a hacking event will block a road can be directly calculated with Eq. (4.8) for any set of parameters, circumventing the need for time-consuming, model-specific, agent-based simulations. Thus, this mathematical insight enables us to rapidly assess the risk of zero-flux traffic for any road, with any number of compromised connected vehicles.

Compromised vehicles gridlock Manhattan

To quantify the broader cyber-physical risks posed by hacking targeted at Internet-connected vehicles, we must investigate how traffic flow in an entire urban street network is affected. Using our percolation-based analytical formula Eq. (4.8), we can directly and immediately compute the likelihood of any road being blocked, which saves significant computational time otherwise required for city-scale agent-based simulations. Thus, we connect road-level traffic dynamics to network-level structure by stochastically marking roads as obstructed according to their percolation probabilities. We can then use tools from network theory to assess the degree of urban disruption due to hacking. While previous studies have investigated urban street network robustness to both random and targeted pruning of edges [143, 144, 145, 146], the consequences of a hack have not been directly explored. The critical advancement introduced by percolation, therefore, is to motivate the pruning of edges based on the underlying traffic features quantified by ρ_H, L, ℓ, and s rather than the bare network structure.

We applied this approach to the island neighborhood of Manhattan, in New York City, USA, using map data from the Open Street Maps tool OSMnx [147]. After fixing the density of compromised vehicles, each road is stochastically set to be accessible or blocked according to the probability calculated with Eq. (4.8), which depends on the length and number of lanes for each road (Methods). Using this method, we quantify the degree to which a hacking event disrupts the city by measuring the city's connectivity. In our analy-

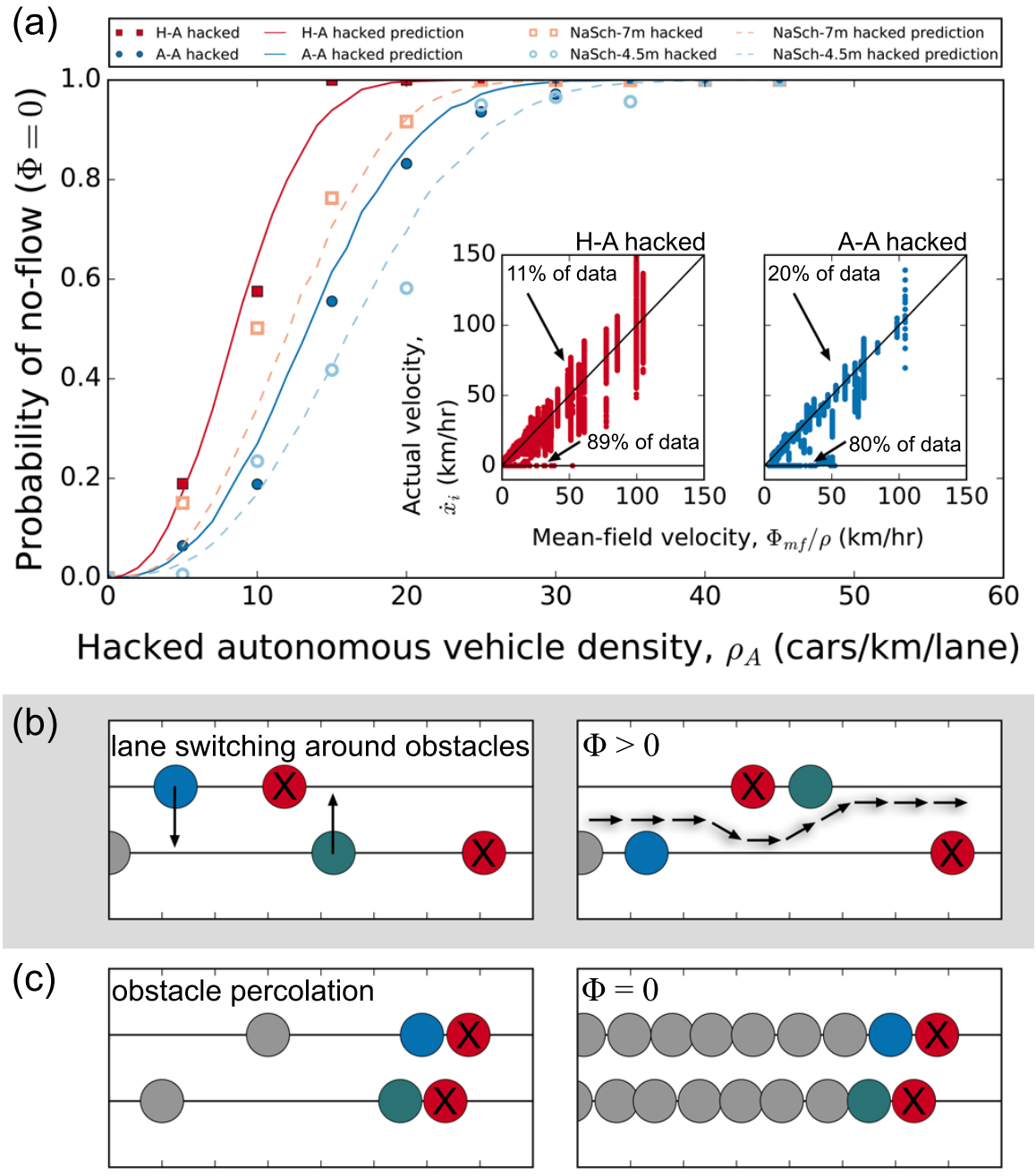

Figure 4.10: Percolation of obstacles is a generic mechanism for loss of flux. Caption continued on subsequent page.

Figure 4.10: Percolation of obstacles is a generic mechanism for loss of flux. (a) Probability of no-flow conditions ($\Phi = 0$) at a given density of disabled autonomous vehicles. Simulation data for combinations of human-driven and hacked-autonomous vehicles (H-A, solid red squares) are consistent with a geometric obstacle percolation prediction (H-A, solid red line). Similarly, simulation data for uncompromised and hacked-autonomous vehicles (A-A, solid blue circles) are consistent with the same geometric percolation prediction (A-A, solid blue line). These findings are reproduced by the Nagel-Schrekenberg cellular automata model with a population of disabled vehicles (red and blue open symbols), and likewise agree with the predictions of geometric obstacle percolation (red and blue dashed lines). Left inset shows the velocity of each human-driven vehicle in H-A simulations versus the mean-field predicted velocity. The data separates onto two lines indicating two discrete outcomes with $\Phi > 0$ (black diagonal line, slope = 1), and $\Phi = 0$ (black horizontal line, slope = 0). Right inset shows the same plot for simulations of all-autonomous vehicles, where only a fraction have been disabled. Here again, we find the same set of discrete outcomes. Cartoon illustrations of model showing (b) how lane switching around non-percolated obstacles allows for flux $\Phi > 0$, and (c) how percolated obstacles lead to a complete loss of vehicle flow ($\Phi = 0$).

sis, a connected component represents a spatial network of roads accessible to each other but not accessible to the rest of the network. The size of each connected component is computed as being equal to the number of accessible street intersections (nodes) within that component. We compute the size of the largest and second largest connected components; when the size of the largest component becomes comparable to the size of the second largest component, the city network has been fragmented [148, 146, 145]. Just as percolated compromised vehicles block individual streets, stochastically blocked individual streets can percolate across the city network [149, 150], which can be described as a percolation-of-percolations event.

We find that for $\rho_H <\approx 10$ compromised vehicles/km/lane, small subnetworks are broken off of the largest connected component (Fig. 4.11a, dark purple lower line). At a critical compromised vehicle density of $\rho_H \approx 13$ compromised vehicles/km/lane, the number of nodes in the second largest connected component reaches its maximal value and is comparable to the number of nodes in the largest connected component. Thus, $\rho_H = 13$ compromised vehicles/km/lane represents the critical point at which there is no longer a substantial network of functional roads that connects points through the city. Above this

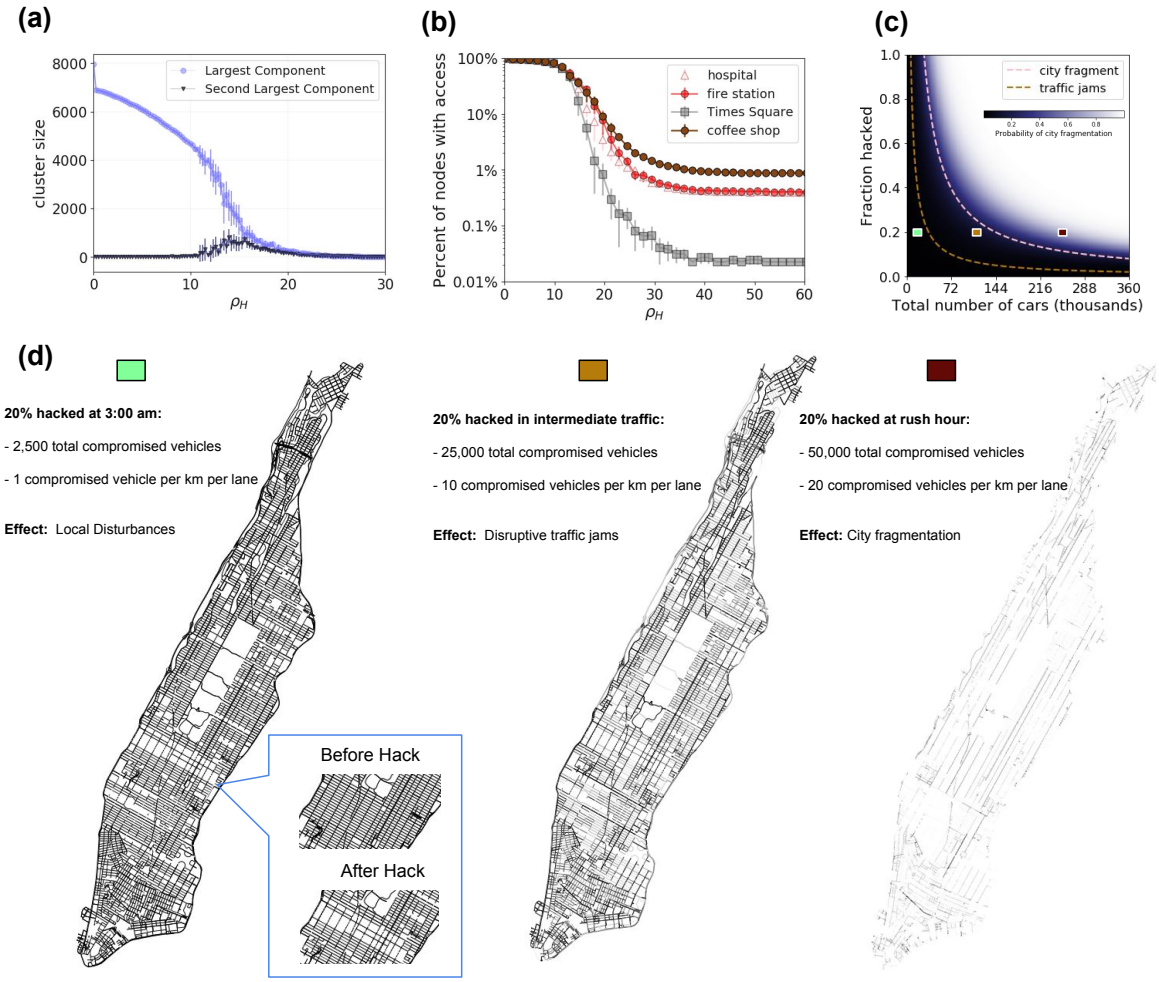

Figure 4.11: Consequences of Internet-connected vehicles being disabled by hacking on a city street network. Caption continued on subsequent page

Figure 4.11: Consequences of Internet-connected vehicles being disabled by hacking on a city street network. (**a**) Size, measured by the number of connected street intersections in the largest and second largest connected components of the street network, as a function of the density of compromised vehicles ρ_H. At the critical compromised vehicle density, $\rho_H \approx 13$ compromised vehicles/km/lane, the size of the second largest component reaches its maximal value and becomes comparable to the size of the largest component. This critical density represents the point at which the network begins to fragment into roughly equal-sized subnetworks, called the point of "city fragmentation." Fluctuations in cluster size increase near the critical point, as expected for percolation-based phase transitions. The jump in cluster size for ρ_H just larger than 0 compromised vehicles/km/lane is due to all single-lane roads being blocked. (**b**) Plot of the fraction of nodes (street intersections) with access to coffee shops, emergency services, and Times Square (a example landmark of interest) as the density of compromised vehicles is varied. (**c**) The horizontal axis is bounded by an estimate for the maximum number of vehicles that can fit bumper to bumper on all the roads of Manhattan island. Hyperbolic contours correspond to constant ρ_H. Pink dashed line corresponds to the critical threshold $\rho_H = 13$ compromised vehicles/km/lane. Dashed orange line corresponds to $\rho_H = 5$ compromised vehicles/km/lane, which is the compromised vehicle density that generally corresponds to the onset of disruptive traffic jams. (**d**) City networks with edges (streets) shaded by the probability that they become totally blocked based on Eq. (4.8). Lighter shades correspond to higher probabilities of obstructions blocking traffic flow. Lower-left inset shows the local disruption that can result from even a small-scale hacking event. Green/orange/red colored rectangles above the city networks correspond to the compromised vehicle density and total number of connected vehicles shown by the identically colored rectangles in (**c**).

compromised vehicle density, the city has fragmented. For $\rho_H \geq\approx 20$ compromised vehicles/km/lane almost all the roads in the city are blocked, and thus we see how compromised vehicles disrupt urban traffic via the percolation-of-percolations.

Along with severe traffic gridlock, access to hospitals and fire stations will be affected in the event of a large-scale hack. To quantify how this disruption affects access to these essential services, latitude and longitude locations of these services were obtained with the Google Places API, and mapped to the closest corresponding intersection in the street network (Methods). At low ρ_H (Fig. 3b, $\rho_H <\approx 10$ compromised vehicles/km/lane), nearly every service is accessible from anywhere in the city. Once city fragmentation occurs, access to services decreases dramatically. At very large ρ_H (Fig. 4.11, $\rho_H \geq\approx 30$ compromised vehicles/km/lane), the only intersections with access to services are the intersections that *contain* the services. At these large densities of hacked, compromised, and disabled vehicles, all the curves plateau to the fraction of nodes with a given service (Fig. 4.11b). For example, if $\approx 0.5\%$ of intersections contain hospitals, the hospital access curve plateaus to 0.5%. We find that, despite emergency services being well distributed throughout the city, access to these services is still dangerously diminished in the event of a large-scale hack.

We quantify the risk of city-wide disruption through the probability of network fragmentation. This probability is defined by the density of compromised vehicles where the size of the second-largest connected component of the street network is maximized. Our measurement of city-wide risk is based on the total number of vehicles on Manhattan roads, and the fraction that are compromised (Fig. 4.11c). We find that when either the traffic density or the fraction of compromised vehicles is very low (number of compromised vehicles $<\approx 2,500$), the probability that compromised vehicles percolate and block individual streets is negligible, so the city grid as a whole remains well connected ($> 95\%$ of edges retained, (Fig. 4.11d, left). Nevertheless, local disruptions can be significant due to stochastic variations. For example, one random instantiation found 2,500 compromised vehicles distributed throughout Manhattan blocked over 70% of roads in the neighborhood just south

of Central Park (Fig. 4.11d, left). While these disruptions are not widespread enough to fragment the city, their impact increases during intermediate traffic conditions due the increased number of mobile and compromised vehicles (Fig. 4.11d, middle). Not surprisingly, the potential for city-wide disruption peaks during rush-hour when traffic density is at its highest and the chances of individual streets being blocked exceeds 50% (Fig. 4.11d, right). The low, medium, and high traffic density regimes considered here (Fig. 4.11d, left to right), correspond to an average probability of blocked roads of less than 25%, greater than 25% but less than 50%, and greater than 50%, respectively (Supplementary Materials). The sensitive dependence of city-wide percolation on ρ_H indicates that the overall risk rapidly increases as it approaches 13 compromised vehicles/km/lane, which ultimately leads to a cascade of consequences from the inability to access most parts of the city.

4.5.4 Large-scale hacking below the percolation threshold

Hacking events that fall below the threshold for city fragmentation can cause significant disruption and danger. As we have already shown, a small-scale hack can stochastically incapacitate a localized region of the city (Fig. 3d, left inset). Alternatively, the same small-scale hack can induce the more familiar phenomenology of clogging simply by disabling a handful of Internet-connected vehicles and waiting for traffic to build up. There are even second-order effects where *both* clogging *and* localized percolation happen *simultaneously*, which could potentially result in even wider disruption due to non-linear interactions between kinetic (clogging) and non-kinetic (percolation) flows.

To better grasp the potential disruption of sub-critical densities of disabled vehicles, we examined post-hack traffic dynamics on a small-scale 5×5 Manhattan-like grid, using the Simulation of Urban Mobility (SUMO) [151] traffic suite (Supplementary Materials). In these simulations, we observed clogging-like kinetic slowing of traffic at densities below the percolation threshold. As expected, the critical threshold for ρ_H at which the average vehicle velocity drops to zero coincides with the emergence of percolation. At higher den-

sities of disabled vehicles, we recover our single-road percolation results where post-hack traffic transitions between flow and no-flow suddenly and abruptly. While sub-percolation simulations can further illuminate time-dependent dynamics, these findings underscore the reality that a percolation-of-percolation event exists within a wider ecosystem of potential hacking-induced traffic disruptions.

Our effort to isolate the specific nature of percolation and distinguish its statistical properties from clogging may appear to underestimate the severity of hacking targeted at Internet-connected vehicles. However, this distinction is critically important for developing risk mitigation, response, and recovery plans that increase infrastructure resilience. For example, a plan that is highly effective for clogging at a sub-critical density of disabled vehicles, may be significantly less effective at larger densities of disabled vehicles, and of course, vice versa. Furthermore, our analytical approach with Eq. (4.8) captures the underlying risk of percolation-based gridlock, while bypassing computationally expensive large-scale traffic simulations. This computational efficiency is appealing for developing real-time recovery plans in the aftermath of a cyber attack where case-specific details can be incorporated in the recovery response. Indeed, with the proliferation of Vehicle-to-Vehicle (V2V) and Vehicle-to-Infrastructure (V2I) connectivity, these challenges are already permeating urban infrastructure. New York City has current plans to install V2V and V2I technology [152, 153], suggesting an urgent need to identify, understand, and plan ahead for the likelihood of vehicle-targeted hacking.

4.5.5 Cyberphysical risks outlook

Quantification is the critical first step in cyber-physical risk mitigation. With the results presented here, we found just ≈ 13 compromised vehicles/km/lane on the Manhattan street network is enough to cause citywide disruption, wherein portions of the city become disconnected from key services. This density corresponds to $\approx 10\%$ of the capacity of the city, or about 30% of all vehicles at intermediate traffic density. From the New York State

vehicle registry, the four largest vehicle manufacturers (Honda, Toyota, Ford, and General Motors) each account for around 10% of the total number of vehicles registered (Supplementary Materials). Thus, if any one of those four manufacturers were compromised during rush hour, it would cause city-wide disruption with probability $> 40\%$. If two manufacturers were compromised, city fragmentation becomes a near certainty, occurring with probability $> 95\%$. Because we have no precedent for large scale cyber-physical hacking, we cannot directly compare these predictions to empirical observations. Indeed, records of traffic accidents across New York City show that there are at most ~ 30 simultaneous accidents, which is far below the percolation threshold [154]. Evidently, the percolation-of-percolations phenomenon described here is a flow phenomenon that is statistically unlikely to occur in conventional conditions, making a cyber-physical hack the only apparent means of observing its occurrence.

As a direct benefit of developing the percolation-of-percolation framework, we have incidentally uncovered an insight useful for developing risk-mitigating strategies. *Using multiple distinct networks for connected vehicle communications technology decreases the number of vehicles that can be compromised in a single malicious cyber-intrusion.* For example, if there were 20 compartmentalized networks in a city, each of which was responsible for 5% of connected vehicles communications, the chance of citywide fragmentation would be low ($< 10\%$) if any one of these networks was hacked. A hacker deliberately seeking to cause a large-scale disruption faced with this compartmentalized multi-network architecture would therefore be required to execute multiple simultaneous intrusions across multiple distinct networks, increasing the cyber-attack's difficulty and making it less likely to occur. In conjunction with conventional cybersecurity strategies, [155, 156] the chances of a percolation-of-percolation event could be effectively reduced to zero. Furthermore, preliminary investigation into dynamics on a 5×5 grid shows that a smaller portion of hacked vehicles below the percolation threshold can cause significant dynamic slowdowns, albeit fundamentally different from percolation where the city is completely gridlocked

(Supplementary Materials). In order to quantify these sub-percolation impacts, future investigations on dynamics taking into account complex city patterns and rerouting of traffic are extremely important.

In this work, we deliberately focused on large-scale effects due to the unique unknowns presented by cyber-attacks targeting vehicles. However, this choice is not meant to discount the significant harm that even a single hacked vehicle can present both to its occupants and to nearby drivers. In terms of the broader traffic flow, we can reasonably surmise a hacked and disabled vehicle would be similar to a conventional break-down. In related scenarios where remote hacking gains control of steering, acceleration, and other vehicle functionality, the impacts could be substantially greater. As such, the easy digital scalability and replicability of hacking means a single well-coordinated cyber-attack would likely surpass any familiar traffic condition. While exploring these technology enabled "unknown unknowns," we must be aware of how unintended blind spots can be exploited so that we can preemptively predict and prevent their harms.

CHAPTER 5
TOPOLOGICAL CONSTRAINTS IN EARLY MULTICELLULARITY FAVOR REPRODUCTIVE DIVISION OF LABOR

5.1 Introduction

The evolution of multicellularity set the stage for an unprecedented increase in organismal complexity [157, 158]. A key factor in the remarkable success of multicellular strategies is the ability to take advantage of within-organism specialization through cellular differentiation [159, 160, 161]. Reproductive specialization, which includes both the creation of a specialized germ line during ontogeny (as in animals and volvocine green algae) and functional differentiation into reproductive and non-reproductive tissues (as in plants, green and red macroalgae, and fungi), may be especially important [162, 163, 164, 165, 166, 167]. Reproductive specialization is an unambiguous indication that biological individuality rests firmly at the level of the multicellular organism [168, 169], and is thought to play an important role in spurring the evolution of further complexity by inhibiting within-organism (cell-level) evolution [170] and limiting reversion to unicellularity [171]. Despite the central importance of reproductive specialization, its origin and further evolution during the transition to multicellularity remain poorly understood [172].

The origin of specialization and sharing has long been of interest to evolutionary biologists, ecologists, and economists. A large body of theory from these fields shows that specialization pays off only when it increases absolute productivity, compared to the case where each individual simply produces what they need [157, 173, 174, 175, 176, 177, 178, 179, 180, 181, 182]. Certain types of trading arrangements maximize the benefits of specialization; highly reciprocal interactions, which facilitate exchange between complementary specialists, amplify cooperation [183, 184]. Still, even when growing in an

ideal spatial arrangement, previous works find that increased specialization and trade is only favored by natural selection when productivity increases as an accelerating function of the degree of specialization, i.e., productivity is a convex, or super-linear, function of the degree of specialization. Conversely, saturating functional returns (i.e., productivity is a concave, or sub-linear, function of the degree of specialization) should inhibit the evolution of specialization [162, 163, 164, 165, 166, 167].

Reproductive specialization differs from classical models of trade in several key respects. Trade between germ (reproductive) and somatic (non-reproductive) cells is intrinsically asymmetric, because the cooperative action, multicellular replication, is not a product that is shared evenly. Selection acts primarily on the fitness of the multicellular group as a whole, which need not be the same as the mean fitness of its component cells [185]. As a result, optimal specialization can result in behaviors that reduce the short-term fitness of some cells within the multicellular group [163, 166], often manifest as reproductive altruism.

Understanding the evolution of cell-cell trade, a classic form of social evolution [186], requires understanding the extent of between-cell interactions. Network theory has proven to be an exceptionally powerful and versatile technique for analyzing social dynamics [187, 188], and indeed, is uniquely well suited to understanding the evolution of early multicellular organisms. When cells adhere through permanent bonds, sparse network-like bodies (i.e., filaments and trees) often result. This mode of group formation is not only common today among simple multicellular organisms, but is the dominant mode of group formation in the lineages evolving complex multicellularity (i.e., plants, red algae, brown algae, and fungi, but not animals).

In this chapter, we develop and investigate a model for how the network topology of early multicellular organisms affects the evolution of reproductive specialization. We find that under a broad class of sparse networks, complete functional specialization can be adaptive even when returns from dividing labor are saturating (i.e., concave / sub-linear). Sparse

networks impose constraints on who can share with whom, which counterintuitively increases the benefit of specialization [172]. By dividing labor, multicellular groups can capitalize on high between-cell variance in fitness, ultimately increasing group-level productivity. Further, we consider group morphologies that naturally arise from simple biophysical mechanisms and show that these morphologies strongly promote reproductive specialization. Our results show that reproductive specialization can evolve under a far broader set of conditions than previously thought, lowering a key barrier to major evolutionary transitions.

5.2 Model

Reproductive specialization can be modeled as the separation of two key fitness parameters, those related to either viability or fecundity, into separate cells within the multicellular organism [189, 169]. Thus, we consider a model of clonal cells living within groups that each invest resources into viability and fecundity. We let v denote each individual's investment into viability, and b denote each individual's investment into fecundity. Each individuals total investment is constrained so that $v + b = 1$. However, an individuals return on its investment is in general nonlinear. Here, we let α represent the 'return on investment exponent: by tuning α above and below 1.0, we can simulate conditions with accelerating and saturating (i.e., convex and concave, or super- and sub-linear) returns on investment, respectively. We let $\tilde{v}$ and $\tilde{b}$ represent a cell's return on viability and fecundity investments, respectively. Following Michod [189, 190], we calculate an individual cell's reproductive fitness as a multiplicative function of $\tilde{v}$ and $\tilde{b}$ (thus, both functions are required for an individual to have nonzero fitness). A single cell's reproduction rate is $w = \tilde{v}\tilde{b} = v^{\alpha}b^{\alpha}$. At the group level, fitness is the total reproduction rate of all cells in the group (i.e., the sum of $\tilde{v}\tilde{b}$ over all cells).

Finally, cells may share the products of their investment in viability with other cells to whom they are connected. For instance, filamentous fungi form networks with citoplas-

mic continuity allowing efficient nutrient translocation between cells [191, 192]. For a given group, the details about who may share with whom, and how much, is encoded in a weighted adjacency matrix $\mathbf{c}$. The element c_{ij} defines what proportion of viability returns individual i shares with individual j. Each individual counts itself among its neighbors, so that $c_{ii} > 0$. Furthermore, since an individual cannot share more viability returns than the total it possesses, we have $\sum_{i=1}^{N} c_{ji} = 1$ for a group of N cells. For the networks we consider, each individual takes a fraction β of its viability returns and shares that fraction equally among all of its n_i neighbors (including itself), and keeps the rest of its returns $1 - \beta$ for itself. Therefore individual i keeps a total fraction of $1 - \beta + \frac{\beta}{n_i}$ of its returns for itself and gives $\frac{\beta}{n_i}$ to each of its non-self neighbors. This means the total amount of returns kept by individual i depends on *both* the network topology and β. When $\beta = 0$ there is no sharing, and when $\beta = 1$ individuals share everything equally among all connections. We refer to β as interaction strength. A given group topology (unweighted adjacency matrix) and β completely specify $\mathbf{c}$.

Within a group of N cells, the overall returns on viability that a given cell enjoys, then, comprises its own returns as well as whatever is shared with it by other members of the group. This can be written as $\tilde{v}_i = v_i^{\alpha}\mathbf{c}_{ii} + \sum_{j \neq i}^{n} v_j^{\alpha}\mathbf{c}_{ji}$, or equivalently, $\tilde{v}_i = \sum_{j}^{n} v_j^{\alpha}\mathbf{c}_{ji}$. Note that this is a column sum, since it describes the total *incoming* viability returns an individual receives as a result of toil and trade. Therefore, we write the group level reproduction rate (i.e., the group fitness) for a group of N individuals as

$$W = \sum_{i=1}^{i=N} \tilde{b}_i \cdot \tilde{v}_i$$
$$W = \sum_{i=1}^{i=N} \tilde{b}_i \sum_{j=1}^{j=N} v_j^{\alpha}\mathbf{c}_{ji}$$

$$W = \sum_{i=1}^{i=N} \sum_{j=1}^{j=N} b_i^{\alpha} \mathbf{c}_{ji} v_j^{\alpha}, \tag{5.1}$$

where all three of the above equations are equivalent. We investigate evolutionary outcomes under this definition of group level fitness for groups with different topologies (who shares with whom), and in scenarios with various return on investment exponents α.

5.3 Results

5.3.1 Fixed resource sharing

We first consider cases wherein cells within a group share across fixed intercellular interactions. Individual i shares v_i^{α} equally among interaction and self terms. In each case we vary the return on investment exponent, α, between 0.5 and 1.5, and the interaction strength, β, between 0.0 and 1.0, both in increments of 0.1. For each combination of topology, α, and β, the group investment strategy (v_i for all i) was allowed to evolve for 1000 generations.

We begin with simple topologies: groups with no connections and groups that are maximally connected. They represent, respectively, the case in which all individuals within the group are autonomous and the case in which every individual interacts with all others (i.e. a 'well-mixed' group). In the absence of interactions, individuals cannot benefit from functions performed by others and therefore must perform both functions v and b; hence specialization is not favored, and does not evolve. In the fully connected case, a high degree of specialization is observed for many values of α and β (figure 5.1a). Consistent with classic results [162, 163, 164, 165, 166, 167], specialization is only achieved in the fully connected case for $\alpha > 1$.

Next, we consider a simple sparse network in which each individual within a group is connected to only two other individuals, forming a complete ring (Fig. 5.1b); we refer to this as the neighbor network. Surprisingly, preventing trade between most individuals encourages division of labor. We find that specialization evolves even when $\alpha < 1.0$, i.e.,

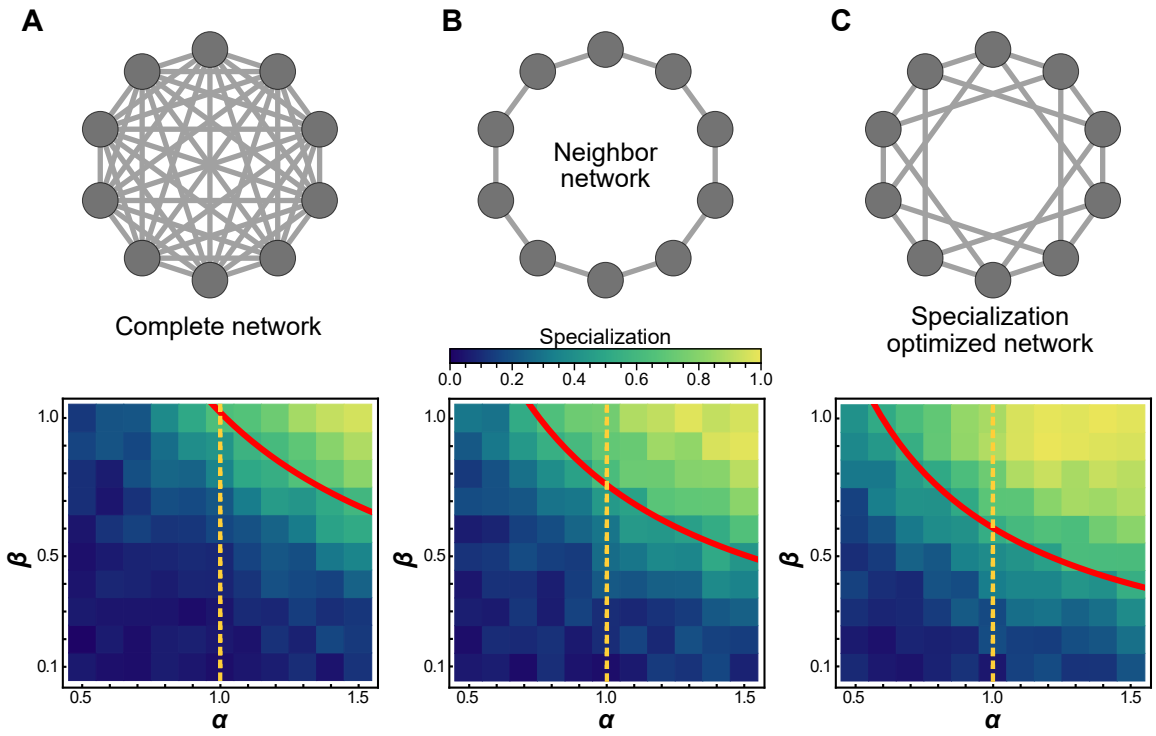

Figure 5.1: Schematic of topology for a simplified six individual group (first row), and mean specialization as a function of specialization power α and interaction strength β across the entire population. (a) When each individual in the group is connected to all others, specialization is favored only when $\alpha > 1$. (b) For the nearest neighbor topology, specialization is favorable for a wider range of parameters, including for some values of $\alpha < 1$. Specifically, specialization is advantageous when $\alpha > \frac{3}{4\beta}$ (see Table 5.1 (c) Connecting alternating specialists creates a bipartite graph which maximizes the benefits of specialization and the range of parameters for which it is advantageous. In this case specialization is favorable wherever $\alpha > \frac{3}{5\beta}$. The red curves represent analytical predictions for α^*, the lowest value of α for which complete generalization is disfavored, and the orange vertical lines are at $\alpha = 1$ to guide the eye. While analysis shows that *some* degree of specialization must occur in the regime upward and to the right of the red curves, simulations reveal that when complete generalization is disfavored complete specialization *is* favored in these networks.

when the returns on investment are saturating or concave. In our simulations, this topology leads to alternating specialists in viability and fecundity (Fig. 5.1b). Analytically, we find that this topology always favors at least some degree of specialization whenever $\alpha > \frac{3}{4\beta}$.

We next study a network with individuals that can be separated into two disjoint subgroups, where every edge of the network connects an individual in one sub-group to an

individual in the other sub-group and no within sub-group connections exist, i.e., a bipartite graph (Fig. 5.1c).

We can analytically determine under what conditions complete generalization is optimal. The complete generalist investment strategy is where every individual in the group invests equally into viability and fecundity, defined as: $v_i^* = \frac{1}{2}$ for all i. For these simple topologies the complete generalist strategy is either a maximum or a saddle point, depending on the values of α and β. Complete generalization is only favored when the Hessian evaluated at the generalist investment strategy $\frac{\partial^2 W}{\partial v_k \partial v_\ell}\big|_{\vec{v}^*} = \mathbf{H}^*$ is negative definite, i.e. all of its eigenvalues are negative. Table 5.1 shows the largest eigenvalues of the Hessian for these topologies. When α and β are chosen so that the largest eigenvalue becomes non-negative, complete generalization cannot maximize fitness.

Table 5.1: Largest eigenvalue of the Hessian evaluated at the generalist critical point as a function of α, β, and N for three topologies.

topology	**largest eigenvalue**
ring graph	$\alpha\left(\frac{1}{2}\right)^{2\alpha-3}(-1+\frac{4}{3}\alpha\beta)$
bipartite graph	$\alpha\left(\frac{1}{2}\right)^{2\alpha-3}(-1+\frac{2N}{N+2}\alpha\beta)$
complete graph	$\alpha\left(\frac{1}{2}\right)^{2\alpha-3}(-1+\alpha\beta)$

While we have not analytically shown where the fitness maximum occurs in cases where the generalist strategy becomes a saddle point, evolutionary simulations (figure 5.1) suggest that when complete generalization is not a fitness maximum, a high degree of (or even complete) specialization typically *does* maximize fitness.

In all cases in which complete specialization is achieved in evolutionary simulations, the self-fitness terms of the viability specialists go to zero, as they cannot reproduce on their own. Furthermore, the fecundity specialists are entirely reliant on the viability specialists for their survival; if viability sharing were suddenly prevented, their fitness would also be zero. This amounts to complete reproductive specialization [162, 186, 189].

5.3.2 Evolving resource sharing

Until now, sharing has been included in every intercellular interaction within groups. Here, we consider the case in which there is initially no sharing, and sharing must evolve along with specialization. These simulations begin with no resource sharing (i.e., $\beta = 0$); during every round, each group in the population has a 2% chance that one of its cells will mutate and β will change. The new β value is chosen from a truncated Gaussian with standard deviation of 10% of the mean, centered on the current value. Whatever is not retained is shared equally across all interactions, including the self term.

Evolutionary simulation results are similar to those from the fixed-sharing model (Fig. 5.5). Saturating specialization (i.e., specialization despite concave return function) still occurs for the two-neighbor and specialization optimized topologies. Thus, for both fixed and evolved resource sharing, we observe specialization for the largest range of parameters (including $\alpha < 1$) not when the group is maximally connected, but rather when connections are fairly sparse. Therefore, a sparse group topology readily constitutes a cooperation-prone physical substrate that can sustain evolvability of specialization traits.

As an example of the benefit of evolving sharing, consider that the maximum fitness according to eq. 5.1 for a group of N disconnected individuals scales as $N\left(\frac{1}{2}\right)^{2\alpha}$. On the other hand, for a bipartite network with a complete specialization strategy (i.e. $\vec{v} = \langle 0, 1, 0, 1, ...\rangle$), the fitness scales as $\left(\frac{N^2\beta}{2N+2}\right)$. The ratio of these fitnesses is $\left(\frac{N^2\beta}{2N^2+2N}\right) 2^{2\alpha} \approx \beta 2^{2\alpha-1}$, where the approximation is for large N. So for larger groups and when $\alpha > \frac{1}{2} - \frac{\log\beta}{2\log 2}$, if a group can evolve resource sharing (i.e. letting $\beta \to 1$ and adopting the specialist investment strategy) its maximum fitness will increase.

5.3.3 Benefit of specialization

We now consider another concrete example to highlight the benefit of specialization. For specialization to be favored, its emergence must result in a higher fitness for the group. To show how this is achieved despite saturating returns, we consider groups of four, con-

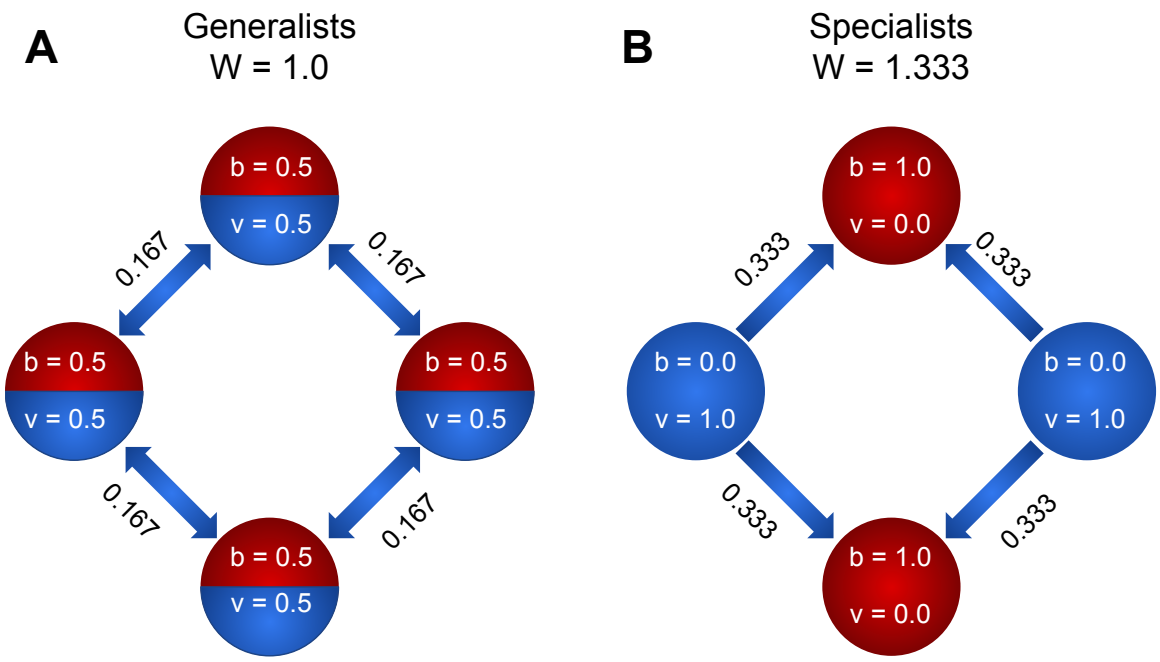

Figure 5.2: To explore how specialization can be favored by the nearest-neighbor topology, we compare the fitness of a four member system when individuals are (a) generalists and (b) specialists. We first consider the case of linear functional returns ($\alpha = 1$). For the case of generalists (a), each individual receives as much viability as it shares, and all nodes contribute equally to the fitness of the group. Therefore, the fitness of the group is $W = 4 \cdot \frac{1}{2} \cdot \frac{1}{2} = 1$. For the case of specialists, however. the viability specialist individuals (blue) have 0 fitness, while the fecundity specialist individuals have nonzero fitness contributions due to the fact that they receive $\frac{1}{3}$ of each viability specialist's output. Thus the fitness of the group is $W = 2(2 \cdot \frac{1}{3}) = \frac{4}{3}$. Thus fitness is higher for the group of specialists, so specialization is favored. For $\alpha = 0.9$, the fitness of generalists is 1.15, and the fitness of specialists is 1.39. Thus, even though the returns on investment are saturating (i.e., concave), specialization is favored.

nected via the nearest-neighbor topology (i.e., in a ring). We directly calculate the fitness of generalists and specialists for two scenarios: $\alpha = 0.9$ and $\alpha = 1$. By summing the fitness contributions of each member, we can calculate the relative fitness of generalists and specialists, and thus determine whether specialization will be favored (Fig. 5.2).

In this simple scenario, reproductive specialization strongly increases group fitness (33% for $\alpha = 1$ and 22% for $\alpha = 0.9$), suggesting an advantage may be found in many systems, even those that are considerably less optimal than the one considered here. For

example, real interactions have costs (e.g., transport costs, loss of shared product, etc.); reproductive division of labor would still be favored as long as those costs do not exceed the benefit of specialization.

The benefit of specialization in ring networks increases with group size. For a ring of size N, fitness under the specialist strategy $\vec{v} = \langle 0, 1, 0, 1... \rangle$ is $W = \frac{\beta}{3}N$. For a ring of generalists the fitness is $W = N(\frac{1}{2})^{2\alpha}$. Therefore, whenever $\alpha > \frac{\log 3 - \log \beta}{2 \log 2}$, the ring of complete specialists enjoys a greater fitness than the ring of complete generalists. Again, note that complete generalization becomes disfavored when $\alpha > \frac{3}{4\beta}$, so there *is* a narrow regime where $\frac{3}{4\beta} < \alpha < \frac{\log 3 - \log \beta}{2 \log 2}$ during which neither complete generalization nor complete specialization is optimal. Numerical optimization and evolutionary simulations suggest that even in this region, however, the specialization score of the optimal strategy is large (fig. 5.1). While these particular topologies do favor specialization even when $\alpha < 1$, we find that the emergence of specialization under these conditions is quite robust to choice of group topology.

5.3.4 Effect of sparsity

Surprisingly, saturating specialization appears to be the rule, rather than the exception, for sparsely connected graphs. We investigated Erdős-Rényi random graphs with varying degrees of connectivity to systematically examine the relationship between sparsity and the value of α at which specialization is favored. We find that many randomly assembled graphs obtain maximum fitness through complete reproductive specialization even when α is below 1 (fig. 5.3 b,c). It is only at the extremes of sparsity and connectivity (near the fully connected or fully unconnected points) that generalists maintain superior fitness for all values of $\alpha < 1$. We further show that this general trend is independent of the size of a group; saturating specialization is favorable for groups of size $N = 10$, $N = 100$, and $N = 1000$. When network connectivity is at its minimum, the group consists solely of isolated individuals that cannot interact. Under these conditions generalists are favored.

Similarly, at maximum connectivity every individual interacts with every other individual. Under these conditions generalists are favored unless $\alpha\beta > 1$. However, when connectivity is small but not zero, specialization arises most readily. We conjecture that the troughs in figure 5.3 c where specialization occurs for the lowest values of α occur when connectivity is just large enough so that a spanning tree is more likely to connect all individuals in the group than not.

5.3.5 Filaments and trees

Sparse topologies like the two-neighbor configuration have significant biological relevance, and direct ties to early multicellularity. The first step in the evolution of multicellularity is the formation of groups of cells [157, 194, 195, 196, 197]. Simple groups readily arise through incomplete cell division, forming either simple filaments (Fig. 5.4a) or tree-like morphologies (Fig. 5.4b) [198, 199, 200, 201]. Filament topologies have been widely observed in independently-evolved simple multicellular organisms, from ancient fossils of early red algae [202](Fig. 4a) to extant multicellular bacteria (i.e. cyanobacteria from the genus *Anabaena*). Branching multicellular phenotypes have also been observed to readily evolve from baker's yeast [203](Fig. 4b), and are reminiscent of ancient fungus-like structures [204] and fossils from early Ediacaran [199].

Simulations of populations of groups with filamentous and branched topologies reveal that specialization is indeed favored in the sub-linear regime (Fig. 5.4a and 5.4b). While the generalist strategy is never a critical point for these networks (which have $\mathbf{c} \neq \mathbf{c}^T$, see methods), we conjecture that there is a nearby critical point which maximizes fitness at small values of α and becomes unstable at larger values of α. We introduce a new metric, α^*, defined as the value of α such that the largest (least negative) eigenvalue of the Hessian evaluated at the complete generalist strategy is zero when $\beta = 1$. For topologies in which each member has the same number of neighbors, α^* is a critical value at which generalization is no longer an optimal strategy. However, even for groups where the number of

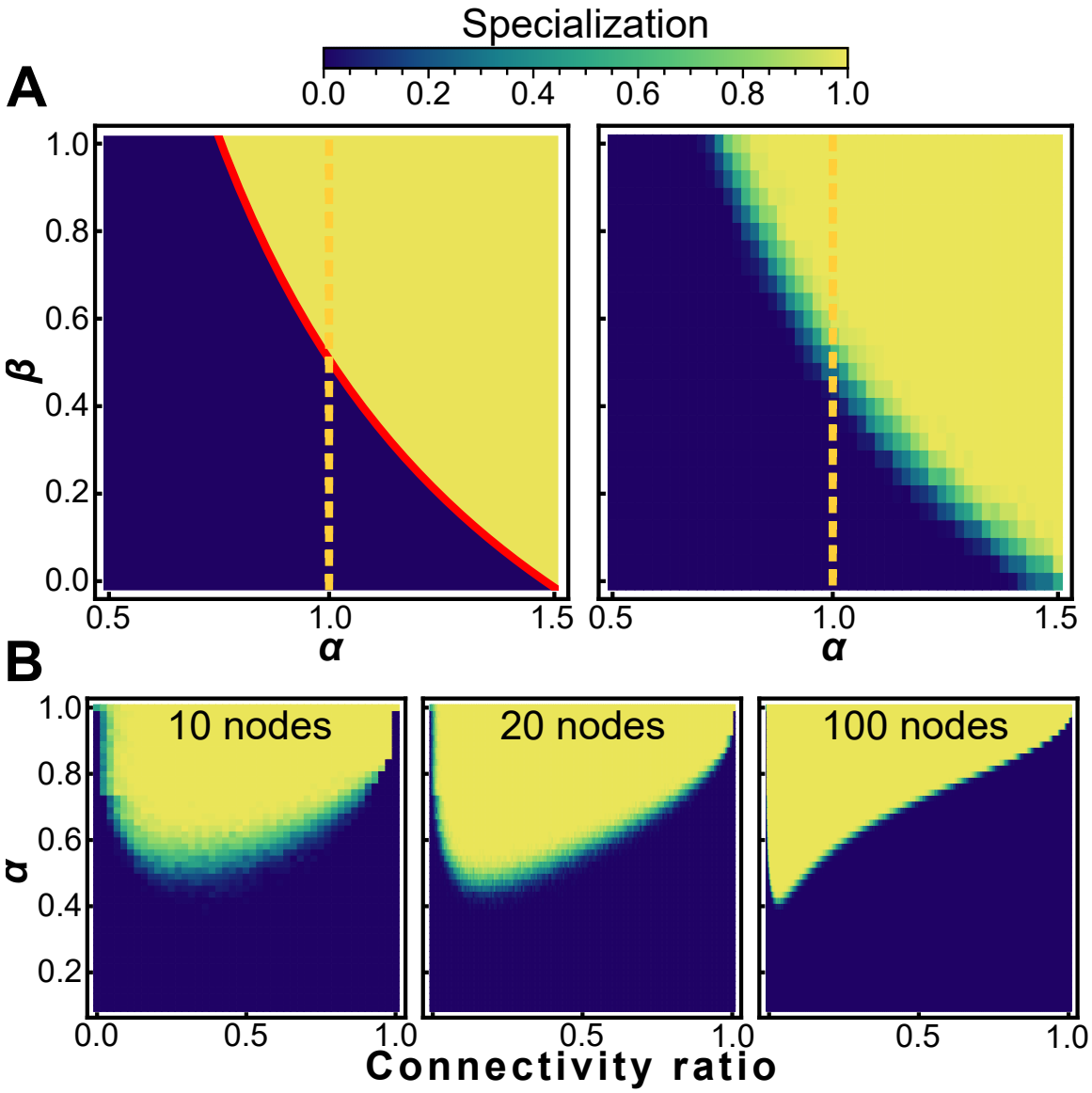

Figure 5.3: Sparsity encourages specialization. Heat maps showing conditions that favor specialists (white) and generalists (black) for nearest neighbor topologies (a) and randomly generated graphs with the same connectivity as nearest neighbor topologies (b). Specialization is adaptive on a neighbor network for $\alpha > \frac{3}{4\beta}$; random networks with the same mean connectivity as the nearest neighbor topology behave similarly. (c) The sparsity of a random graph affects how likely it is to favor specialization. We numerically maximize fitness for random graphs of size $N = 10$ (left), $N = 20$ (middle), and $N = 100$ (right) at different levels of sparsity, and subsequently measure the specialization $\mathcal{S}$ of the fitness maximizing investment strategy. The horizontal axis is the number of connections divided by the maximum possible number of connections. The vertical axis is the specialization power α, and the colormap shows mean specialization.

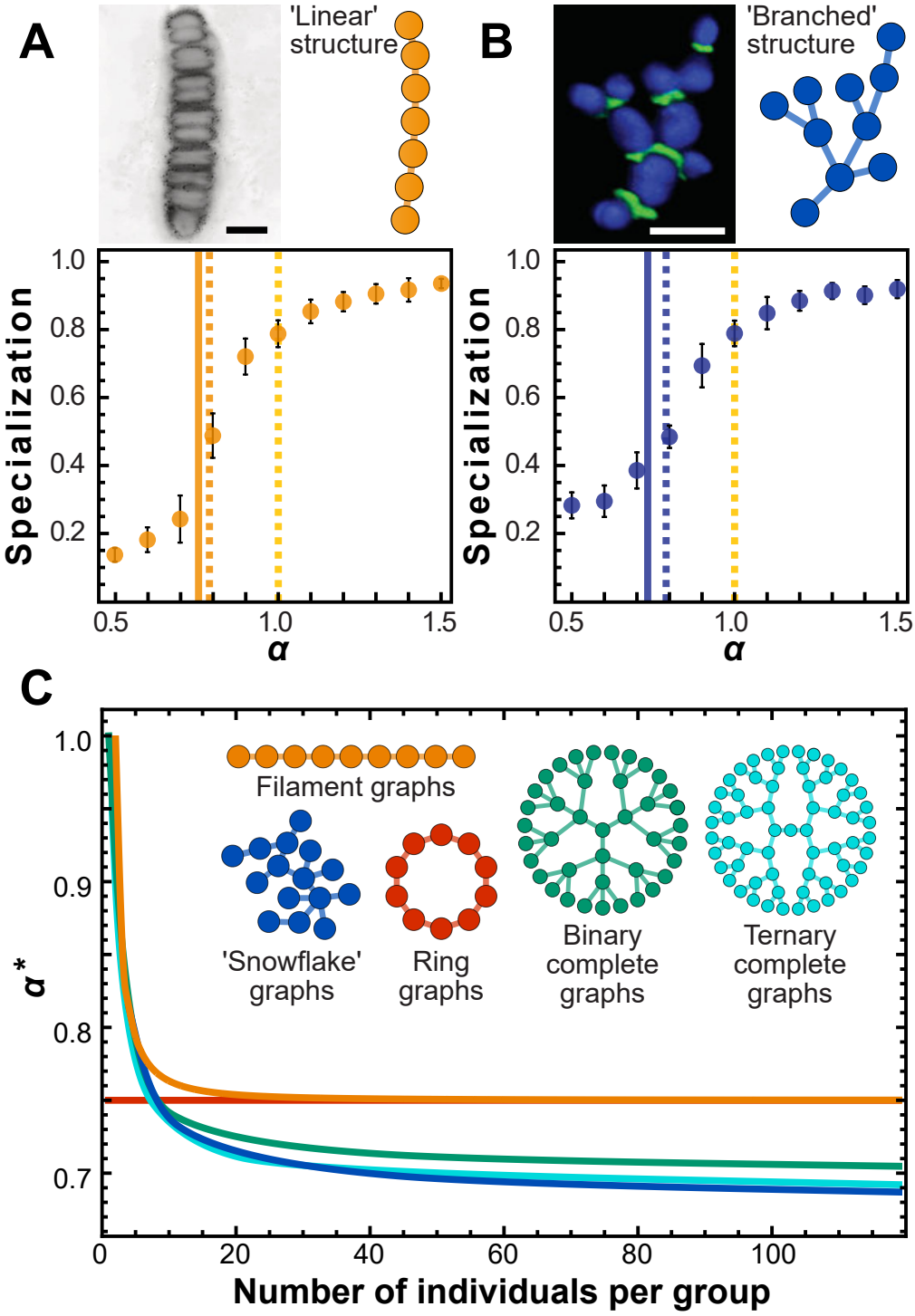

Figure 5.4: Simple multicellular organisms with sparse topologies. Caption continued on subsequent page.

Figure 5.4: Simple multicellular organisms with sparse topologies. We show two examples of simple multicellular organisms with linear and branched topologies. The image in (a) is a fossilized rhodophyte specimen of *Bangiomorpha pubescens*, courtesy of Prof. Nicholas Butterfield (see e.g. [193]; the image in (b) is a confocal image of 'snowflake yeast' showing cell volumes in blue and cell-cell connections in green. Scale bars in both panels $= 10\mu$m. Panels include cartoons depicting simplified topologies. Topologically similar to the two-neighbor configuration, these configurations yield similar simulation results. Specialization is plotted as a function of α. Solid green (a) and blue (b) vertical lines indicate analytical solutions for the transition point where the Hessian evaluated at $\vec{v} = \frac{1}{2}\vec{1}$ stops being negative definite, i.e. α^*; dotted lines indicate roughly where the simulation curves cross specialization of 0.5, i.e. the "true" transition value of α where specialization becomes favored. (c) To further explore trees and filaments we analytically solved for α^* for various types of trees and filaments of different sizes. (d) $\alpha*$ is plotted versus group size for several topologies. This is a proxy measure of how amenable a network structure is to specialization.

neighbors for each cell varies, we can still use α^* as a proxy for how amenable a topology is to saturating specialization. The smaller α^*, the more specialization is likely to be favored. We plot vertical lines where $\alpha = \alpha^*$ (solid green fig 5.4(a) and blue fig 5.4(b)), and dotted lines to indicate roughly where the simulation curves cross specialization of 0.5. This shows that using α^* as an overall metric for how amenable a network is to saturating specialization is a reasonable approach— at least in this case. This metric α^* only depends on topology and can in principle be calculated analytically given any network. We examined the value of α^* as filaments and a variety of tree-like structures grow larger, and find that specialization becomes more strongly favored (Fig. 5.4c and d). While group size has no effect on specialization for some topologies, like the circular lattice, filaments and trees all see a decrease in $\alpha*$ as group size increases. Once these topologies are larger than a few tens of cells, there appears to be little added benefit to increased group size in terms of specialization. Simple and easily accessible routes to multicellular group formation can readily evolve in response to selection for organismal size [201], and this process may also strongly favor the evolution of cellular differentiation [205, 206, 207, 196].

5.4 Discussion

During the evolution of multicellularity, formerly autonomous unicellular organisms evolve into functionally-integrated parts of a new higher-level organism [167, 208]. Once integrated into a group setting, these cells will differentiate into specialists only if group fitness is increased by doing so. Evolutionary game theory [175, 209, 210] argues that functional specialization should only stably evolve when increased investment in trade increases reproductive output. Conventionally, this requires returns from specialization to be accelerating, i.e, convex or super-linear [157, 173, 174, 175, 176, 177, 178, 179, 180, 181]. While this idea is intuitive, it is, in the case of fixed group topology, also overly restrictive. In this paper, we explore how social interactions within groups, measured by their network topology, affect the evolution of reproductive specialization. Indeed, when all individuals within groups interact (with equal interaction strength), benefits must be super-linear for specialization to evolve [157, 173, 175, 162]. Yet for a broad class of sparsely-connected networks, complete specialization can evolve even when the fitness function is saturating, i.e., concave (figure 5.3).

Rather than being unusual, networks favoring specialization readily arise as a consequence of physical processes structuring simple cellular groups [183]. For example, septin defects during cell division create multicellular groups with simple graph structures (Fig. 5.4 a and b), where cells are connected only to parents and offspring [198, 199, 201, 211]. If cells share resources only with physically-attached neighbors, then the physical topology of the group describes its interaction topology, and these networks strongly favor reproductive specialization.

Disentangling the evolutionary underpinnings of ancient events is notoriously difficult. Still, it is worth examining the independent origins of complex multicellularity, which are independent runs of parallel natural experiments in extreme sociality. Complex multicellularity (large multicellular organisms with considerable cellular differentiation) has evolved

in at least 5 eukaryotic lineages, once each in the animals [212], land plants [213], and brown algae [214], twice in the red algae [215], and 8-11 times in fungi [216]. In all cases other than animals, these organisms form multicellular bodies via permanent cell-cell bonds, creating long-lasting highly structured populations. Both fossil and phylogenetic evidence suggests that early multicellular organisms in these lineages were considerably simpler, growing as relatively simple graph structures. For example, 1.2 billion year old red algae formed linear filaments of cells [202], basal multicellular charophyte algae form circular sheets of cells radiating from a common center [213], the ancestor of the brown algae likely formed a branched haplostichous thallus that was either filamentous or pseudoparenchymatous [214], and filamentous fungi are primarily composed of linear chains.

Finally, our model of complete trade specialization could apply directly or with slight modification to systems in which 1) only the aggregate productivity of the group is maximized, 2) the productivity of each individual within the group is a multiplicative function of returns on investment into two (or more) tasks, and 3) there is an asymmetry in how products of those investments are shared. The main difference between our work and previous investigations of the effect of group topology on specialization is that we consider the productivity of groups as a whole, not the individuals within them, and we consider situations of highly asymmetric sharing.

5.5 Conclusion

We explored the evolution of reproductive specialization in groups with various topologies. Our results demonstrate that group topological structure likely plays a key role in the evolution of reproductive division of labor. Indeed, within a broad class of sparsely connected networks, specialization is favored even when the returns from cooperation are saturating, i.e., concave; this result is in direct contrast to the prevailing view that accelerating, i.e., convex, returns are required for natural selection to favor increased specialization [162, 163, 164, 165, 166, 167]. Further, we find that saturating specialization is favorable for a

broad class of scenarios in which the degree of sharing is asymmetric, and the interaction topology is sparse.

Our results support the emerging consensus that evolutionary transitions in individuality are not necessarily highly constrained [201, 217, 197, 160, 218, 219, 220]. While further work is required to define general patterns in the evolution of biological complexity and the major evolutionary transitions, our results suggest that some non-adaptive processes, such as topological group-level structure, are fundamental mechanisms upon which natural selection and other adaptive processes can act, paving the way for the origin of new levels of biological organization.

5.6 Methods

5.6.1 Analysis

The gradient of the fitness with respect to the group investment strategy $\vec{v}$, is

$$\frac{\partial W}{\partial \vec{v}} = \sum_{k=1}^{N} \hat{e}_k \alpha \left(v_k^{\alpha-1} \sum_{j=1}^{N} c_{kj}(1-v_j)^{\alpha} - (1-v_k)^{\alpha-1} \sum_{j=1}^{N} c_{jk} v_j^{\alpha} \right) \tag{5.2}$$

where $\hat{e}_k$ is a unit vector in the k^{th} direction. First notice that if $\mathbf{c} = \mathbf{c}^T$, and $\vec{v} = \frac{1}{2}\vec{1}$ where $\vec{1}$ is a vector of ones, then the gradient is zero. This strategy, $\vec{v} = \frac{1}{2}\vec{1}$, corresponds to the 'generalist' approach, where every individual invests equally into both tasks. Call it the generalist strategy. Second, notice that if $\mathbf{c} \neq \mathbf{c}^T$ then the gradient is *not* zero under the generalist strategy, so at least some degree of specialization must be necessary to maximize fitness. To determine the stability of this solution we examine $\mathbf{H}^*$, the Hessian evaluated at the generalist critical point. If $\mathbf{H}^*$ is negative definite, then the generalist strategy is a fitness maximum and is therefore an optimal strategy. If, on the other hand, $\mathbf{H}^*$ has both

positive and negative eigenvalues then the generalist strategy lies at a saddle point within the fitness landscape, and therefore the optimal strategy must be somewhere else in (or on the boundary of) the domain (i.e. $v_i \in [0,1]$ for all $i \in 1,2,...N$). Finally, note that $\mathbf{H}^*$ is never positive definite since $\vec{1}$ is always an eigenvector with negative eigenvalue (when $\mathbf{c} = \mathbf{c}^T$).

We also use the zero crossing of the largest eigenvalue of $\mathbf{H}^*$ evaluated at $\vec{v} = \frac{1}{2}\vec{1}$ and $\beta = 1$ as an overall measure of how amenable a network is to specialization, even when $\mathbf{c} \neq \mathbf{c}^T$.

Hessian

The Hessian $\frac{\partial^2 W}{\partial v_k \partial v_\ell}$ is

(5.3)

Of particular interest for us is the value of the Hessian at the generalist strategy when $\mathbf{c} = \mathbf{c}^T$. In that case

$$\mathbf{H}^* = \alpha \left(\frac{1}{2}\right)^{2\alpha-3} \Big[-\alpha\beta\mathbf{a} + (\alpha\beta - 1)\,\mathbf{I} \Big]. \tag{5.4}$$

where $\mathbf{a}$ is the row-normalized adjacency matrix of the network. If $\mathbf{A}$ is the network's adjacency matrix then

$$a_{ij} = \frac{A_{ij}}{\sum_{j=1}^{N} A_{ij}}.$$

The case when $\mathbf{c} = \mathbf{c}^T$

As noted above, when $\mathbf{c} = \mathbf{c}^T$, the generalist strategy is always a critical point where $\frac{\partial W}{\partial \vec{v}} = 0$. To determine the stability of this solution we examine $\mathbf{H}^*$ (eq. 5.4). If $\mathbf{H}^*$ is negative definite, then the generalist strategy is a fitness maximum and is therefore an optimal strategy. If, on the other hand, $\mathbf{H}^*$ has both positive and negative eigenvalues

then the generalist strategy lies at a saddle point within the fitness landscape, and therefore the optimal strategy must be somewhere else in (or on the boundary of) the domain (i.e. $v_i \in [0,1]$ for all $i \in 1,2,...N$). Finally, note that $\mathbf{H}^*$ is never positive definite (when $\mathbf{c} = \mathbf{c}^T$). Consider $\mathbf{H}^*\vec{1}$:

$$\mathbf{H}^*\vec{1} = \alpha\left(\frac{1}{2}\right)^{2\alpha-3}\left[-\alpha\beta\mathbf{a}\vec{1} + (\alpha\beta - 1)\,\mathbf{I}\vec{1}\right]$$
$$\mathbf{H}^*\vec{1} = \alpha\left(\frac{1}{2}\right)^{2\alpha-3}\left[-\alpha\beta\vec{1} + (\alpha\beta - 1)\,\vec{1}\right]$$
$$\mathbf{H}^*\vec{1} = -\alpha\left(\frac{1}{2}\right)^{2\alpha-3}\vec{1}$$

We have $\mathbf{a}\vec{1} = \vec{1}$ since $\mathbf{a}$ is row-normalized. Furthermore, $\alpha > 0$, so $\vec{1}$ is always an eigenvector of $\mathbf{H}^*$ with a negative eigenvalue.

We can next ask, under what conditions is $\mathbf{H}^*$ negative definite? This will depend on the group topology, the nonlinear returns on investment α, and the interaction strength β. We examine three cases: the ring graph, the bipartite graph, and the complete graph.

Table 5.2: Largest eigenvalue of the Hessian evaluated at the generalist critical point as a function of α, β, and N for three topologies. When the group size $N = 4$, the bipartite graph coincides with the ring graph, and indeed the eigenvalues agree. Similarly, when $N = 2$ the bipartite graph coincides with the complete graph and the eigenvalues agree. The interesting domain of $\alpha\beta$ is $(0,1]$, so for the complete graph $\mathbf{H}^*$ is always negative definite. However, the bipartite and ring graphs show regions where the generalist strategy is *not* stable.

topology	**largest eigenvalue**
ring graph	$\alpha\left(\frac{1}{2}\right)^{2\alpha-3}(-1+\frac{4}{3}\alpha\beta)$
bipartite graph	$\alpha\left(\frac{1}{2}\right)^{2\alpha-3}(-1+\frac{2N}{N+2}\alpha\beta)$
complete graph	$\alpha\left(\frac{1}{2}\right)^{2\alpha-3}(-1+\alpha\beta)$

When $\mathbf{c} = \mathbf{c}^T$, the matrix $\mathbf{H}^*$ is a special type of matrix called a circulant matrix, with well known properties. Its eigenvalues are given by the discrete Fourier transform of its first row. The k^{th} eigenvalue is

$$\lambda_k = \sum_{j=0}^{N-1} H^*_{1j} e^{\frac{2\pi i}{N} jk}$$

For the ring topology with $N = 10$, for example

$$\lambda_k = \alpha \left(\frac{1}{2}\right)^{2\alpha-3} \left((-1 + \frac{2\alpha\beta}{3}) - \frac{\alpha\beta}{3} e^{\frac{\pi i}{5} k} - \frac{\alpha\beta}{3} e^{\frac{9\pi i}{5} k}\right)$$

Which has its maximum when $k = 5$,

$$\max_k \lambda_k = \alpha \left(\frac{1}{2}\right)^{2\alpha-3} (-1 + \frac{4\alpha\beta}{3})$$

The maximum eigenvalue for the bipartite and complete graphs can be computed similarly.

5.6.2 Evolutionary simulations

Our evolutionary simulations maintain the same overall structure as the Wright-Fisher model: a discrete-time Markov chain framework with fitness-weighted multinomial sampling between generations and constant population size. Therefore we refer to them as Wright-Fisher evolutionary simulations. We initialize a population of $\mathcal{N} = 1000$ groups, each of group size $N = 10$, with uniform random investment strategies. We then let them evolve for 1000 generations, selecting offspring according to the relative fitness of each group (see eq. 5.1). At each generation there is a 2% chance for a mutation to a given group's investment strategy $\vec{v}$. If a mutation occurs, a new investment strategy is selected from a truncated multivariate gaussian distribution centered at the current (pre-mutation) investment strategy and with standard deviation equal to $\frac{1}{10}\vec{v}$. After mutations each group's fitness is calculated according to eq. 5.1, and the population is ranked according to fitness. Finally, $\mathcal{N}$ groups are selected (with replacement) to populate the next generation, according to a multinomial distribution weighted by the groups' fitness *ranks*.

5.6.3 Measuring specialization

To quantify the degree of specialization associated with a given group's optimal investment strategy— the one which maximizes the fitness— we introduce the following metric, which we refer to simply as "Specialization":

$$\mathcal{S} = \frac{2}{N} \sum_{i=1}^{N} \left(\max(v_i, 1 - v_i) - \frac{1}{2} \right) \tag{5.5}$$

Specialization ranges from 0 (for groups consisting of cells investing equally in functions v and b) to 1 (for groups consisting of cells investing exclusively in either function

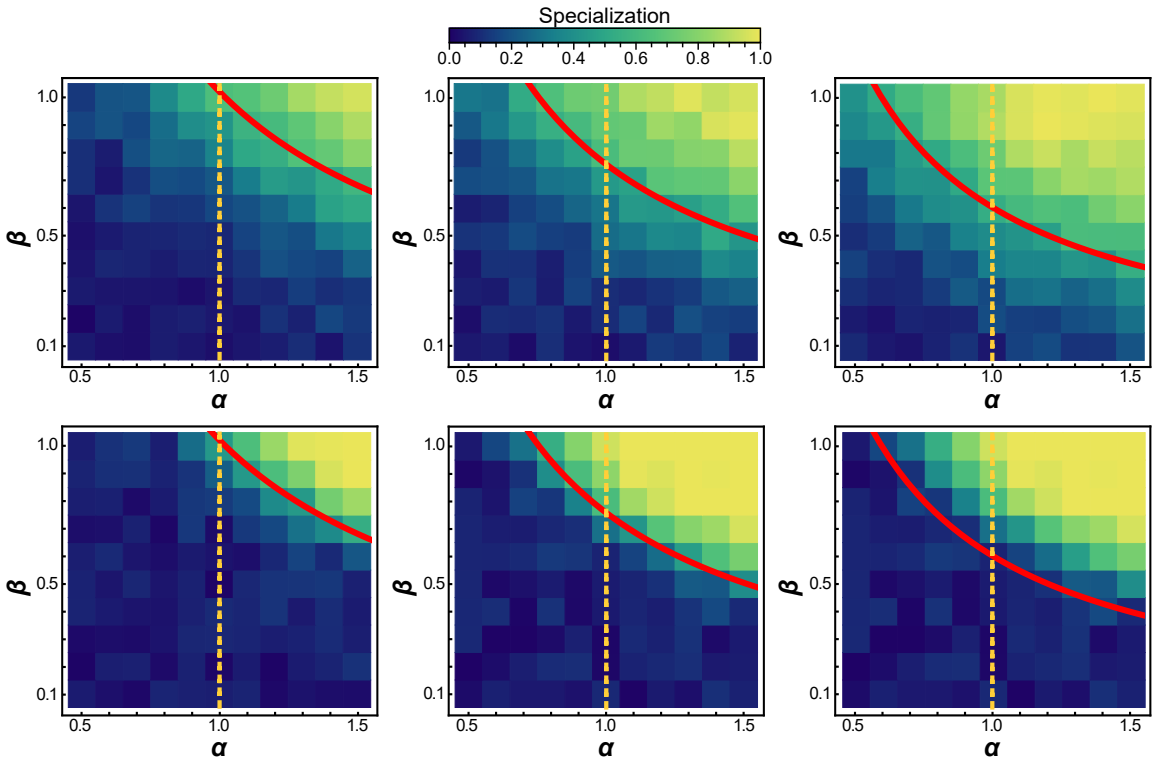

Figure 5.5: Simulation results for different quantiles of fitness. Mean specialization as a function of specialization power α and interaction strength β for groups of size ten of the same topologies investigated in the main text across the entire population (top row) and of the fittest (bottom row) of 1000 groups after 1000 rounds of selection. (a) When each individual in the group is connected to all others, specialization is favored only when $\alpha > 1$. (b) For the nearest neighbor topology, specialization is favorable for a wider range of parameters, including for some values of $\alpha < 1$. Specifically, specialization is advantageous when $\alpha > \frac{3}{4\beta}$. (c) connecting alternating specialists maximizes the benefits of specialization and the range of parameters for which it is advantageous. In this case specialization is advantageous wherever $\alpha > \frac{3}{5\beta}$. The red curves represents an analytical prediction for where specialization becomes favorable, and the orange vertical lines are at $\alpha = 1$ to guide the eye

Appendices

APPENDIX A

BACTERIA

A.1 Biofilm simulations

I've developed several biofilm simulations that are all based on the framework of individual-based-modelling [221, 17, 18, 19]. Since the role of the simulations is elucidating the physics of biofilms, they are intentionally designed to be biologically minimal. By attempting to capture relevant observed behavior with as few added details as possible, we avoid the problem of overfitting and thereby increase the ability of the simulations to generalize. The added bonus is that the later task of connecting the microscopic behavior to observed macroscopic behavior becomes easier.

For different experiments, it was necessary to use different types of simulations. I've used three different biofilm simulators as the basis for comparison with experiments, with additional modifications and tweaks to each as necessary.

A.1.1 Off lattice biofilm simulations

The off lattice simulations allow us to independently tune experimentally inaccessible parameters, such as killing rate, as well as to directly investigate dynamics at the single-cell level. Briefly, the biofilm is represented as a collection of bacterial cells distributed in either a three or two-dimensional continuous domain. The state of the biofilm is fully characterized by the center positions of spheres (circles in 2D) that represent bacteria, and which may overlap. The following processes are simulated:

Motion: Overlapping cells are treated as "neighbors" in direct contact, and as such

experience a repulsive force linear in the extent of overlap. The force on the i$^{\text{th}}$ cell is then:

$$\vec{f}_i^{\text{growth}} = -k \sum_{j \in \text{neighbors}} \vec{r}_j - \vec{r}_i$$

The spring constant k is roughly in agreement with literature values taken from AFM measurements [27]. The the i$^{\text{th}}$ cell is then subject to the growth force and a viscous damping:

$$m\ddot{\vec{r}}_i = -\gamma m\dot{\vec{r}}_i + \vec{f}_i^{\text{growth}}$$

The overdamped limit is taken, as the Reynold's number is very small [222], and so inertial effects are ignored.

$$\dot{\vec{r}}_i = \frac{-k}{m\gamma} \sum_{j \in \text{neighbors}} \vec{r}_j - \vec{r}_i$$

with the Stokes-Einstein relation $\gamma = 6\pi\eta R_i$. Here, R_i is a cell diameter, and is set to 1μm, η is the dynamic viscosity set to that of water ($\eta = 8.9 \times 10^{-4}$Pa $\cdot$ s) as an order of magnitude estimate, and the mass of a cell is set to the mass of a 1 micron sphere of water ($m = 4 \times 10^{-15}$kg). Note that the effective viscosity of the overall biofilm (cells + background) could still be different than the chosen viscosity of the background fluid that damps cell motion. Cell positions are updated using forward Euler integration, so that

$$\vec{r_i^t} = \vec{r_i^{t-1}} + dt \cdot \frac{-k}{m\gamma} \sum_{j \in \text{neighbors}} \vec{r_j^{t-1}} - \vec{r_i^{t-1}}$$

If the parameters are set as above, then we can interpret our results in terms of real units. That is, each simulation update advances the clock by dt seconds. However, often we are interested in scaling behavior and qualitative results, so we instead collapse $\frac{-k}{m\gamma}$ into an tuneable constant that adjusts the rate at which dynamics occurs and report results in

arbitrary units.

Growth: Cells grow at a constant volume (area) per time. After a completed reproduction event, the mother cells volume (area) resets to its initial value.

Reproduction: To best replicate cellular division via binary fission, cells reproduce with a probability that grows linearly in time. A daughter cells center position is seeded at a random point on the surface (perimeter) of the mother cell. Once the daughter cell is seeded, the mother cell returns to its original size. The time scale is set by the expected time to reproduce (about 20 minutes for V. cholerae). We simulated reproduction through two different strategies. In the first, any cell in the system is free to reproduce once it has grown large enough. While this approach is not identical to reproduction in biofilms, it was chosen to demonstrate that a minimal model reproduces experimentally observed phenomenon. In tracer bead simulations, we only allowed reproduction to occur for cells with the 5% smallest z-positions. This replicates the behavior of real biofilms on agar surfaces, for which reproduction occurs more near the agar surface where the nutrient concentration is the highest. This also speeds up the rate at which tracer beads approach the top surface of the biofilm. However, limiting reproduction to the bottom layer does not qualitatively change the other simulation results.

T6SS killing and random death: Cells are removed from the biofilm by random death with a probability that is constant in time. To simulate T6SS killing, two different bacterial strains with different T6SS effectors are introduced. A cell is removed from the biofilm due to T6SS killing with a probability that is linear in the number of enemy cells within a 2 radius neighborhood of itself. All other cellular processes, such as secretion of biofilm, are left out of the simulation. Thus, the entire biofilm structure is a result of changes in constituent number and mechanical interactions between cells. With this biologically minimal framework, we recapitulate the fluidization of biofilms and the behavior of the height correlation predicted by [3], and measured in our biofilms.

All simulations were written and implemented in Processing, a free and open source

programming language and integrated development environment built on Java [223].

For investigations of domain coarsening, we found that the off lattice biofilm behaved similarly to a yet simpler approach, namely cellular automata or a lattice simulation.

A.1.2 Lattice biofilm simulations

Whereas the off-lattice biofilm simulation models cells that interact via forces and can take on any position that can be represented by floating point numbers, the lattice simulation more closely resembles a cellular automaton model where discrete grid sites are updated according to an abstract rule set. However, the key cellular behaviors (other than motion) that are modeled are the same.

Reproduction: Each lattice site maintains an integer state s; either it is empty ($s = 0$) or it is occupied by a cell of a given type $s \in \{1, 2, ...\}$. If a lattice site is empty and it is neighbored by non-empty sites, it will change its state to the type of one of its neighbors with a probability proportional to the proportion of that type of cell in the neighborhood.

$$P_{s \to s'} = \frac{\sum_j \delta(s_j = s')}{\sum_j 1 - \delta(s_j = 0)}$$

Where j runs over the 1 site radius neighborhood, and s_j is the state of the jth neighbor site. In other words, we count the number of non-empty neighbors of type s' as well as the total number of non-empty neighbors. The probability that an empty site transitions to type s' is the ratio of these two counts.

T6SS killing and random death: A cell's state can return to 0 (empty) due to T6SS killing with a probability that is linear in the number of enemy cells within a 1 site radius neighborhood of itself.

$$P_{s' \to s''} = \frac{\sum_j \delta(s_j = s'')}{\sum_j 1 - \delta(s_j = 0)}$$

To model differences in bacterial strains' killing ability, we sometimes weight this prob-

ability by a constant factor for each strain. Furthermore, in some versions of the simulation we introduce a probability of random death, where a site's state can revert to 0 with some small constant probability.

The algorithm for the lattice individual-based-model (LIBM) approximates demixing in a system of mutual killing *V. Cholerae*, and has been shown [28] to agree well with experimental results.

In the LIBM, each bacterium can have up to $2z$ nearest neighbors, for a dimensionality z, and the probability of dying via T6SS at a given time is linear in the number of enemy neighbors. Every site, v, in the lattice has a color, (e.g. 'red', 'green', or 'empty') and a neighborhood consisting of the lattice sites directly above, below, to the left, and to the right, of site v. Then the update rules for site v at a given time will be:

```
for w in neighborhood(v):
    if Color(w) is not Color(v):
        enemy_count+=1
if (enemy_count/4)>random.random():
    Color(v)='empty'
```

The sites are updated sequentially at random. That is, at each time step a site is picked uniformly at random to be updated.

The time evolution of the overall lattice state can be viewed as a Markov Chain, however this is not a particularly fruitful approach in our case. If you have a Markov chain that usually implies that there should be a unique stationary distribution that is independent of initial conditions. However, this Markov chain is not irreducible, meaning that it is not possible to get from any state to any other state via a series of single step transitions. If the entire lattice is filled with one type of bacteria and other types have gone extinct, it is impossible to "revive" them. This absorbing state is the inevitable fate of any LIBM simulation run long enough, where the strain with the highest killing ability takes over the whole grid. If the strains have equal killing abilities then one of them (randomly or ac-

cording to initial conditions) takes over the entire grid. These fixation probabilities could maybe be calculated (we basically have a biased random walk with absorbing states and we start at some known configuration, the tricky part is that local spatial structure becomes important). But these fixation probabilities are not really the most interesting quantities to chase. The reason for this is that the mixing time for this Markov Chain is very large compared to the number of generations a real biofilm could reasonably be expected to persist in laboratory conditions. That is also why initial conditions are interesting to investigate here. For example, as discussed in the chapter 2, initializing the simulation via the coffee ring effect has a large impact on spatial structure and genotype frequency even after many generations.

This simulation can also be cast as a continuous scalar field model. We start with the introduction of a scalar-valued parameter ϕ. For example, for two colors:

$$\phi(v) = \begin{cases} 1, & \text{if } color(v) \text{ is red} \\ 0, & \text{if } color(v) \text{ is empty} \\ -1, & \text{if } color(v) \text{ is green} \end{cases}$$

If the discrete simulation above is now cast in the language of the parameter ϕ, instead of each site being labeled with a color or empty, it is labeled with a value of the parameter ϕ:

```
enemy_count=4*phi(v)
for w in neighborhood(v):
        enemy_count+=(phi(w)-phi(v))
if abs(enemy_count/4)>random.random():
    if phi(v)==-1:
        phi(v)+=1
    elif phi(v)==1:
```

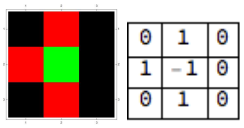

Figure A.1: ϕ and color representations of a sample neighborhood in a discrete IBM. Here $enemyCount = \nabla^2\phi(v) + 4\phi(v) = \sum \phi(w) - \phi(v) + (4 \times -1) = 7 + -4 = 3$

```
        phi(v)-=1
    else:
        phi(v)=round(enemy_count/4)
```

Here empty sites are filled in by a slightly different rule, but the behavior of this simulation is qualitatively unchanged. It may seem that the value of $enemyCount$ is different for this algorithm as for the original LIBM but in fact the computations are equivalent. For example, figure A.1 shows a sample neighborhood portrayed in both the original color representation of the LIBM as well as the scalar order parameter representation introduced above. In both cases, $enemyCount = 3$

Noting that the for loop represents a sum over the 4 sites $w \in neighborhood(v)$ i.e. $w : d(w, v) = 1$, we can write:

$$|enemyCount| = \begin{cases} -\Big\{ \sum\limits_{w:d(v,w)=1} \phi(w) - \phi(v) \Big\} - 4\phi(v), & \phi(v) > 0 \\ \Big\{ \sum\limits_{w:d(v,w)=1} \phi(w) - \phi(v) \Big\} + 4\phi(v), & \phi(v) < 0 \end{cases} \tag{A.1}$$

Which, upon comparison with equation (1), reveals that $|enemyCount| = |\nabla^2\phi(v) + 4\phi(v)|$

The change in the status of a given lattice site at a given time will be reflected by a change in the value of ϕ. In the given algorithm this will depend on whether the value of $enemyCount$ is large enough compared to a random number we'll call r . The probability of death or survival is $P_{survive} = P(\Delta\phi = 0) = P(\frac{|enemyCount|}{4} \leq r)$ and $P_{death} = P(\Delta\phi \neq 0) = P(\frac{enemyCount}{4} > r)$. The expectation value, for the change in the order

parameter over time, in general, is:

$$\langle \Delta\phi(v) \rangle = \sum \Delta\phi(v) \cdot P(\Delta\phi(v))$$

$$\langle \Delta\phi(v) \rangle = 0 \times P(\Delta\phi = 0) + 1 \times P(\Delta\phi = 1) - 1 \times P(\Delta\phi = -1)$$

Then the expected value of the change in ϕ, for the case of both positive and negative order parameter, according to the update rules above, is given as:

$$\langle \Delta\phi(v) \rangle = P(\frac{1}{4}\nabla^2\phi(v) + \phi(v) > r)$$

$$\text{with, } P(\frac{1}{4}\nabla^2\phi(v) + \phi(v) > r) = \int_0^{\frac{1}{4}\nabla^2\phi(v)+\phi(v)} p(r)dr$$

If we assume r is drawn from a uniform random distribution $r \in [0, 1]$ (other probability distributions will affect the outcome) then:

$$\langle \Delta\phi(v) \rangle = \frac{1}{4}\nabla^2\phi(v) + \phi(v) \tag{A.2}$$

The final step is to assume that the behavior of $\langle \Delta\phi(v) \rangle$ will equal $\Delta\phi(v)$ in the limit of fine time-slicing compared to spatial size. Letting time and space be continuous:

$$\frac{\partial\phi(x, y, t)}{\partial t} = D\nabla^2\phi(x, y, t) + \phi(x, y, t) \tag{A.3}$$

This is simply the reaction-diffusion system commonly used to describe pattern formation in bacterial communities and other systems [224].

Figure A.2 shows the demixing behavior of the continuous field model, and the LIBM.

This result is also consistent with the Allen-Cahn equation with a free energy density of $f(\phi) = -\phi^2$, or even $f(\phi) = -\frac{1}{4}\phi^4 + \frac{1}{2}\phi^2$. One potential for future work is to investigate how hard the analogy to free energy density can be pushed. For example, there are two

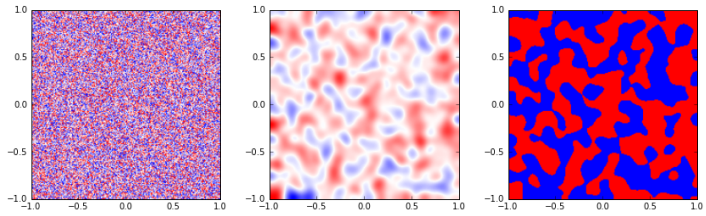

Figure A.2: The phase separation behavior of the continuous field model. Left: well mixed initial seeding on the continuous domain (-1:1,-1:1). Blue corresponds to $\phi = -1$, red to $\phi = 1$ and white to $\phi = 0$. Middle: system after evolving for several thousand time slices. Right: binarized version of middle image with each pixel forced to "choose" to be either blue or red.

minima at equal values of $f(\phi)$, implying that the chemical potential of each phase is equivalent, which means that there should be zero Laplace pressure between phases. This will be reflected as strain-strain interfaces that minimize their surface areas— an observation that could be experimentally verified.

A.1.3 Viscoelastic biofilm simulations

To capture the viscoelastic character of the biofilm, we model it as a chain of cells coupled by Voigt-Kelvin elements, with spring stiffness E and dashpot damping η. Reproduction and death are assumed to be Poisson processes with an activity rate λ_{act}; the time-step between events is chosen from an exponential distribution $dt \sim e^{-\lambda_{act} t}$. Each event corresponds, with equal probability, to the step-strain resultant from reproduction or death of a cell at a random position in the biofilm, and as such imposes a step stress σ_0 felt instantaneously throughout the biofilm. Finally, after each event the velocities and positions of all the cells are updated according to the current state of stress in the biofilm and the constitutive equations $\sigma(t) = E\epsilon(t) + \eta \frac{d}{dt}\epsilon(t)$, using backward-Euler integration. This leads to the discretization scheme:

$$\epsilon_t = \frac{1}{1 + dt\frac{E}{\eta}} \cdot (\epsilon_{t-1} + \frac{dt}{\eta}\sigma_t))$$

A.2 Model system: *V. cholerae* and the type VI secretion system (T6SS)

To address the aims presented above, the Hammer lab has provided engineered strains of *V. cholerae* that not only form biofilms with tuneable amounts of EPS but also come equipped with the type VI secretion system (T6SS). the T6SS is a machinery that is used to transfer toxic effector proteins from one cell to another in a contact dependent fashion, and is present in 25% of all sequenced gram negative bacteria [225]. Its prevalence can be explained by its positive impact on bacterial fitness in social environments. One way in which this shows itself is through cheater avoidance, which is achieved through T6SS generated clonal phase separation. [28] T6SS also helps bacteria adhere to host cells, regulate intracellular pH, and enhance genetic diversity by allowing cells to "pick up" enemy DNA [226].

T6SS also appears to be important to the health of microbial communities. There are reports of the importance of T6SS in biofilm formation [227]. It is a highly modular system with potentially many different effector-immunity pairs each strictly and independently regulated on a single genome. T6SS is switched on and off according to a number of cues and signals such as the presence of chitin, temperature, quorum sensing, pH, salinity, Iron concentration, and antibiotics [228].

For our purposes, T6SS affords a unique tool to vary the amount of activity due to cell lysis and reproduction in biofilms in the homeostatic limit. We've used several strains in the work discussed below. First of all, there are isogenic mutual killer strains of V. cholerae (SN306 and SN316) which differ only in the toxic effector used to kill the other strain. T6SS can also be "turned off", as in genetically modified nonkiller strains (SN311 and SN318) which cannot kill but are otherwise identical to our mutual killers [229, 230]. All four strains can be genetically modified to produce no Vibrio Polysaccharide extracellular matrix components (VPS-) [35], or to produce normal amounts of VPS (VPS+). The strains used are also engineered to express either the Kusabira Orange (mKO) orange fluo-

rescent protein (SN306 and SN311) or the teal fluorescent protein (SN316 and SN318) for microscopy. Strains other than this will be introduced inline.

APPENDIX B

TRAFFIC

Percolation for different vehicle types

In chapter 3, we principally considered percolation for vehicles of size 7 m ($s = 14$ m), which is a typical size representative of cars. However, many vehicles on the road are longer. For example, the typical size of trucks is about twice as long, and with this larger size, the percolation probability similarly increases. Thus, we reran our microscopic IDM/MOBIL simulations and compared these results to the theoretical prediction of Eq. (1) for a variety of different road parameters (Fig. B.1). For 2, 3, and 4-lane roads with "cars," ρ_H at the critical percolation point ($P(\Phi = 0) = 0.5$) are $5, 10,$ and 13 respectively. For 2, 3, and 4-lane roads, percolation density for "trucks" corresponds to $3, 6,$ and 8 respectively. In general, at the point of percolation, "trucks" of twice the size as "cars" show a decrease in the critical percolation density ρ_H by $\approx \frac{2}{3}$.

Independence of percolation on highway/urban speeds

Our percolation-based interpretation and analysis is independent of numerous details contained in any microscopic description in vehicle traffic. The essential quantity that arises as being highly significant, however, is the minimum allowed center-to-center separation between vehicles, s. To verify that our understanding of the results holds, we varied the preferred speeds in the IDM/MOBIL simulation to test both highway and urban conditions. (Fig. B.2). Indeed, we observe the percolation probabilities measured from these different scenarios are closely matched, and accurately follow the theoretical percolation prediction.

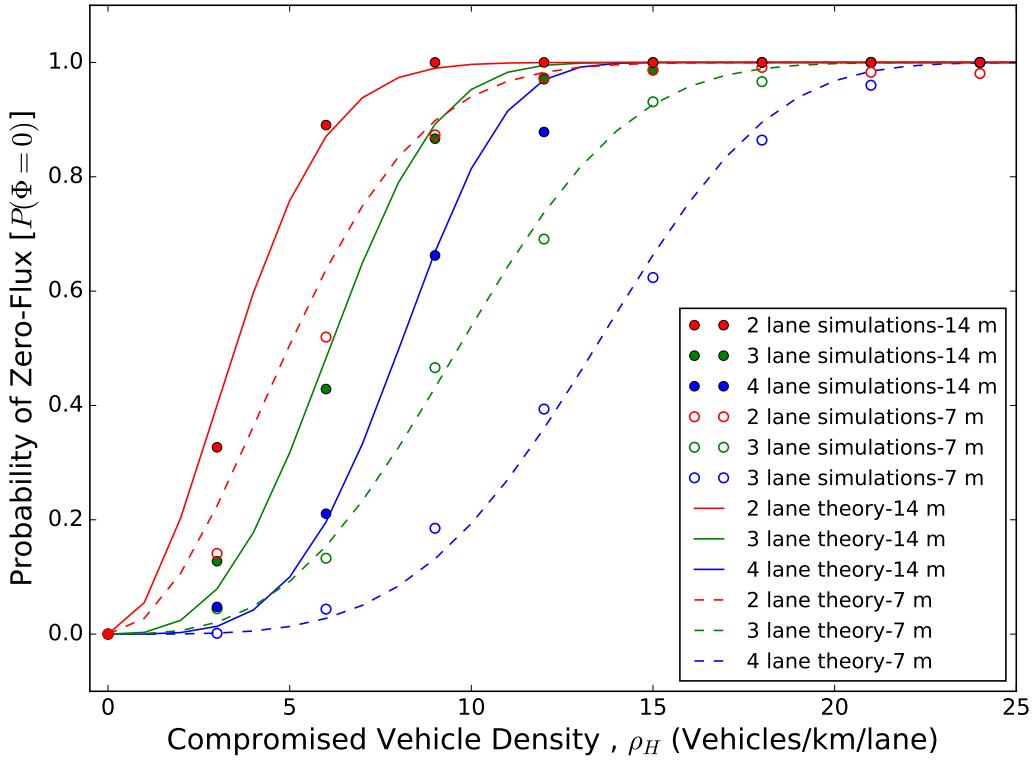

Figure B.1: Percolation predictions (lines) compared to microscopic simulations (circles) for vehicles of different sizes and number of lanes. Solid lines and filled circles are data for "trucks" with size 14 m. Dashed lines and open circles are data for "cars" with size 7 m. Colors denote different number of lanes.

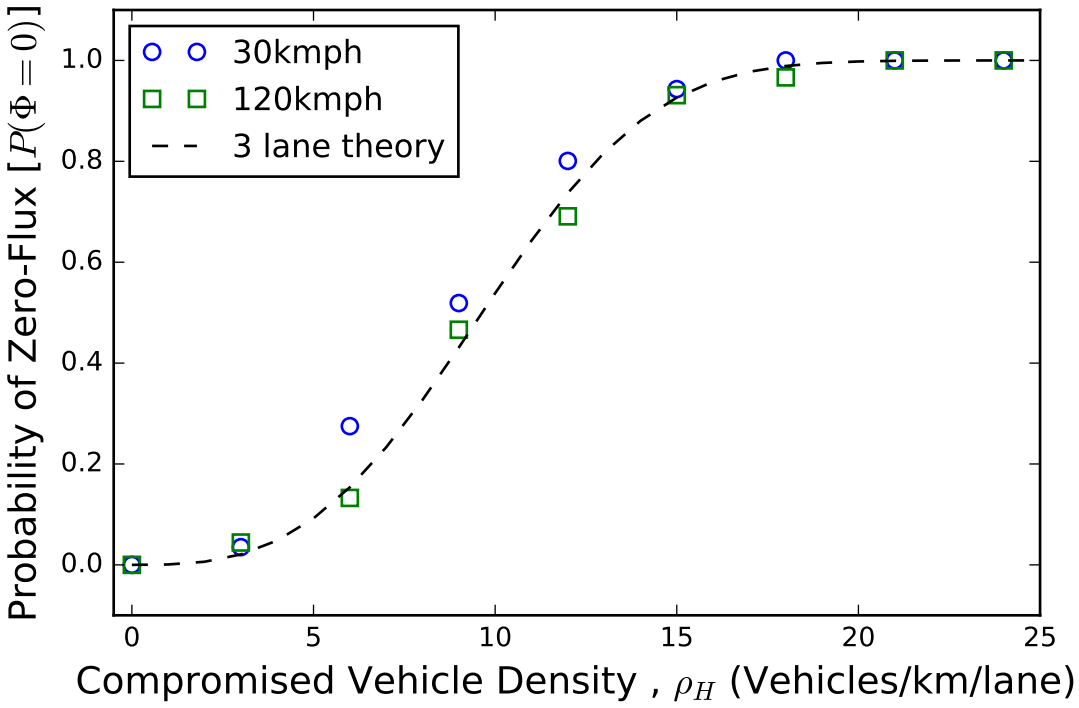

Figure B.2: Independence of percolation probabilities from the preferred speed parameter in the IDM/MOBIL microscopic model. Dashed lines are theoretical percolation curves for vehicles with size 7 m. Blue circles denote IDM/MOBIL simulations where maximum speed is 30 km/h, representative of urban scenarios. Green squares denote IDM/MOBIL simulations where maximum speed is 120 km/h, representative of highway scenarios.

Percolation prediction and empirical traffic configurations

While deriving our analytical percolation model, we approximated vehicles as having a particular size, and uniform probability to be found anywhere on a simulated highway-like environment. A valid question is whether these approximations are sufficient to describe real traffic, where vehicles might self-organize in a manner that affects the percolation probability. To address this question, we measured percolation probabilities corresponding to real-world vehicle driving patterns from the NGSIM traffic dataset [142].

The NGSIM dataset contains information regarding vehicle size, lane number, and position on the highway at different times. In order to emulate a large-scale hacking event in which multiple vehicles were suddenly and simultaneously disabled on a 3-lane highway, we selected a subset of 3 adjacent lanes from the NGSIM dataset at a particular timestamp in a 500 m stretch of highway. Corresponding to that timestamp, we randomly selected a certain number of vehicles as compromised, and extracted their positions from the NGSIM dataset. We then checked for blockages, which we defined as configurations where the space between the compromised vehicles on adjacent lanes is smaller than the typical vehicle length. This definition is consistent with our IDM/MOBIL simulations because the spacing between vehicles is too small for non-compromised vehicles to pass through. By looking at multiple configurations from different time stamps, we obtained the probability of percolation for various densities of compromised vehicles/km/lane, ρ_H. Our analytical formula captures the trend of percolation probability versus ρ_H as measured from the NGSIM data, remarkably well, with $R^2 > 0.99$ (Fig. B.3). Thus, this data suggests the potential differences between self-organized flow of simulated vehicles using IDM/MOBIL and the self-organized flow of real-world traffic do not affect our percolation interpretation of post-hack conditions.

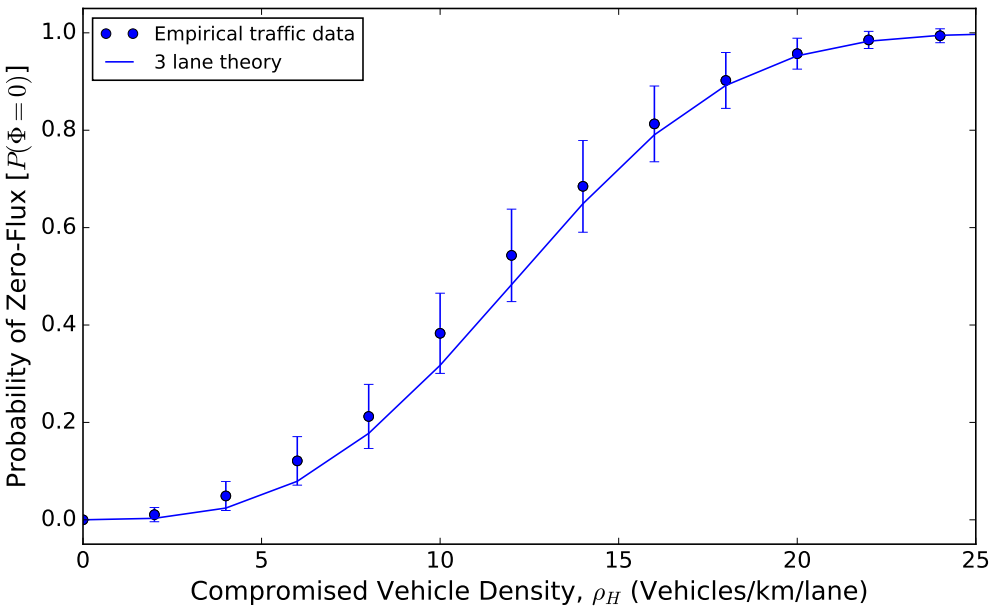

Figure B.3: Percolation probabilities for empirical distribution of vehicles available in the US DOT NGSIM dataset. Solid lines are theoretical prediction for vehicles of spacing 7 m. Symbols represent percolation probabilities corresponding to actual vehicle positions in traffic for a 500 m stretch of highway.

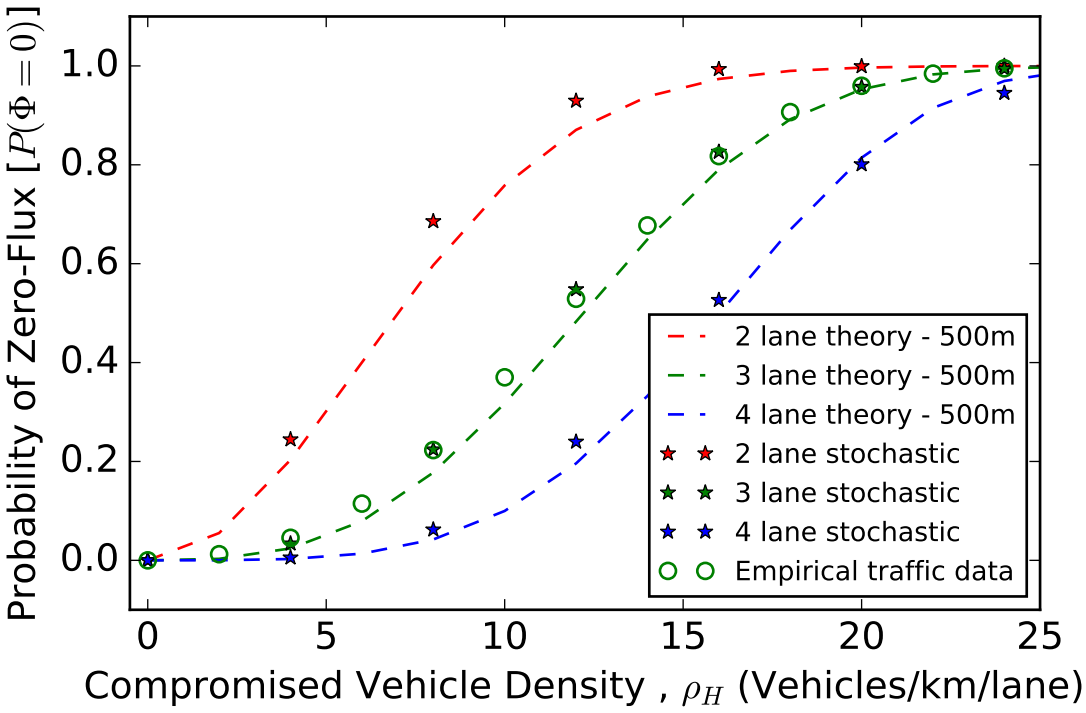

Figure B.4: Theoretical percolation predictions and stochastic vehicle-free model for post-hack traffic disruption have significant agreement. Dashed lines are theoretical percolation curves for cars, with spacing 7 m on a 500m road. Colors denote different number of lanes. Star data points are generated with the stochastic vehicle-free model where strips of a 500 m road are chosen randomly to be inaccessible to traffic. Open circles denote percolation probabilities as measured from empirical traffic (same data as in Fig. B.3) This data reinforces the generality of percolation as an interpretive framework.

Independence of percolation from microscopic traffic simulations

Our analysis of the microscopic IDM/MOBIL simulations for post-hack traffic flow led us to interpret the main results (Figs. 2 and 3) in terms of percolation. As seen in Eq. (1), percolation is broadly insensitive to the vast majority of details in IDM/MOBIL, with the exception of s, the minimum center-to-center distance between two vehicles on adjacent lanes that allows a third vehicle to lane-change between them. Hence, if the percolation interpretation is correct, then our subsequent analysis and predictions using Eq. (1) should be generically reproducible with other parameters or even entirely different models.

To test this reasoning and further validate our results, we develop and ran a vehicle-free stochastic simulation that simply designated randomly selected non-overlapping strips of road to be inaccessible to traffic flow. These strips were chosen to have the same length as vehicles so that we could place them at comparable densities ρ_H to our percolation formula. A given configuration was considered to be percolated when inaccessible strips on adjacent lanes were within 14 m center-to-center of each other. This definition directly reflects the notion that a 7 m vehicle would be unable to navigate through closely packed strips of inaccessible roadway. We find these stochastic simulations (Fig. B.4, points) closely match our theoretical predictions (Fig. B.4, dashed lines), even though no microscopic model for vehicle flow was used. Further, to test this is valid for real traffic, we additionally plot percolation as measured from NGSIM taffic data (Fig. B.3)and find that NGSIM data percolation probabilities are essentially indistinguishable from stochastic simulations and analytic percolation predictions.This evidence strongly supports percolation, and especially Eq. (1), as a broadly-applicable interpretation for large-scale post-hack events including a real-world cyber-physical hack if it should occur.

Generating a street network of Manhattan

OSMnx makes it possible to quickly and systematically generate a street network from map data. OpenStreetMap is a crowd-sourced cartography project. Since its inception in 2004, it has made significant progress in establishing a free editable map of the entire world. OpenStreetMap is to maps as Wikipedia is to encyclopedias [231]. By now OpenStreetMap has extensive and well documented APIs available, which Geoff Beoing made use of in building OSMnx [147]. OSMnx is a free, open-source module for Python that interfaces with OpenStreetMap to download street networks, building footprints, administrative boundaries, and more. OSMnx is built on a stack of NetworkX, a Python package for network analysis and standard graph algorithms, Matplotlib for visualization, and GeoPandas for fast querying of geographical data.

When constructing a primal graph representation of a real street network in which nodes and edges represent intersections and streets respectively, some simplifications and corrections will most likely be required to clean messy map data. For example, a spatial network is planar if it can be drawn in two dimensions with its edges intersecting only at nodes. One of the main difficulties in using satellite imagery to automatically generate street networks is that the real network is usually not planar due to overpasses, bridges, tunnels, and the like. One will need to either rely on the relative rarity of bridges and assume a planar graph or draw more information about the position of overpasses and bridges from another data source (such as OpenStreetMaps Overpass API). Other examples of detailed decisions that must be made to construct street networks include handling artificial nodes that may arise in satellite data at points where roads curve severely, or handling inconsistencies in human generated data, e.g., one report says an overpass is at a specific location but it has since been rebuilt and another report says its somewhere else. Researchers have been working on ways to systematize the generation of urban street networks [232], and OSMnx synthesizes and implements much of that work.

The strength of OSMnx is that it uses an algorithmic method to reproducibly correct and simplify a street network from a constantly maintained and transparent data source. Although of course other studies have investigated the network properties of street networks, before the advent of OSMnx researchers had a much more difficult task in assembling consistent, reproducible, and realistic graphs to represent real cities. OSMnx also enjoys the significant advantage of dealing with the primal street network, in which nodes are intersections and streets are edges as, as opposed to other tools which use the dual street network in which intersections are treated as edges and roads are treated as nodes. This means that OSMnx retains the spatial and metric information needed for our study such as road length and width.

To construct our street network of Manhattan, OSMnx calls OpenStreetMaps Nominatum API and builds a polygon from the boundary geometry that gets returned for the query `Manhattan`. It then uses OpenStreetMap's Overpass API to fill in the raw street network data inside this polygon. Then OSMnx algorithmically corrects the topology using strict mode, which takes care of dead ends, self loops, and artificial nodes at road elbows. OSMnx returns a directed multigraph that represents Manahattan, where the edges contain plentiful information such as the latitude/longitude, street name, number of lanes, street length, speed limit, etc. We then cast the manhattan city network as an undirected graph. While all subsequent analysis was performed on the undirected version of the Manhattan network, we performed some analysis also on the full directed multigraph as well with similar results, discussed further below.

There are about 10,000 edges in the graph of Manhattan and about 2,000 of them contain information about the number of lanes on the road they represent. The edges also contain partially complete information on the other features such as "speed limit" and "highway type." To use our percolation formula to predict risk from hacking we need to know how many lanes each road has, so we used the 2,000 labeled edges as a training set and performed a random forest regression to infer the number of lanes on the 8,000 unlabeled

edges. A random forest regression is an ensemble method within (usually) supervised machine learning that aggregates a number of decision tree learners, each of which has been trained on a random subset of the features, and averages their outputs. This method was chosen as it outperformed other ensemble methods and linear regression in accuracy as measured by R^2 score of model predictions versus hold-out data. Introductions to classification and regression by random forests are readily available [233].

For the complete data cleaning and modeling parameters and process please see the supplemental ipython notebook at:
https://github.com/dyanni3/Traffic-Simulations/blob/master/OSM%20manhattan.ipynb. In short, we dropped irrelevant features like 'osm ID' and filled in null values on incomplete data. We used Scikit learn's RandomForestRegressor to construct a bootstrap sampled model with 10 estimators, no max depth, and an evaluation criterion of mean squared error. We achieved over 85% accuracy as measured by R^2 and a Pearson's R score of 0.88 (Fig. B.5, demonstration of substantial accuracy enabled by our machine learning model).

B.1 Analysis of hacking on the street network

B.1.1 A primer on connected component labeling

There are several types of graph in graph theory. Undirected graphs are just a collection of nodes and edges, and in the simplest case edges are just like line segments, each one connecting two nodes. In an undirected graph it is possible for edges to have different "weights," a scalar value associated with the edge that conveys additional information. For example, in our street network graph the edges could be weighted by length, or by number of lanes, or by probability of percolation. Directed graphs, or Digraphs, are graphs in which the edges are like vectors, they can have attributes associated with them and they each have a direction, so they have a starting node and an ending node. It is common for a pair of nodes to have two directed edges running between them: one from node A to node B and another from node B to node A. This could, for example, represent a two way

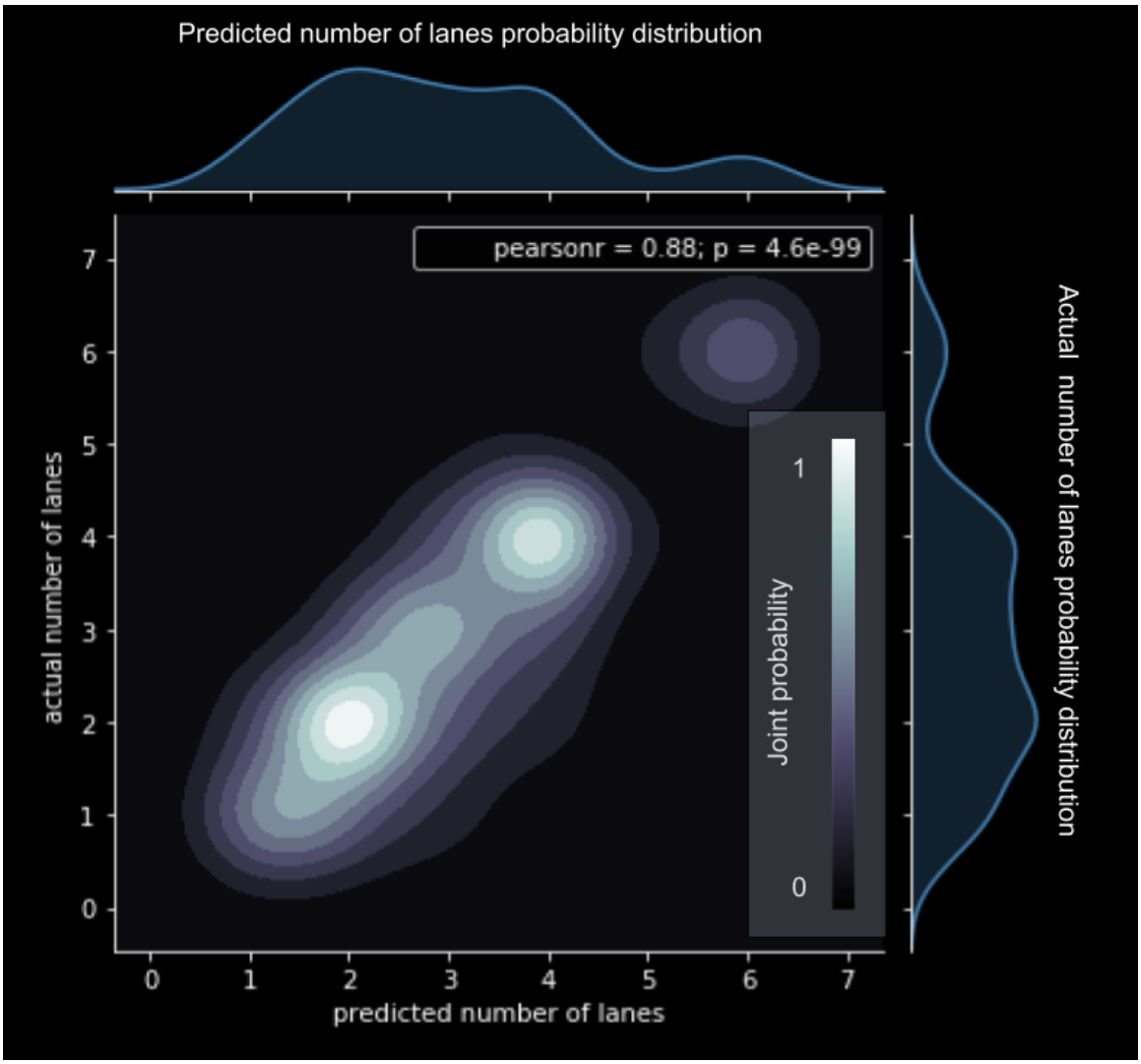

Figure B.5: Joint density plot showing the joint distribution of predicted number of lanes and actual number of lanes in the test-set. The colormap in the joint-plot ranges from probability density of zero (black), to probability density of 1 (white). Top: distribution of predicted lanes. Right: distribution of actual lanes. From the single variable distributions shown on the top and the right, it is clear that our model retains the "shape" of the real distribution, and doesn't introduce any systematic bias in the number of lanes on roads in Manhattan. From the slope of the bright areas in the joint plot and the high Pearson's R score it is clear that our model is reasonably accurate at predicting the actual number of lanes on a highway in Manhattan given some auxiliary information such as the speed limit, length, and "highway type," all of which data is more complete in the OSM dataset than number of lanes.

street in Manhattan. It is also possible for an edge to start at one node and end at the same node, forming a self-loop. Finally, if there are multiple "degenerate" edges going from the same starting node to the same ending node then you have a multigraph. Normally you would only have either 0 or 1 edges connecting a pair of nodes, or maybe two in the case of directed graphs, but in multigraphs you could have any natural number of edges connecting a single pair of nodes. The fully general case of directed multigraphs are sometimes called *multidigraphs*.

OSMnx gives us a full scale multidigraph representation of the streets in Manhattan. This means that one way streets are represented as directed edges. A common question to ask about a given network is how many separate connected subgraphs exist within it. By connected we mean a collection of nodes that can each be accessed by any other in the connected network by a path consisting of a series of edges and nodes also contained in the connected network. But this definition is ambiguous when it comes to dealing with undirected versus directed graphs. For example, imagine a physical manifestation of an undirected network made out of beads and yarn sitting on a table, then for a connected graph if you pick up one of the beads you'd lift up the entire graph. For an unconnected graph if you pick up one of the beads then part of the graph would still be left sitting on the table. This sense of connectivity is captured by algorithms that measure simply connected components on undirected graphs. However, for a directed graphs this is insufficient. Imagine a graph that is only two nodes, A and B, and a single directed edge going from A to B. This graph appears to have one *simply connected component*, but it has two *strongly connected components*. That is because if you start at node B you cannot access node A, so the node B represents one of the strongly connected components and the node A represents the other one.

For our Manhattan networks we measured both (i) the number of strongly connected components on the full multidigraph, and (ii) the number of simply connected components on the Manhattan network after being cast as an undirected graph after a simulated hacking

event that removes some portion of edges. We found the results are within error bars of one another. Therefore the rest of the analysis was performed on undirected versions of the Manhattan graph.

B.1.2 Connected components analysis

Equipped with a fully informed Manhattan street network, we used our analytical formula for compromised vehicle percolation to predict the probability of percolation on every road in Manhattan, given a certain compromised vehicle density. We assume for our analysis that there is a uniform *density* of traffic on every road in Manhattan. While this assumption clearly does not hold in real traffic, this simplification is justified because (i) we later sweep through all densities on the city network so that the entire parameter space is explored for each road, and (ii) real roads experience a relatively narrow dynamic range of traffic densities [117]. After distributing compromised vehicles evenly throughout the city network, we calculate the probability of road percolation on each road. We then remove edges from the network stochastically, weighted by the road percolation probability, as follows: for each edge in the network we pick a random number r and if $r < P_p$ the edge gets pruned. After the edge pruning we are left with a partial network and we use NetworkX's standard connected components analysis (which uses a simple depth-first search approach) to compute the number of connected components. We repeat this process many times to generate the data shown in the main text (Fig. 3a and b). When using the full multidigraph version of our network in this analysis, we find that the size of the largest and second largest "Strongly Connected Components" fall consistently within error bars of the largest and second largest connected components of the undirected graph.

To further visualize how a hack can break the city network into smaller and smaller unconnected subgraphs, we generated a visualization of the edges in the post-hack network colorized according to which component they belong to (Fig. B.6). As the density of compromised vehicles increases, a greater number of small subgraphs get "chipped off"

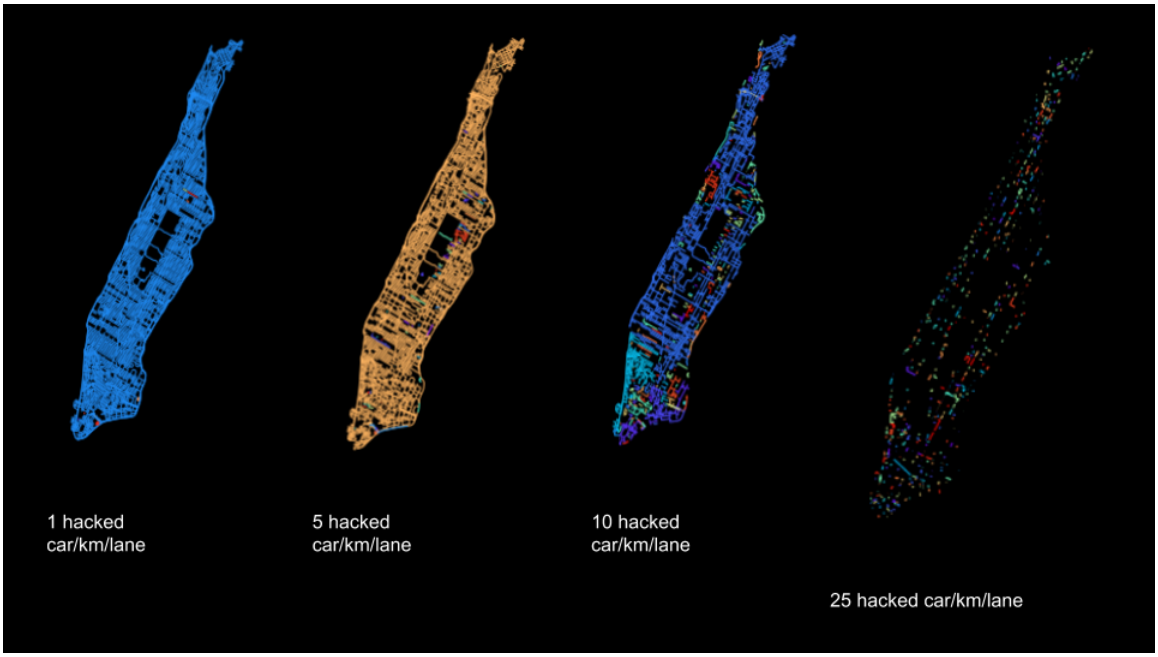

Figure B.6: Random coloration of each connected component after a hack of $\rho_H = 1$ (left), $\rho_H = 5$ (second from left), $\rho_H = 10$ (third from left) and finally $\rho_H = 25$ (right). Edges that have been pruned correspond to roads that have become obstructed due to a percolation of compromised vehicles, and are colored black.

of the largest connected component. At a compromised vehicle density approaching the critical value for city fragmentation of ≈ 13 the largest connected component begins to break into roughly equal sized pieces. At a very large compromised vehicle density not only are there very few remaining edges, but they are mostly disconnected from each other. An cyber-physical hacking attack of this magnitude would be catastrophic.

The three regimes of mild to severe traffic load and fraction of compromised vehicles regimes discussed in the main text can be summarized based on their average probability of road blockage, q, which is averaged across all the road probabilities in Manhattan for a given ρ_H. The three regimes are $q <\approx 0.25$, $q <\approx 0.45$, and $q \geq\approx 0.45$ (Fig. B.7a). When $q \approx 0.25$ we see the onset of dramatically reduced traffic flux. When $q \approx 0.45$ we see city fragmentation.

B.1.3 Google Places API

To cast the effects of city fragmentation into concrete terms of real safety risks, we investigated how a hack would affect access to emergency services. To find the locations of services in the city we used a Python wrapper for the Google Places API developed by Samuel Adu and others [234]. The Google Places API is a service that returns information about places using HTTP requests. This can be thought of as being exactly the same as when you search for something in Google Maps, except that the query returns much more information, including latitude and longitude data for the search results. After geolocations for services such as fire stations and hospitals are returned by Python-Google-Places, we use OSMnx which calls GeoPandas to find the nearest node in our Manhattan graph to a given service latitude/longitude pair. This amounts to running a k-nearest-neighbors algorithm with $k = 1$ and using a geodesic distance metric. When the nearest node is found, the service is assigned to that node. After a hack, for each service, we inquire which connected component its node belongs to and then determine what percentage of nodes in the entire network also lie in the same connected component. This is computed in a brute force method, for each service location.

One could ask whether the drastic reduction in emergency services (Fig. 3c) is due to some property of the way these services are distributed in Manhattan. To test this hypothesis, we constructed samples of "nodes of interest" uniformly at random and tested how many nodes have access to those randomly chosen nodes of interest. When using a random sample containing 0.5% of the nodes in Manhattan (roughly the same frequency as each of the emergency services tested) we find that access to these nodes is nearly identical to access to emergency services (Fig. B.8). This result suggests that the reduction in access to emergency services is not due to some specific fragility of Manhattan, such as would be the case if all emergency services were clustered right next to each other, but rather it is a generic feature of city fragmentation that we'd expect to see in any urban street network analysis.

B.2 Vehicle brand prevalence and hacking risks

Vehicles from the same manufacturer typically utilize similar Internet-connected systems. Thus, it is possible that nearly all Internet-connected vehicles from one particular manufacturer are hacked through the same vulnerability. To understand these risks, we analyzed vehicle brand registration distributions across New York State. We assumed that at a particular road density, the fraction of the vehicles on road is reflected by the fraction of registered vehicles belonging to that brand. Honda, Toyota, Ford, Chevrolet, and Nissan represent 5 of the top manufacturers, collectively representing $> 40\%$ of all registered vehicles (Fig. B.9), and the largest brand, Honda, represents $> 10\%$ of all registered vehicles. If all Hondas were hacked during rush hour in Manhattan ($\rho = 250,000$, density of Hondas on the road $\approx 25,000$), there is an $\sim 40\%$ chance of city-wide fragmentation.

B.3 Simulations of post-hack dynamics

The percolation of blocked roads due to hacked vehicles is a worst-case scenario, which requires a large number of hacked vehicles; however, compromised vehicle densities below that required for percolation likely dramatically impact dynamics, slowing the speed of traffic. Cascading effects of blocked roads on neighboring roads could further reduce traffic flows. One might therefore expect the impact of traffic slowdowns would be a function of the amount of time passed after a large-scale hacking event, i.e., the longer vehicles are stuck on the road, the slower traffic flows.

To investigate the dynamic effects of compromised vehicles on a Manhattan-like road network, we performed traffic simulations on a 5×5 grid using the Simulation of Urban Mobility (SUMO) traffic simulation suite. In these simulations, each road has 3 lanes, is 200 m long, and allows for two-way traffic flow. Each vehicle has a predefined route, with random routing, random starting, and random ending positions. Every second, a new vehicle is introduced, and once the vehicle reaches its destination, it is removed. All inter-

sections have traffic lights, to prevent vehicles from blocking intersections. Compromised vehicles are stopped at random positions. Vehicles that cannot reach their destinations remain in the simulation, increasing the total vehicle density; this is similar to increased density on real roads in the event of blocked lanes or traffic jams.

The average velocity of vehicles across the grid V_0 is fairly constant at ≈ 7 m/s under normal pre-hack conditions. However, when vehicles are compromised, the average post-hack speed $V_H(t)$ reduces with increasing compromised vehicle density, ρ_H (Fig. B.10). We find that V_H depends on the amount of time t after a hack, where $t = 0$ corresponds to the moment when vehicles are disabled. We find that when $t = 1,000$ s, $V_H(t) = V_0/2$ at $\rho_H \approx 3$ vehicles/km/lane, but 5,000 s after compromise, $V_H(t) = V_0/2$ at $\rho_H \approx 1$ vehicle/km/lane.

We observe that above $\rho_H \approx 15$ vehicles/km/lane, V_H is almost zero for all t. This density corresponds to the density at which grid fragmentation occurs, as determined from geometric percolation (Fig. B.11). Thus, while dynamic effects are important, the underlying percolation threshold ultimately determines when there is complete gridlock. This geometric calculation allows worst-case scenarios to be assessed without expending the significant computational effort involved in citywide traffic simulations.

In this simulation, vehicles follow a fixed route, and so the estimate of dynamics does not account for traffic rerouting, which could be reasonably expected in real-world contexts. In the future, it will be useful to consider traffic rerouting alongside other important factors that might arise in response to a large-scale hacking event, such as a reduction in the number of disabled vehicles due to emergency response efforts. These effects would be particularly helpful in trying to develop an optimal recovery plan.

B.4 Analysis of local traffic disturbance from Macy's Thanksgiving Day Parade, 2016

In general, predicting the overall impact of a planned or unplanned non-recurrent traffic disruption due to lane closures is a well studied but difficult problem. Recent progress has benefitted from the increasing availability of public traffic incident data and from the use of machine-learning techniques [235, 236, 237]. In principle, it should be possible to combine our findings with the techniques outlined in those studies to analyze the full impact of a large scale hack. However, a full-scale survey of the impacts of traffic disruptions due to non-recurring traffic incidents such as planned special events is beyond the scope of this study. Furthermore, it would be difficult to validate such an investigation without comparison to real world data. Fortunately, no such data currently exists for catastrophic city fragmentation type events.

However, we *do* obtain a "zero$^{\text{th}}$ order" sense of a realistic response to multiple simultaneous road blockages by examining traffic stream data from the NYC DOT [238] during the month of November, 2016. In particular, we are interested in the effects of lane closures due to the *Macy's Thanksgiving Day Parade, 2016*. We quantified average traffic speeds within one block of the parade route during the time period from 12:00 pm to 8:00 pm for each day in November (Fig. B.12). On the day of the parade, the average velocity within one block of the parade route is two standard deviations lower than the average velocity at those same locations on other days in the same month. Further, the average traffic speed over all of Manhattan on Thanksgiving day is one standard deviation *higher* than average (Fig. B.13). This gives a rough idea of how dynamics are affected by blocked roads, when such blockages are planned, and vehicles knowingly reroute, which is the best case scenario. In contrast, our simulations of dynamics on a grid are the worst case scenario, when traffic is not rerouted. Furthermore, as a control, we show that traffic on Thanksgiving day in Manhattan is not, on the whole, disrupted (Fig. B.13).

B.5 A primer on malicious hacking

A number of high-profile events illustrate the various ways hacking can be weaponized. A selection of recent examples include: (i) distributed denial-of-service with zombie botnets, (ii) large-scale social engineering and disinformation campaigns using stolen credentials, (iii) remote deactivation of electricity grids[239], (iv) industrial sabotage[240, 241], (v) theft of money, identity, and intellectual property, (vi) disrupted access to medical facilities[242], (vii) disclosure of personal information as a means of coercion, and (viii) large-scale covert cyber-spying. Individually, these malicious hacks demonstrate the harm a few individuals can inflict with the right software exploits. Collectively, they form a broader picture of the social challenges presented by technology. To further illustrate, we summarize some of the more common yet lower-profile forms of hacking prevalent today.

1. Digital eavesdropping can be easily achieved with packet sniffers such as Wireshark or its equivalents. These software tools can be used defensively to analyze and record suspicious network traffic, however, they can also be used to discretely monitor the activity of others without their consent.

2. Keyloggers are a class of software that monitors user input through the mouse and keyboard. Generally, the purpose is to discretely record sensitive information such as passwords.

3. Denial of Service (DoS) and Distributed Denial of Service (DDoS) attacks flood targeted servers in order to overload bandwidth and computational resources, forcing the target into a non-responsive state. In DDoS attacks, hackers will deploy remotely controlled computers (bots) to increase the number of data packets used in the attack. Interestingly, the damage inflicted by DDoS attacks are mediated through collective effects of multiple bots simultaneously flooding the target. This example shows how collective properties have already been weaponized by malicious hackers.

4. Brute force hacking is a resource-intensive attack typically launched against narrowly chosen targets. It involves the systematic effort to access and decrypt data by trying all combinations of passwords.

5. As an alternative to brute force, man-in-the-middle hacks can use various techniques to insert themselves between a user and the network. From this position, an attacker can force or fool the user to enter sensitive data, passwords, or information of value.

6. Once installed, malware, viruses, and trojan software are routinely used in a variety of ways. Common examples include (i) the covert transmission of information such as data from a keylogger, (ii) theft of intellectual property, and (iii) the installation of software that forces a system to discretely participate in DDoS attacks.

In a relatively short period of time, hacking has gone from an esoteric pastime requiring in-depth expertise to an easily accessible outlet for malicious behavior. Today, there are multiple front-end software packages enabling anyone with basic shell scripting knowledge to perform all of the attacks listed above. Indeed, publicly available software such as Wifiphisher automates the process of de-authenticating a user from a legitimate internet access point, allows the user to connect to an "evil twin" access point that functions as a man-in-the-middle, and ultimately presents the target with a seemingly legitimate request that asks them to enter sensitive information. We provide this information here specifically to argue the case that hacking of autonomous vehicles isn't just a possibility, but for all practical purposes, it is an inevitability. As such, preventive strategies like those discussed in the main text will be essential for the safety of drivers.

B.6 An outlook on hacking autonomous vehicles

Current estimates project approximately 150 million internet-connected vehicles on the road by 2020, with most sharing real-time data through cloud services[243]. A comprehensive knowledge of vehicle localization, local traffic, weather, and infrastructure conditions

would reduce congestion, lead to more efficient commutes, and potentially less accidents among many other possible benefits. However, this increase in connectedness leads to a corresponding increase in vulnerability through mapping, entertainment, and productivity software. As such, the National Highway Traffic Safety Administration lists 15 assessment criteria for significant software updates of vehicles and their related subsystems. The first four criteria are (i) data recording and sharing, (ii) data privacy, (iii) system safety, and (iv) vehicle cybersecurity[244], all of which are likely hacking targets.

A recent string of "white hat hacks" have demonstrated the existence of vulnerabilities in vehicle software through proof-of-concept demonstrations. Chris Valasek and Charley Miller gave one of most well-known examples through a zero-day exploit of the entertainment system in a Jeep Cherokee to seize control of the target vehicle[243]. In response, Fiat Chrysler Automobiles issued a software patch to 1.4 million affected vehicles. In a significantly less-sophisticated demonstration, a low-cost ($\approx \$60$), low-power laser pulse generator was used to stop an autonomous vehicle by creating a "ghost" object in its drive path[245, 246].

Despite these concerning demonstrations, resources are being invested into the development of new software technology such as vehicle-to-vehicle (V2V) and vehicle-to-infrastructure (V2I) communications[247], which allow the sharing of data through wireless networks. These protocols will be essential for autonomous vehicles to maximize fuel efficiency, minimize traffic congestion, and prevent accidents. However, this necessarily means vehicles will be communicating with one another, creating new opportunities for malicious hackers to exploit. Indeed, thought leaders on the subject have expressed due concern. Nevertheless, the U.S. DOT issued a proposed rule in December 2016 that would advance the deployment of connected vehicle technologies throughout the U.S. by mandating the deployment of V2V throughout the light vehicle fleet.

Given the demonstrated hacks exploiting these new connected software systems, there is an urgent need for a better understanding of how collective motion can be weaponized.

As such, the anticipate-and-inoculate approach discussed in the main text will likely continue to progress alongside autonomous vehicle technologies, hopefully in a manner that proactively prevents any large-scale malicious hacks.

B.7 Equations of motion and numerics for SVYY simulations

In the main text we provided a simplified form of the equations of motion where indices for vehicles were excluded. We also combined the equations of motion for human- and autonomously-driven vehicles through the index α, which takes the value A for autonomously-driven vehicles and H for human-driven vehicles. Here, we explicitly write out the full equations of motion with indices and appropriate substitution for the repulsion force coefficient, as described in the main text. Thus, for a simulation with N_H human-driven vehicles and N_A autonomously driven vehicles, we have

$$\begin{aligned} \ddot{x}_i &= F_i^{\text{propulsion}} + F_i^{\text{repulsion}}, \\ F_i^{\text{propulsion}} &= \tau_\alpha^{-1}(v_{\alpha,i} - \dot{x}_i), \\ F_i^{\text{repulsion}} &= \begin{cases} \left(\frac{v_{\alpha,i}}{\tau_\alpha}\right)\left[\frac{(1-\delta x_{i,i+1}/R)^{3/2}}{(1-r/R)^{-3/2}}\right], & \delta x_{i,i+1} < R \\ 0, & \text{otherwise}, \end{cases} \end{aligned} \tag{B.1}$$

where the index $i = 1 \ldots N$ runs over all $N = N_A + N_H$ vehicles, the distance $\delta x_{i,i+1} = x_{i+1} - x_i$ is the separation between two consecutive cars within a lane, and the preferred speed $v_{\alpha,i}$ is drawn from a Gaussian distribution for the N_H human-driven vehicles whereas autonomous vehicles are all assigned a single uniform value. Simulations were performed on straight "roads" of length L with periodic boundary conditions. When a vehicle's position at time step t was calculated to $x_i(t) = L + \delta L > L$, its position was stored as $x_i(t) = \delta L$. As a result, the calculation of $\delta x_{i,i+1} = x(t)_{i+1} - x(t)_i$ takes into consideration the possibility that for vehicle i, the next vehicle $(i+1)$ could be wrapped around back to

Table B.1: Empirical values for density, velocity, and flux. The sources are: (1) Northbound 101 at Cabrillo Blvd., California, (2) Northbound 101 at 1st St., California, (3) Southbound I85 exit 249C, GA, and (4) Southbound 101, Hollywood Freeway, California (DOT NGSIM dataset). Rows where the source is starred (*) are used to generate the response time τ_H in Fig. 4.3. All entries are used in empirical measurements of $\Phi(\rho)$ in Fig. 4.4

	ρ (cars/km/lane)	v (km/h)	Φ (cars/h/lane)
source	median	median	median
1	13	76	1,004
1	16	79	1,292
1	32	37	1,209
1	32	38	1,214
2*	95	6	660
2	5	107	507
3*	127	6	693
4*	37	44	1,623

the origin, and appropriate offsets are incorporated to avoid these edge effects. For human-driven vehicles, the preferred velocities $v_{\alpha,i}$ were redrawn from the Gaussian distribution when they were wrapped around to the origin in order to keep faster vehicles from simply catching-up with the slowest vehicle and equilibrating into a single long chain of vehicles. All simulations were performed in Python with a time step Δt such that $\Delta t = (1/20)$ s, and a total of 10,000 time steps (500 s) were computed.

B.8 Quantitative image analysis

Daytime traffic videos in California (CA) were obtained from live traffic camera streams available on the Caltrans website[98]. Nighttime traffic video from Atlanta, Georgia (GA) was recorded manually from a conveniently located building near the highway off ramp using a Canon EOS Rebel DSLR. Videos were analyzed using the OpenCV computer vision library and features of interest were detected through the Harris corner detection algorithm[248]. Features were chosen and spatial averaging performed such that individual cars could be automatically localized and tracked within each video using the Lucas-Kanade[249] algorithm. Distances between lane markers were used to scale and correct

for perspective distortions of the camera. Specifically, federal highway guidelines specify the use of 10 ft white markers with 40 ft spacing (center-to-center distance), though most drivers grossly underestimate this distance[250].

Empirical measurements [Fig. 4.4] of the median and interquartile range for density ρ, velocity v, and flux Φ are provided here for reference [Table B.1].

B.9 Calculation of human driver response time

While the DOT data provided vehicle coordinates $x(t)$, we used quantitative image analysis on the first two video sources to obtain this information. Differentiating and smoothing with a Savitzky-Golay filter allowed us to identify vehicles that stopped and accelerated over a time $t_f \approx 2 - 5$ s due to stop-and-go traffic. To empirically determine the human-driver response time τ_H, we assume that a driver in stopped traffic will accelerate when a sufficiently large gap between them and the next car becomes available. The timescale during which the car adjusts its velocity then corresponds to the response timescale τ_H.

From this perspective, we define the moment a vehicle at rests starts moving as $t = t_0$. From our image analysis and DOT data, we found that within a few seconds, most cars initially accelerate, but then experience a plateau in velocity. At lower densities, this time to plateau is about 2 s, while for higher densities, it is about 5 s. Defining this zero-to-plateau time interval as t_f, we extract τ_H by fitting measured vehicle position data to $\dot{x}(t - t_0)/\dot{x}(t_f - t_0) = 1 - e^{-t/\tau_H}$ with a non-linear least squares method. In the main text, we simplified this expression by setting $t_0 = 0$ for convenience. In higher-density traffic, we observed drivers tend to accelerate over longer periods of time, whereas in lower-density traffic, drivers tend to react faster. From the empirical California (CA), Georgia (GA), and Department of Transportation (DOT) measurements of the human driver response time τ_H [Fig. 4.3(c)], we calculated average $\tau_H = 2.0$ s, which was used in simulations.

B.10 Validations of active matter model using one-lane traffic flow

Having defined the equations of motion for vehicles on a single lane road, we performed a series of test simulations to confirm the active matter model proposed here (e.g., Eq. 4.3) reproduces basic phenomenology of vehicle traffic. For example, simulating and plotting $x_i(t)$ for $N = N_H = 50$ vehicles immediately reveals the presence of backwards-propagating density waves, otherwise known as "phantom traffic jams," that travel at velocity $\Delta x/\Delta t \approx -2$ m/s [Fig. B.14(a), dense horizontal bands]. Measurements of the time-dependent density $\rho(t)$ [Fig. B.14(b)] and flux $\Phi(t)$ [Fig. B.14(c)] provide further useful quantification of collective motion, as they are influenced by the balance between steady uniform flow and the emergence of phantom traffic jams.

For comparison, we analyzed videos of single-lane traffic flow to generate the equivalent empirical observations. We observed similar density waves with propagation speeds ≈ -3 to -6 m/s, with qualitatively similar fluctuations in $\rho(t)$ and $\Phi(t)$ [Fig. B.15]. In the main text, we provide a more rigorous quantitative comparison between this empirical and simulation data [Fig. 4.4].

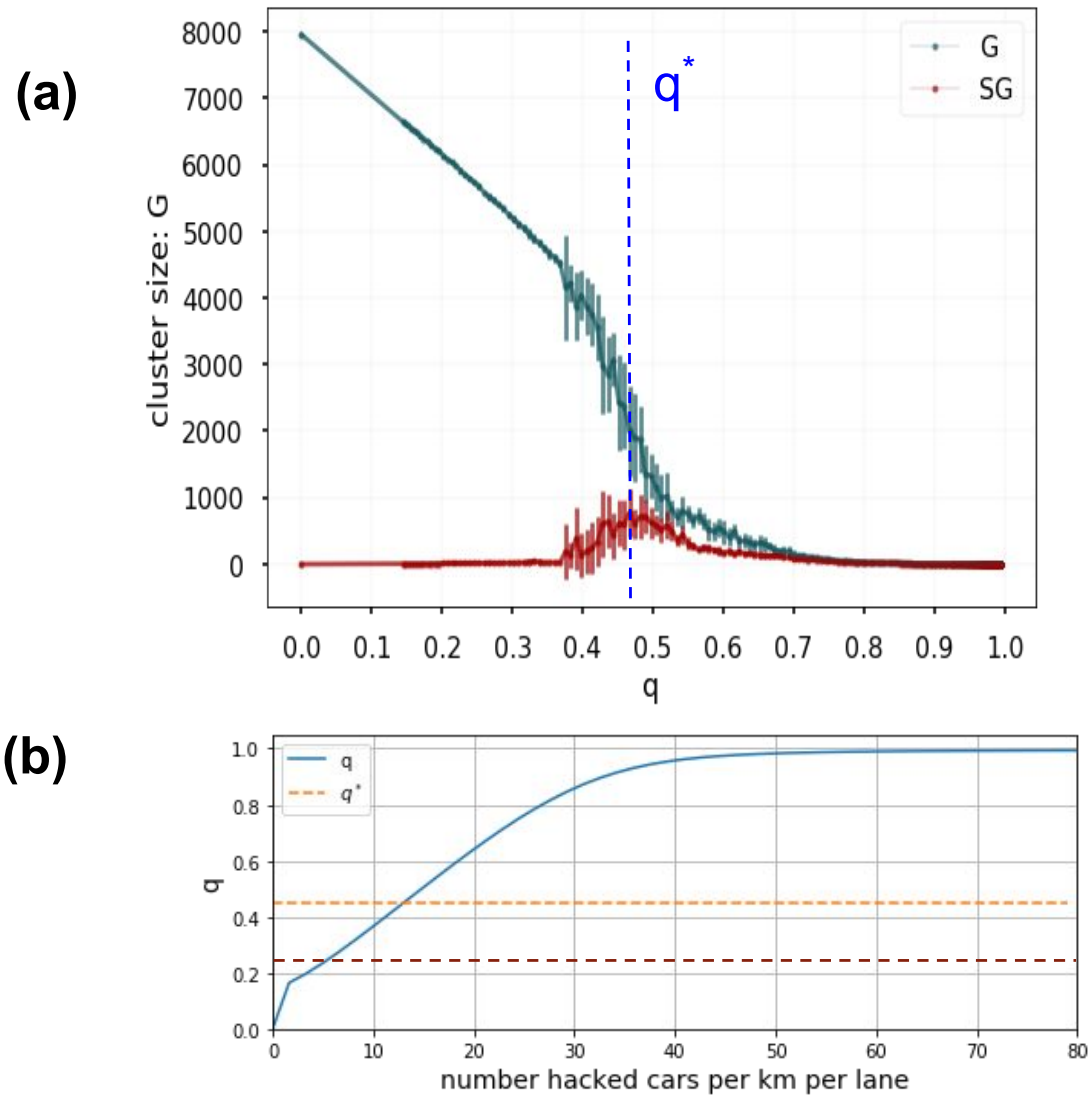

Figure B.7: Details for determining when a percolation-of-percolations event occurs for a the Manhattan city road network. (a) We define q as the probability of road blockage averaged over all the road probabilities in Manhattan, for a given ρ_H. Here we plot the size of the largest connected component **G**, and the second largest connected component **SG** of the Manhattan street network as a function of q. (b) shows a comparison of q and ρ_H with an orange dotted line showing the point of city fragmentation $q \approx 0.45$ and a red dotted line showing the onset of traffic jams $q \approx 0.25$.

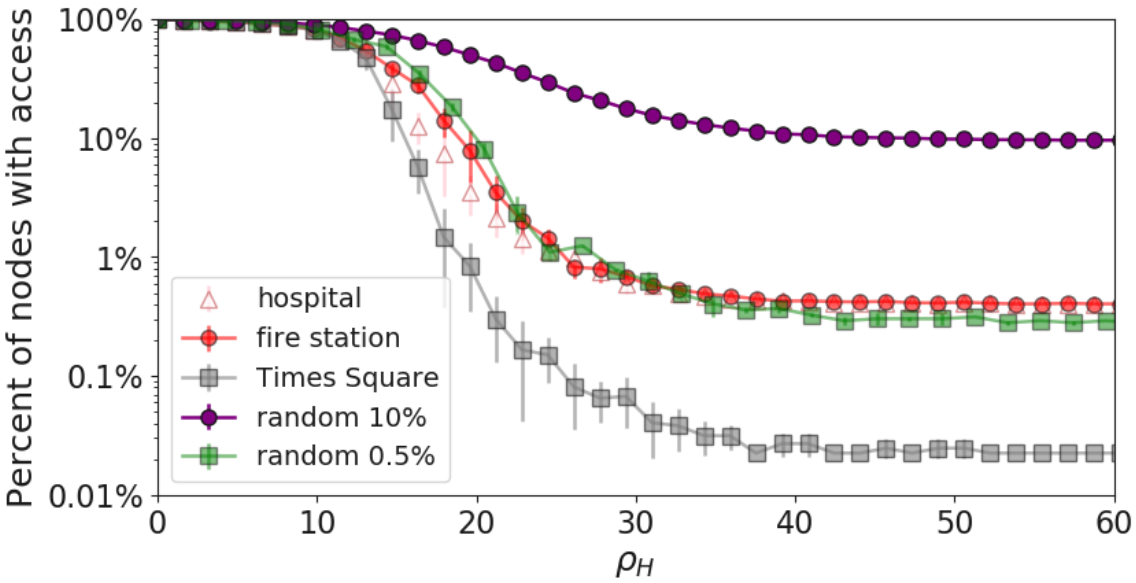

Figure B.8: Plot of the fraction of nodes with access to a service (log scale) against ρ_H. A simple random sample containing 10% of the city's nodes (purple circles), emergency services (white triangles for hospitals and red circles for fire stations), a simple random sample containing 0.5% of the city's nodes (green squares), and a single node of interest are plotted to demonstrate the general trend as well as the effect of pre-hack service abundance in the city. Note that the green squares fall right on top of the emergency services data points, indicating that the reduction in emergency services is *despite* their being well distributed throughout Manhattan.

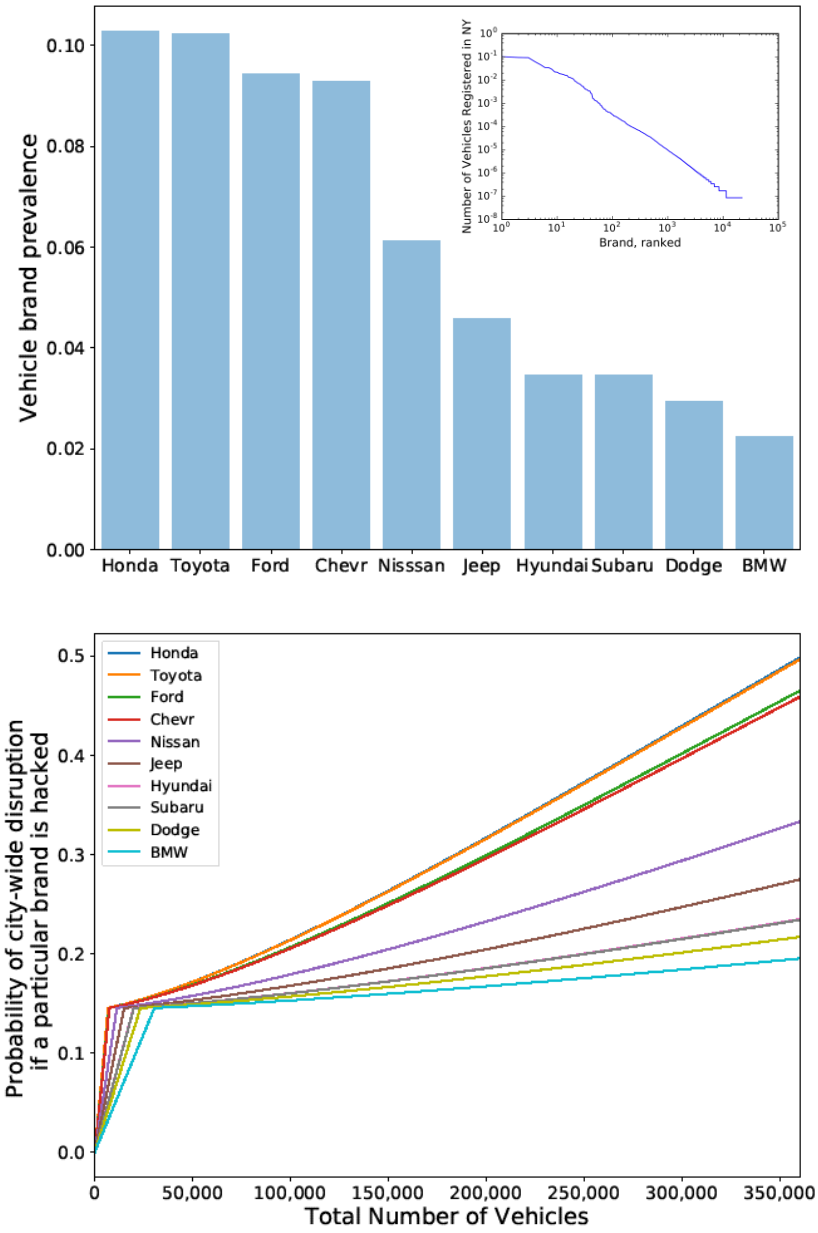

Figure B.9: New York State vehicle brand prevalence and hacking risks. (a) Histogram of brand prevalence as a fraction of all vehicles registered in NY. Inset: Rank histogram of brand prevalence. (b) Density-dependent probability of city-wide disruption in the event that all cars of a particular brand are suddenly and simultaneously disabled. Different colors correspond to different manufacturing brands.

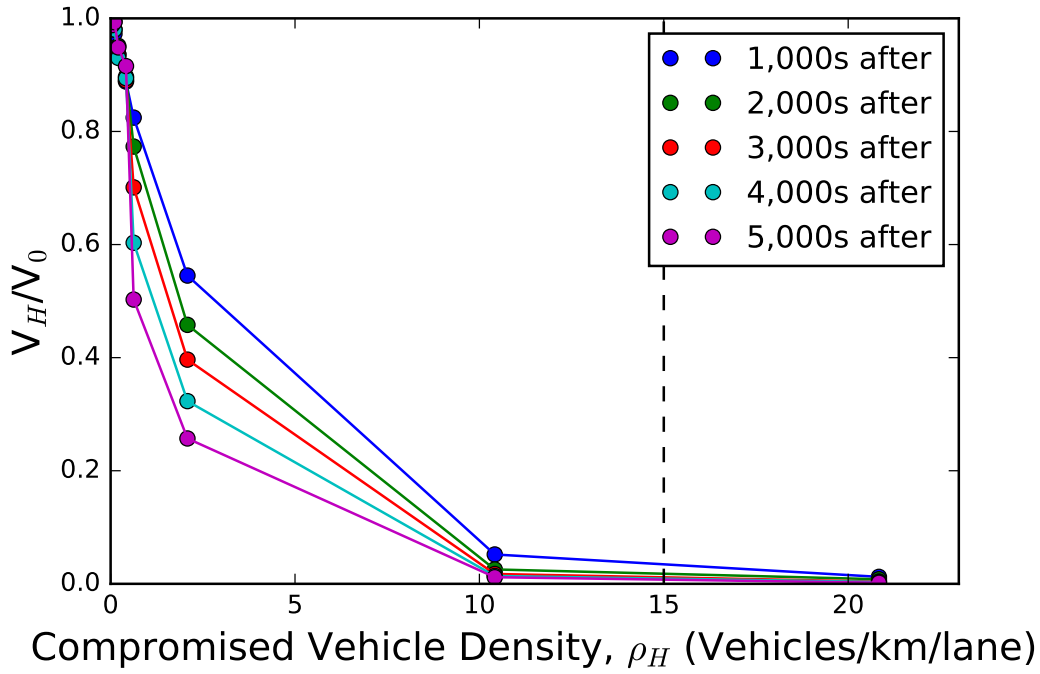

Figure B.10: Relative velocity of simulated vehicles in a post-hack environment on a Manhattan-like traffic grid. Velocities were computed on a 5×5 lattice using SUMO. V_0 denotes average velocity pre-hack and V_H denotes average velocity post-hack. Dashed line indicates percolation threshold of the 5×5 grid.

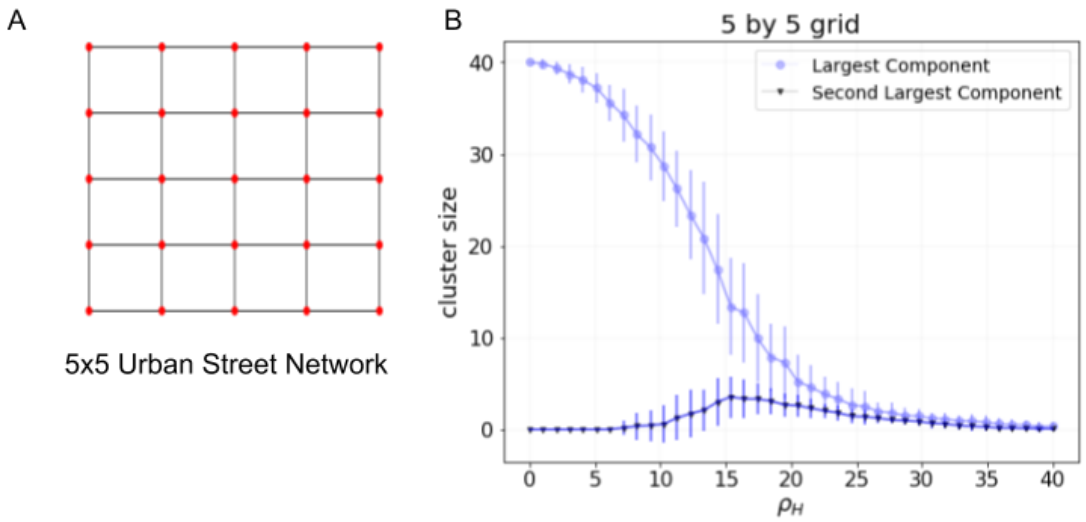

Figure B.11: Analysis of a 5×5 Manhattan-like street grid, using Eq. (1), and the same parameters that were used to generate Fig. B.10. Namely, $L = 200$ m, $\ell = 3$ lanes, and $s = 14$ m. Network fragmentation occurs at a similar hacked vehicle density to that of Manhattan, likely due to the similarity in network structure and topology. Network fracture also occurs in the same hacked vehicle density regime as the zero-flux regime probed by dynamic simulations shown in Fig. B.10.

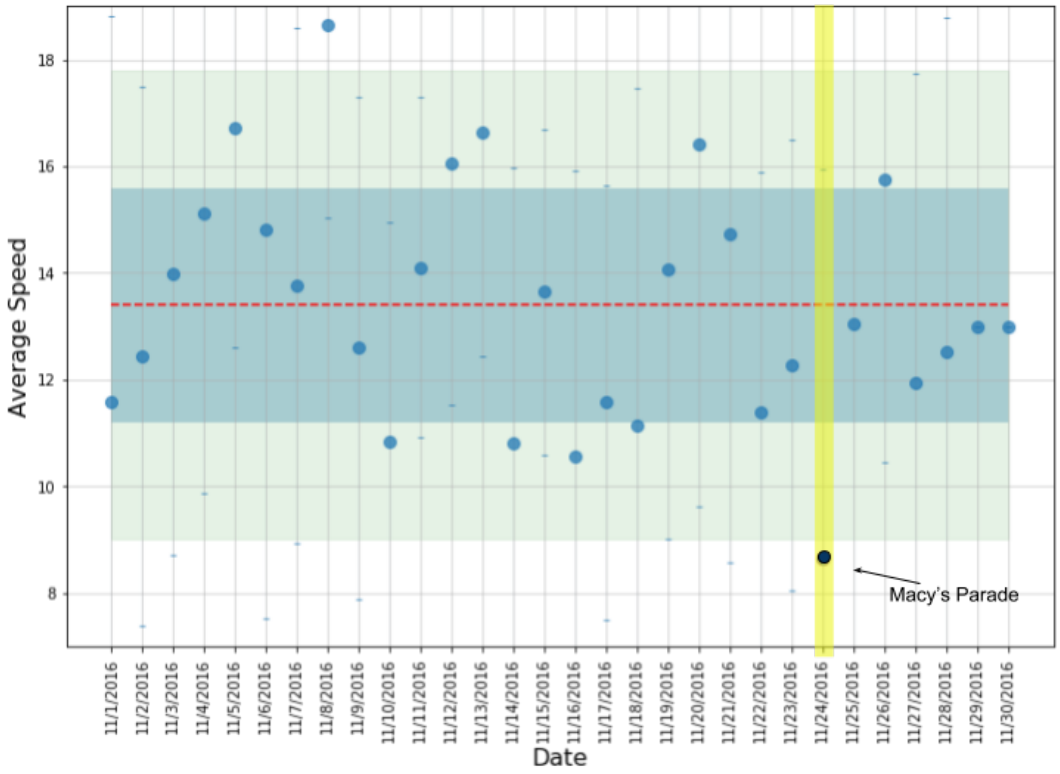

Figure B.12: Average traffic speeds within one block of Macy's parade route during 12:00 pm to 8:00 pm for each day of November (blue points) including Thanksgiving, which was the actual day of Macy's Day Parade (dark blue point near bottom of graph). The red dotted line shows the monthly average speed, the blue shaded region is the monthly average $\pm$ one standard deviation, and the pale green shaded region is the monthly average $\pm$ two standard deviations.

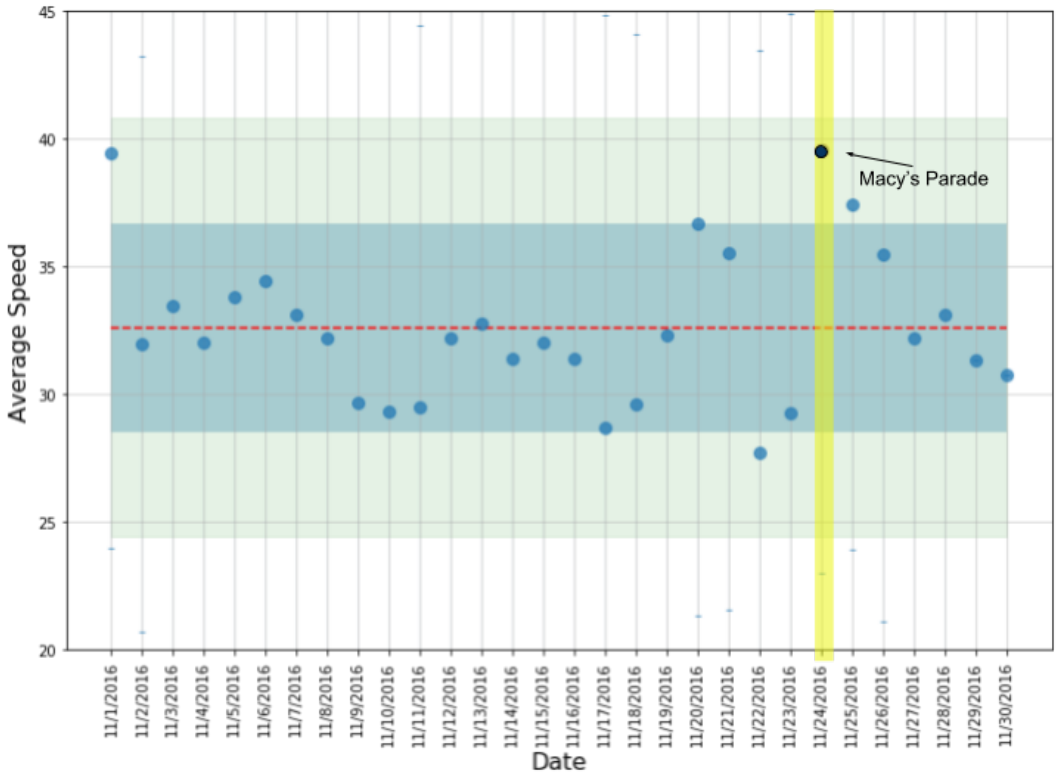

Figure B.13: Average traffic speeds over all of Manhattan during 12:00 pm to 8:00 pm for each day of November (blue points) including Thanksgiving, which was the day of the Macy's Day Parade (dark blue). Outside of the immediate vicinity of the parade traffic congestion was within normal limits. The red dotted line shows the monthly average speed, the blue shaded region is the monthly average $\pm$ one standard deviation, and the pale green shaded region is the monthly average $\pm$ two standard deviations.

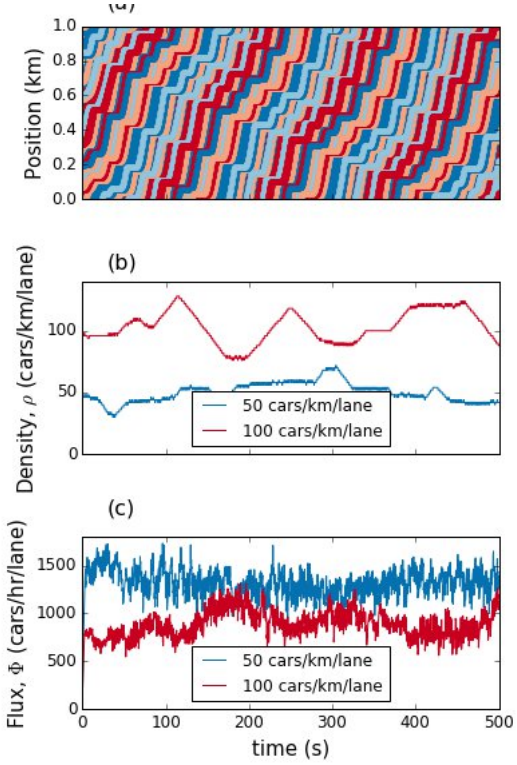

Figure B.14: Basic time-dependent quantification of simulated human-driven vehicles. (a) Space-time diagram of vehicle trajectories. Here, each randomly colored line (various shades of green) is a vehicle with average velocity $\Delta x/\Delta t > 0$. When the local slope is flat, the vehicle has stopped due to the emergence of backwards-propagating density waves ($\Delta x/\Delta t < 0$, shaded orange). Measurements of the (b) density and (c) flux show random statistical fluctuations that depend on the number of vehicles N_H in the simulation. Note, the total length of the simulated road $L = 1.0$ km, so that the average density $\approx N_H/L$.

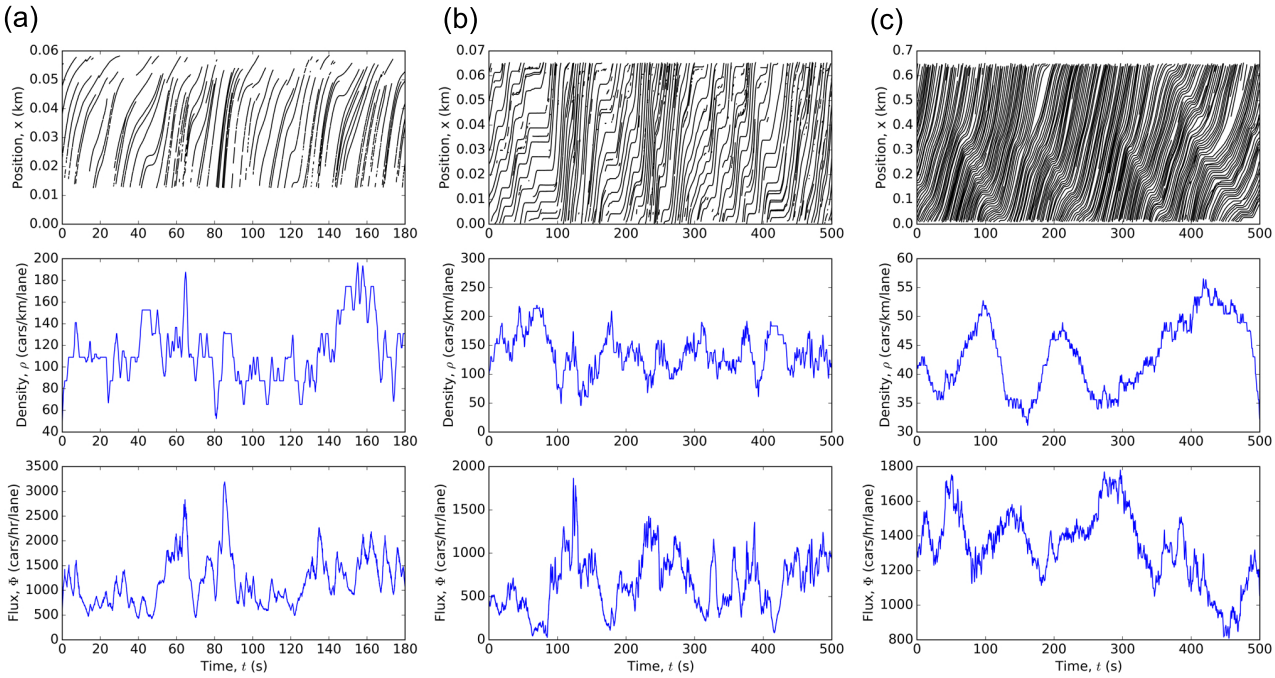

Figure B.15: Basic time-dependent quantification of empirical human-driven vehicles. The three data sources in (a-c) correspond to the same three data sources described in the main text Fig. 4.3. The three rows of plots shown here mimic Fig. B.14, and show qualitative similarities.

REFERENCES

[1] S. S. Branda, "Vik, å, friedman, l., & kolter, r. (2005)," in *Biofilms: The matrix revisited*, 13(1: Trends in Microbiology, pp. 20–26.

[2] W. F. Ratcliff, *BIOL*, vol. 8803, 2016.

[3] W. B. Whitman, D. C. Coleman, and W. J. Wiebe, "Prokaryotes: The unseen majority," in *Proc. Natl*, Acad. Sci. USA 95, 1998, pp. 6578–6583.

[4] W. Pohl, M. Hoppert, C. Flies, B. Gunzl, H. Ruppert, and S. J. E. biofilms: "A model for extraterrestrial ecological niches?" *InInstruments, Methods, and Missions for Astrobiology II International Society for Optics and Photonics*, vol. Vol. 3755,). Pp. 223–232, 1999.

[5] J. Toporski, A. Steele, D. S. McKay, and F. Westall, "Bacterial biofilms in astrobiology: The importance of life detection," in *InFossil and Recent Biofilms. , Dordrecht*, 2003, pp. 429–445.

[6] R. M.B. f. Donlan, "A clinically relevant microbiological process," *Clin. Infect*, vol. 33, pp. 1387–1392, 2001.

[7] M. Jamal, W. Ahmad, S. Andleeb, F. Jalil, M. Imran, M. A. Nawaz, T. Hussain, M. Ali, M. Rafiq, and K. M. B. biofilm and, "And associated infections," *Journal of the Chinese Medical AssociationOct*, vol. 15, 2017.

[8] J. G. Thomas, I. Litton, and H. Rinde, "Economic impact of biofilms on treatment costs," *Biofilms, Infection and Antimicrobial Therapy*, pp. 21–37, 2006.

[9] C. G. Kumar and A. Sk., "Significance of microbial biofilms in food industry: A review," *International journal of food microbiologyJun*, vol. 30, no. 42, pp. 9–27, 1998.

[10] R. Be., "Biofilms in the water industry," *American Society of Microbiology*, vol. 1, pp. 359–378, 2004.

[11] P. F. Sanders and S. Pj., "Biofouling in the oil industry," *American Society of Microbiology*, vol. 1, pp. 171–198, 2005.

[12] J. D. Zardus, B. T. Nedved, Y. Huang, C. Tran, and H. Mg., "Microbial biofilms facilitate adhesion in biofouling invertebrates," *The Biological BulletinFeb;*, vol. 214, no. 1, pp. 91–8, 2008.

[13] C. Even, C. Marlire, J. M. Ghigo, J. M. Allain, A. Marcellan, and E. Raspaud, "Recent advances in studying single bacteria and biofilm mechanics," *Advances in colloid and interface scienceSep*, vol. 1, no. 247, pp. 573–88, 2017.

[14] N. Høiby, T. Bjarnsholt, M. Givskov, S. Molin, and O. Ciofu, "Antibiotic resistance of bacterial biofilms," *International journal of antimicrobial agentsApr*, vol. 1, no. 35, p. 4, 2010.

[15] J. U. Kreft, C. Picioreanu, J. W. Wimpenny, and van Loosdrecht Mc., "Individual-based modelling of biofilms," *MicrobiologyNov*, vol. 1, no. 147, p. 11, 2001.

[16] D. R. Espeso, A. Carpio, and B. Einarsson, "Differential growth of wrinkled biofilms," *Physical Review EFeb*, vol. 18, p. 91, 2015.

[17] F. L. Hellweger and V. A Bucci, "Bunch of tiny individualsindividual-based modeling for microbes," *Ecological ModellingJan*, vol. 10, no. 220, p. 1, 2009.

[18] C. Picioreanu, M. C. Van Loosdrecht, and H. Jj., "Mathematical modeling of biofilm structure with a hybrid differentialdiscrete cellular automaton approach," *Biotechnology and bioengineeringApr*, vol. 5, no. 58, p. 1, 1998.

[19] L. A. Lardon, B. V. Merkey, S. Martins, A. Dtsch, C. Picioreanu, J. U. Kreft, and S. B. iDynoMiCS: "Nextgeneration individualbased modelling of biofilms," *Environmental microbiologySep;*, vol. 13, no. 9, pp. 2416–34, 2011.

[20] S. Ps., "Mechanisms of antibiotic resistance in bacterial biofilms," *International journal of medical microbiologyJul*, vol. 1, p. 292, 2002.

[21] M. Mg., "The physics of biofilmsan introduction," *Journal of Physics D: Applied PhysicsApr*, vol. 18, p. 49, 2016.

[22] S. Lecuyer, R. Stocker, and R. Rusconi, "Focus on the physics of biofilms," *New Journal of PhysicsMar*, vol. 27, p. 17, 2015.

[23] H. Boudarel, J. D. Mathias, B. Blaysat, and M. Grdiac, "Towards standardized mechanical characterization of microbial biofilms: Analysis and critical review," *NPJ biofilms and microbiomesAug*, vol. 20, p. 4, 2018.

[24] A. Persat, C. D. Nadell, M. K. Kim, F. Ingremeau, A. Siryaporn, K. Drescher, N. S. Wingreen, B. L. Bassler, Z. Gitai, and S. Ha., "The mechanical world of bacteria," *CellMay*, vol. 21, no. 161, p. 5, 2015.

[25] H. J. Busscher and R. Bos, "Van der mei hc. initial microbial adhesion is a determinant for the strength of biofilm adhesion," *FEMS microbiology lettersMay*, vol. 1, no. 128, p. 3, 1995.

[26] J. B. Xavier, C. Picioreanu, S. A. Rani, M. C. van Loosdrecht, and S. Ps., "Biofilm-control strategies based on enzymic disruption of the extracellular polymeric substance matrixa modelling study," *MicrobiologyDec*, vol. 1, no. 151, p. 12, 2005.

[27] S. Dhahri, M. Ramonda, and C. Marliere, "In-situ determination of the mechanical properties of gliding or non-motile bacteria by atomic force microscopy under physiological conditions without immobilization," *PLoS OneApr*, vol. 12, p. 8, 2013.

[28] L. McNally, E. Bernardy, J. Thomas, A. Kalziqi, J. Pentz, S. P. Brown, B. K. Hammer, P. J. Yunker, and R. Wc., "Killing by type vi secretion drives genetic phase separation and correlates with increased cooperation," *Nature communicationsFeb*, vol. 6, p. 8, 2017.

[29] R. Maroto, A. Raso, T. G. Wood, A. Kurosky, B. Martinac, and H. Op., "Trpc1 forms the stretch-activated cation channel in vertebrate cells," *Nature cell biologyFeb;*, vol. 7, p. 2, 2005.

[30] B. I. B. mechanosensitive channels: "Progress towards an understanding of their roles in cell physiology," *Current opinion in microbiologyApr*, vol. 1, no. 18, pp. 16–22, 2014.

[31] C. A Kung, "Possible unifying principle for mechanosensation," *NatureAug;*, vol. 436, p. 7051, 2005.

[32] J. Zakrisson, B. Singh, P. Svenmarker, K. Wiklund, H. Zhang, S. Hakobyan, M. Ramstedt, and M. Andersson, "Detecting bacterial surface organelles on single cells using optical tweezers," *LangmuirApr*, vol. 28, no. 32, p. 18, 2016.

[33] L. Craig, M. E. Pique, and T. Ja., "Type iv pilus structure and bacterial pathogenicity," *Nature Reviews MicrobiologyMay;*, vol. 2, p. 5, 2004.

[34] E. Bernardy, M. Turnsek, S. Wilson, C. Tarr, and B. Hammer, "Diversity of clinical and environmental isolates of vibrio cholerae in natural transformation and contact-dependent bacterial killing indicative of type vi secretion system activity," *Applied and Environmental Microbiology*, vol. 82, no. 9, pp. 2833–2842, 2016.

[35] B. K. Hammer and B. L. Bassler, "Quorum sensing controls biofilm formation in vibrio cholerae, mol," *Microbiol.*, vol. 50, p. 101, 2003.

[36] S. S. Branda, F. Chu, D. B. Kearns, R. Losick, and R. A Kolter, "Major protein component of the bacillus subtilis biofilm matrix," *Molecular microbiologyFeb;*, vol. 59, no. 4, pp. 1229–38, 2006.

[37] V. Krstgens, H. C. Flemming, J. Wingender, and W. Borchard, "Uniaxial compression measurement device for investigation of the mechanical stability of biofilms," *Journal of microbiological methodsJul*, vol. 30, no. 46, p. 1, 2001.

[38] Y. He, B. W. Peterson, M. A. Jongsma, Y. Ren, P. K. Sharma, and H. J. Busscher, "Van der mei hc," *Stress relaxation analysis facilitates a quantitative approach towards antimicrobial penetration into biofilms. PLoS OneMay*, vol. 27, p. 8, 2013.

[39] T. Shaw, M. Winston, C. J. Rupp, I. Klapper, and P. Stoodley, "Commonality of elastic relaxation times in biofilms," *Physical review lettersAug*, vol. 24, p. 93, 2004.

[40] A. Seminara, T. E. Angelini, J. N. Wilking, H. Vlamakis, S. Ebrahim, R. Kolter, D. A. Weitz, and B. Mp., "Osmotic spreading of bacillus subtilis biofilms driven by an extracellular matrix," *Proceedings of the National Academy of SciencesJan*, vol. 24, no. 109, p. 4, 2012.

[41] J. Prost, F. Jlicher, and J. J. A. gel physics, *Nature PhysicsFeb;*, vol. 11, p. 2, 2015.

[42] J. Ranft, M. Basan, J. Elgeti, J. F. Joanny, J. Prost, and F. J"ulicher, "Fluidization of tissues by cell division and apoptosis," *Proceedings of the National Academy of SciencesNov*, vol. 9, 2010.

[43] T. Risler, A. Peilloux, and J. Prost, "Homeostatic fluctuations of a tissue surface," *Physical review lettersDec*, vol. 18, p. 115, 2015.

[44] H. M. Lpez, J. Gachelin, C. Douarche, H. Auradou, and E. Clment, "Turning bacteria suspensions into superfluids," *Physical review lettersJul*, vol. 7, p. 115, 2015.

[45] A. Doostmohammadi, S. P. Thampi, and Y. Jm., "Defect-mediated morphologies in growing cell colonies," *Physical review lettersJul*, vol. 20, p. 117, 2016.

[46] A. Sokolov, I. S. Aranson, J. O. Kessler, and G. Re., "Concentration dependence of the collective dynamics of swimming bacteria," *Physical review lettersApr*, vol. 11, p. 98, 2007.

[47] H. P. Zhang, A. Beer, E. L. Florin, and S. H. C. motion and, "And density fluctuations in bacterial colonies," *Proceedings of the National Academy of SciencesAug*, vol. 3, no. 107, p. 31, 2010.

[48] P. Romanczuk, M. Br, W. Ebeling, B. Lindner, and S.-G.L. A. brownian particles, *The European Physical Journal Special TopicsMar*, vol. 1, no. 202, p. 1, 2012.

[49] J. Stenhammar, A. Tiribocchi, R. J. Allen, D. Marenduzzo, and C. Me., "Continuum theory of phase separation kinetics for active brownian particles," *Physical review lettersOct*, vol. 2, p. 111, 2013.

[50] Z. S. L. liquid crystals, *InLyotropic Chromonic Liquid Crystals 2017 (pp. 77-92)*. Cham: Springer.

[51] H. Wioland, F. G. Woodhouse, J. Dunkel, J. O. Kessler, and G. Re., "Confinement stabilizes a bacterial suspension into a spiral vortex," *Physical review lettersJun*, vol. 24, p. 110, 2013.

[52] M. C. Marchetti, J. F. Joanny, S. Ramaswamy, T. B. Liverpool, J. Prost, M. Rao, and S. Ra., "Hydrodynamics of soft active matter," *Reviews of Modern PhysicsJul*, vol. 19, p. 85, 2013.

[53] C. Me., "Diffusive transport without detailed balance in motile bacteria: Does microbiology need statistical physics?" *Reports on Progress in PhysicsMar*, vol. 9, p. 75, 2012.

[54] R. S. T. mechanics and. and statistics of active matter.

[55] C. Battle, C. P. Broedersz, N. Fakhri, V. F. Geyer, J. Howard, C. F. Schmidt, and M. Fc., "Broken detailed balance at mesoscopic scales in active biological systems," *ScienceApr*, vol. 29, no. 352, p. 6285, 2016.

[56] A. Kalziqi, D. Yanni, J. Thomas, S. L. Ng, S. Vivek, B. K. Hammer, and Y. P.I. A. Matter: "Activity from death and reproduction," *Physical review lettersJan*, vol. 5, p. 120, 2018.

[57] M. Tg., "Estimating the viscoelastic moduli of complex fluids using the generalized stokeseinstein equation," *Rheologica ActaAug*, vol. 1, no. 39, p. 4, 2000.

[58] T. A. Witten, T. Witten, P. A. Pincus, and P. P. S. fluids: polymers, *colloids, surfactants*. on Demand; Oxford University Press, 2004.

[59] R. Kubo, "The fluctuation-dissipation theorem and brownian motion," *InMany-body theory(*, vol. 1, 1966.

[60] R. Martnez-Garca, C. D. Nadell, R. Hartmann, K. Drescher, and B. J. C. adhesion and, "And fluid flow jointly initiate genotype spatial distribution in biofilms," *PLoS computational biologyApr*, vol. 16, p. 14, 2018.

[61] M. E. Davey and O. G. M. Biofilms: "From ecology to molecular genetics," *Microbiology and Molecular Biology Reviews*, vol. 64, p. 4,

[62] W. B. Whitman, D. C. Coleman, and W. W.P. T. unseen majority, "Pnas," *Sep;*, vol. 95, no. 12, pp. 6578–83, 1998.

[63] D. J. T. size and, "And the duration of air-carriage of respiratory droplets and droplet-nuclei," *Epidemiology & InfectionSep;*, vol. 44, no. 6, pp. 471–9, 1946.

[64] G. R. Johnson, L. D. Knibbs, T. J. Kidd, C. E. Wainwright, M. E. Wood, K. A. Ramsay, S. C. Bell, and M. L. A. novel method and, "And its application to measuring pathogen decay in bioaerosols from patients with respiratory disease," *PloS oneJul*, vol. 7, p. 11, 2016.

[65] T. Gilet and L. Bourouiba, "Fluid fragmentation shapes rain-induced foliar disease transmission," *Journal of the Royal Society InterfaceMar*, vol. 6, p. 12, 2015.

[66] R. D. Deegan, O. Bakajin, T. F. Dupont, G. Huber, S. R. Nagel, and W. Ta., "Capillary flow as the cause of ring stains from dried liquid drops," *Nature*, vol. 389, no. 6653, pp. 827–829, 1997.

[67] R. D. Deegan, D. T. F. Bakajin O, G. Huber, S. R. Nagel, and W. Ta., "Contact line deposits in an evaporating drop," *Phys. Rev*, vol. 62, 2000.

[68] D. Rd., "Pattern formation in drying drops phys," *Rev. E*, vol. 61, p. 475, 2000.

[69] P. J. Yunker, T. Still, M. A. Lohr, and A. G. Yodh, "Suppression of the coffee-ring effect by shape-dependent capillary interactions," *Nature ;*, vol. 476, no. 7360, pp. 308–311, 2011.

[70] W. Sempels, R. De Dier, H. Mizuno, J. Hofkens, and J. Vermant, "Auto-production of biosurfactants reverses the coffee ring effect in a bacterial system," *Nature Communications*, vol. 4, p. 1757, 2013.

[71] T. T. Nellimoottil, P. N. Rao, S. S. Ghosh, and A. Chattopadhyay, "Evaporation-induced patterns from droplets containing motile and nonmotile bacteria," *LangmuirAug*, vol. 14, no. 23, p. 17, 2007.

[72] T. Wong, T. Chen, X. Shen, and C. Ho, "Nanochromatography driven by the coffee ring effect," *Analytical Chemistry*, vol. 83, no. 6, pp. 1871–1873, 2011.

[73] A. K. Thokchom, R. Swaminathan, and S. A. F. flow and, "And particle dynamics inside an evaporating droplet containing live bacteria displaying chemotaxis," *LangmuirOct*, vol. 8, no. 30, p. 41, 2014.

[74] M. E. Hibbing, C. Fuqua, M. R. Parsek, and P. S. B. competition: surviving and, "And thriving in the microbial jungle," *Nature Reviews MicrobiologyJan*, vol. 1, no. 8, p. 1, 2010.

[75] N. Aj., "An outline of the dynamics of animal populations," *Australian journal of Zoology*, vol. 2, no. 1, pp. 9–65, 1954.

[76] A. Russell, S. Peterson, and J. Mougous, "Type vi secretion system effectors: Poisons with a purpose," *Nature Reviews Microbiology*, vol. 12, no. 2, pp. 137–148, 2014.

[77] C. M. Waters and B. L. Bassler, "Quorum sensing: Cell-to-cell communication in bacteria," *Annu. Rev*, vol. 21, pp. 319–346, 2005.

[78] O. Hallatschek and D. Nelson, "Gene surfing in expanding populations," *Theoretical Population Biology*, vol. 73, no. 1, pp. 158–170, 2008.

[79] M. Whiteley, S. P. Diggle, and G. E. P. in and, "And promise of bacterial quorum sensing research," *NatureNov;*, vol. 551, p. 7680, 2017.

[80] S. P. Diggle, A. S. Griffin, G. S. Campbell, and W. S. C. and, "And conflict in quorum-sensing bacterial populations," *NatureNov;*, vol. 450, p. 7168, 2007.

[81] K. H. Nealson, T. Platt, and H. Jw., "Cellular control of the synthesis and activity of the bacterial luminescent system," *Journal of bacteriologyOct*, vol. 1, no. 104, p. 1, 1970.

[82] B. W. Peterson, Y. He, Y. Ren, A. Zerdoum, M. R. Libera, P. K. Sharma, A.-J. Van Winkelhoff, D. Neut, P. Stoodley, H. C. Van Der Mei, *et al.*, "Viscoelasticity of biofilms and their recalcitrance to mechanical and chemical challenges," *FEMS microbiology reviews*, vol. 39, no. 2, pp. 234–245, 2015.

[83] J. L. Silverberg, M. Bierbaum, J. P. Sethna, and I. Cohen, "Collective motion of humans in mosh and circle pits at heavy metal concerts," *Physical Review Letters*, vol. 110, no. 22, p. 228 701, 2013.

[84] D. Helbing, "Traffic and related self-driven many-particle systems," *Reviews of Modern Physics*, vol. 73, pp. 1067–1141, 4 2001.

[85] G. Dervisoglu, G. Gomes, J. Kwon, R. Horowitz, and P. Varaiya, "Automatic calibration of the fundamental diagram and empirical observations on capacity."

[86] D. Helbing, "Fundamentals of traffic flow," *Physical Review E*, vol. 55, no. 3, p. 3735, 1997.

[87] K. Nagel and M. Schreckenberg, "A cellular automaton model for freeway traffic," *Journal de physique I*, vol. 2, no. 12, pp. 2221–2229, 1992.

[88] J. Treiterer, "Investigation of traffic dynamics by aerial photogrammetry techniques," Tech. Rep., 1975.

[89] K. Nagel and M. Paczuski, "Emergent traffic jams," *Physical Review E*, vol. 51, no. 4, p. 2909, 1995.

[90] D. Helbing and P. Molnar, "Social force model for pedestrian dynamics," *Physical review E*, vol. 51, no. 5, p. 4282, 1995.

[91] M. Bando, K. Hasebe, A. Nakayama, A. Shibata, and Y. Sugiyama, "Dynamical model of traffic congestion and numerical simulation," *Physical review E*, vol. 51, no. 2, p. 1035, 1995.

[92] M. Treiber and A. Kesting, "Modeling lane-changing decisions with mobil," *Traffic and Granular Flow07*, pp. 211–221, 2009.

[93] M. Treiber, A. Hennecke, and D. Helbing, "Congested traffic states in empirical observations and microscopic simulations," *Physical Review E*, vol. 62, no. 2, p. 1805, 2000.

[94] H. D. Treiber M, "Memory effects in microscopic traffic models and wide scattering in flow-density data.," *Physical Review E*, 2003.

[95] A. Bottinelli, D. T. Sumpter, and J. L. Silverberg, "Emergent structural mechanisms for high-density collective motion inspired by human crowds," *Physical Review Letters*, vol. 117, no. 22, p. 228 301, 2016.

[96] A. Bottinelli and J. L. Silverberg, "How to: Using mode analysis to quantify, analyze, and interpret the mechanisms of high-density collective motion," *Frontiers in Applied Mathematics and Statistics*, vol. 3, p. 26, 2017.

[97] L. D. Landau and E. M. Lifshitz, *Course of Theoretical Physics Vol 7: Theory and Elasticity*. Pergamon Press, 1959.

[98] `http://www.dot.ca.gov/video/index.html`.

[99] U. S. D. of Transportation Federal High Administration, *Ngsim datasets*, `https://www.its-rde.net/index.php/rdedataenvironment/10023` [Online; accessed 2-August-2017], 2005.

[100] V. Alexiadis, J. Colyar, and J. Halkias, "A model endeavor," *Public Roads*, vol. 70, no. 4, 2007.

[101] M. Montanino and V. Punzo, "Making ngsim data usable for studies on traffic flow theory: Multistep method for vehicle trajectory reconstruction," *Transportation Re-*

search Record: Journal of the Transportation Research Board, vol. 2390, pp. 99–111, 2013.

[102] M. Treiber and A. Kesting, "Traffic flow dynamics," *Traffic Flow Dynamics: Data, Models and Simulation, Springer-Verlag Berlin Heidelberg*, 2013.

[103] M. J. Lighthill and G. B. Whitham, "On kinematic waves. ii. a theory of traffic flow on long crowded roads," *Proceedings of the Royal Society of London A: Mathematical, Physical and Engineering Sciences*, vol. 229, no. 1178, pp. 317–345, 1955.

[104] G. F. Newell, "A simplified car-following theory: A lower order model," *Transportation Research Part B: Methodological*, vol. 36, no. 3, pp. 195–205, 2002.

[105] K. Nagel and M. Schreckenberg, "A cellular automaton model for freeway traffic," *Journal de Physique I*, vol. 2, no. 12, pp. 2221–2229, 1992.

[106] T. Nagatani, "The physics of traffic jams," *Reports on Progress in Physics*, vol. 65, no. 9, p. 1331, 2002.

[107] M. Treiber and D. Helbing, "Mobil: General lane-changing model for car-following models," *Disponıvel em http://www. mtreiber. de/publications/MOBIL_TRB. pdf, Acesso em dezembro de*, vol. 2009, 2006.

[108] D Helbing, *Video of traffic waves. website*.

[109] Y. Sugiyama, M. Fukui, M. Kikuchi, K. Hasebe, A. Nakayama, K. Nishinari, S.-i. Tadaki, and S. Yukawa, "Traffic jams without bottlenecksexperimental evidence for the physical mechanism of the formation of a jam," *New journal of physics*, vol. 10, no. 3, p. 033 001, 2008.

[110] S.-i. Tadaki, M. Kikuchi, M. Fukui, A. Nakayama, K. Nishinari, A. Shibata, Y. Sugiyama, T. Yosida, and S. Yukawa, "Phase transition in traffic jam experiment on a circuit," *New Journal of Physics*, vol. 15, no. 10, p. 103 034, 2013.

[111] F. Wu, R. Stern, M. Churchill, M. L. Delle Monache, K. Han, B. Piccoli, and D. Work, "Measuring trajectories and fuel consumption in oscillatory traffic: Experimental results," in *Transportation Research Board 96th Annual Meeting (TRB 2017)*, 2017, p. 14.

[112] M. R. Flynn, A. R. Kasimov, J.-C. Nave, R. R. Rosales, and B. Seibold, "Self-sustained nonlinear waves in traffic flow," *Physical Review E*, vol. 79, no. 5, p. 056 113, 2009.

[113] L. Wang, B. K. Horn, and G. Strang, "Eigenvalue and eigenvector analysis of stability for a line of traffic," *Studies in Applied Mathematics*, vol. 138, no. 1, pp. 103–132, 2017.

[114] *Connected car market report*, https://www.statista.com/outlook/320/109/connected-car/united-states#, Accessed: 2018-05-10, 2018.

[115] *Connected vehicle benefits*, https://www.its.dot.gov/factsheets/pdf/ConnectedVehicleBenefits.pdf, Accessed: 2018-03-28, 2018.

[116] *World's biggest data breaches*, http://www.informationisbeautiful.net/visualizations/worlds-biggest-data-breaches-hacks/, Accessed: 2018-05-10, 2018.

[117] *General accountability office (gao), vehicle cybersecurity: Dot and industry have efforts under way, but dot needs to define its role in responding to a realworld attack, gao- 16-350*, http://www.gao.gov/assets/680/676064.pdf, Accessed: 2018-03-27, 2016.

[118] S. Parkinson, P. Ward, K. Wilson, and J. Miller, "Cyber threats facing autonomous and connected vehicles: Future challenges," *IEEE Transactions on Intelligent Transportation Systems*, vol. 18, no. 11, pp. 2898–2915, 2017.

[119] M. H. Eiza and Q. Ni, "Driving with sharks: Rethinking connected vehicles with vehicle cybersecurity," *IEEE Vehicular Technology Magazine*, vol. 12, no. 2, pp. 45–51, 2017.

[120] *Hackers are the real obstacle for self-driving vehicles*, https://www.technologyreview.com/s/60861 are-the-real-obstacle-for-self-driving-vehicles/.

[121] A. Kesting, M. Treiber, M. Schönhof, F. Kranke, and D. Helbing, "Jam-avoiding adaptive cruise control (acc) and its impact on traffic dynamics," in *Traffic and Granular Flow05*, Springer, 2007, pp. 633–643.

[122] A. Kesting, M. Treiber, and D. Helbing, "Enhanced intelligent driver model to access the impact of driving strategies on traffic capacity," *Philosophical Transactions of the Royal Society A: Mathematical, Physical and Engineering Sciences*, vol. 368, no. 1928, pp. 4585–4605, 2010.

[123] A. Talebpour and H. S. Mahmassani, "Influence of autonomous and connected vehicles on stability of traffic flow," Tech. Rep., 2015.

[124] C.-Y. Liang and H. Peng, "Optimal adaptive cruise control with guaranteed string stability," *Vehicle system dynamics*, vol. 32, no. 4-5, pp. 313–330, 1999.

[125] L. Davis, "Effect of adaptive cruise control systems on traffic flow," *Physical Review E*, vol. 69, no. 6, p. 066 110, 2004.

[126] S. Parkinson, P. Ward, K. Wilson, and J. Miller, "Cyber threats facing autonomous and connected vehicles: Future challenges," *IEEE Transactions on Intelligent Transportation Systems*, vol. 18, no. 11, pp. 2898–2915, 2017.

[127] S. Cui, B. Seibold, R. Stern, and D. B. Work, "Stabilizing traffic flow via a single autonomous vehicle: Possibilities and limitations," in *2017 IEEE Intelligent Vehicles Symposium (IV)*, IEEE, 2017, pp. 1336–1341.

[128] N. Kheterpal, K. Parvate, C. Wu, A. Kreidieh, E. Vinitsky, and A. Bayen, "Flow: Deep reinforcement learning for control in sumo," *EPiC Series in Engineering*, vol. 2, pp. 134–151, 2018.

[129] M. Amoozadeh, A. Raghuramu, C.-N. Chuah, D. Ghosal, H. M. Zhang, J. Rowe, and K. Levitt, "Security vulnerabilities of connected vehicle streams and their impact on cooperative driving," *IEEE Communications Magazine*, vol. 53, no. 6, pp. 126–132, 2015.

[130] C. W. Axelrod, "Cybersecurity in the age of autonomous vehicles, intelligent traffic controls and pervasive transportation networks," in *Systems, Applications and Technology Conference (LISAT), 2017 IEEE Long Island*, IEEE, 2017, pp. 1–6.

[131] *Autonomous cars without human drivers are coming to california next year*, `http://bgr.com/2017/10/11/self-driving-car-tests-california-rules/`, Accessed: 2018-03-27, 2017.

[132] *Driverless testing of autonomous vehicles*, `https://www.dmv.ca.gov/portal/dmv/detail/vr/autonomous/auto`, Accessed: 2018-03-27, 2018.

[133] M. Richtel and C. Dougherty, "Googles driverless cars run into problem: Cars with drivers," *New York Times*, vol. 1, 2015.

[134] N. Bißmeyer, C. Stresing, and K. M. Bayarou, "Intrusion detection in vanets through verification of vehicle movement data," in *Vehicular Networking Conference (VNC), 2010 IEEE*, IEEE, 2010, pp. 166–173.

[135] C. Chen, L. Li, J. Hu, and C. Geng, "Calibration of mitsim and idm car-following model based on ngsim trajectory datasets," in *Vehicular Electronics and Safety (ICVES), 2010 IEEE International Conference on*, IEEE, 2010, pp. 48–53.

[136] G. Whitham, "On kinematic waves ii. a theory of traffic flow on long crowded roads," *Proc. R. Soc. Lond. A*, vol. 229, no. 1178, pp. 317–345, 1955.

[137] C. Thomas and D. J. Durian, "Fraction of clogging configurations sampled by granular hopper flow," *Physical review letters*, vol. 114, no. 17, p. 178 001, 2015.

[138] I. Zuriguel, D. R. Parisi, R. C. Hidalgo, C. Lozano, A. Janda, P. A. Gago, J. P. Peralta, L. M. Ferrer, L. A. Pugnaloni, E. Clément, *et al.*, "Clogging transition of many-particle systems flowing through bottlenecks," *Scientific reports*, vol. 4, p. 7324, 2014.

[139] H. Péter, A. Libál, C. Reichhardt, and C. J. Reichhardt, "Crossover from jamming to clogging behaviors in heterogeneous environments," *arXiv preprint arXiv:1712.03307*, 2017.

[140] M Sahini and M Sahimi, *Applications of percolation theory*. CRC Press, 2014.

[141] H. J. Blitzstein JK, *Introduction to probability*, 2017.

[142] C. Systematics, "Ngsim us 101 data analysis: Summary report," *Prepared for Federal Highway Administration*, 2005.

[143] R. Albert, H. Jeong, and A.-L. Barabási, "Error and attack tolerance of complex networks," *nature*, vol. 406, no. 6794, p. 378, 2000.

[144] D. S. Callaway, M. E. Newman, S. H. Strogatz, and D. J. Watts, "Network robustness and fragility: Percolation on random graphs," *Physical review letters*, vol. 85, no. 25, p. 5468, 2000.

[145] S. Abbar, T. Zanouda, and J. Borge-Holthoefer, "Robustness and resilience of cities around the world," *arXiv preprint arXiv:1608.01709*, 2016.

[146] J. Wang, "Resilience of self-organised and top-down planned citiesa case study on london and beijing street networks," *PLoS one*, vol. 10, no. 12, e0141736, 2015.

[147] G. Boeing, "Osmnx: New methods for acquiring, constructing, analyzing, and visualizing complex street networks," *Computers, Environment and Urban Systems*, vol. 65, pp. 126–139, 2017.

[148] D. Li, B. Fu, Y. Wang, G. Lu, Y. Berezin, H. E. Stanley, and S. Havlin, "Percolation transition in dynamical traffic network with evolving critical bottlenecks," *Proceedings of the National Academy of Sciences*, vol. 112, no. 3, pp. 669–672, 2015.

[149] L. M. Shekhtman and S. Havlin, "Percolation of hierarchical networks and networks of networks," *Phys. Rev. E*, vol. 98, p. 052 305, 5 2018.

[150] G. Zeng, D. Li, S. Guo, L. Gao, Z. Gao, H. E. Stanley, and S. Havlin, "Switch between critical percolation modes in city traffic dynamics," *Proceedings of the National Academy of Sciences*, vol. 116, no. 1, pp. 23–28, 2019.

[151] M. Behrisch, L. Bieker, J. Erdmann, and D. Krajzewicz, "Sumo–simulation of urban mobility," in *The Third International Conference on Advances in System Simulation (SIMUL 2011), Barcelona, Spain*, vol. 42, 2011.

[152] *Connected vehicle pilot deployment program: New york city, new york*, https://www.its.dot.gov/factsheets/pdf/NYCCVPliot_Factsheet_020817.pdf, Accessed: 2018-05-11, 2017.

[153] *Nyc dot advances to phases two and three of federal connected vehicle pilot program*, http://www.nyc.gov/html/dot/html/pr2016/pr16-094.shtml, Accessed: 2018-05-11, 2016.

[154] *Nypd motor vehicle collisions*, https://www.autoinsurancecenter.com/traffic-accidents-in-new-york-city.html, Accessed: 2018-10-15, 2018.

[155] S. Shamsh and V. Dubey, "Roaming honeypots along with ids in mobile ad-hoc networks," *International Journal of Computer Applications*, vol. 69, no. 23, 2013.

[156] M. H. Almeshekah and E. H. Spafford, "Cyber security deception," in *Cyber Deception*, Springer, 2016, pp. 23–50.

[157] E. Szathmáry and J. M. Smith, "The major evolutionary transitions," *Nature*, vol. 374, no. 6519, pp. 227–232, Mar. 1995.

[158] A. H. Knoll, "The multiple origins of complex multicellularity," *Annual Review of Earth and Planetary Sciences*, vol. 39, pp. 217–239, 2011.

[159] D. C. Queller and J. E. Strassmann, "Beyond society: The evolution of organismality," *Philosophical Transactions of the Royal Society of London B: Biological Sciences*, vol. 364, no. 1533, pp. 3143–3155, 2009. eprint: http://rstb.royalsocietypublishing.org/content/364/1533/3143.full.pdf.

[160] T. Brunet and N. King, "The origin of animal multicellularity and cell differentiation," *Developmental Cell*, vol. 43, no. 2, pp. 124–140, Oct. 2017.

[161] T. Cavalier-Smith, "Origin of animal multicellularity: Precursors, causes, consequences—the choanoflagellate/sponge transition, neurogenesis and the cambrian explosion," *Philosophical Transactions of the Royal Society of London B: Biologi-*

cal Sciences, vol. 372, no. 1713, 2017. eprint: http://rstb.royalsocietypublishing.org/content/372/1713/20150476.full.pdf.

[162] G. A. Cooper and S. A. West, "Division of labour and the evolution of extreme specialization," *Nature Ecology & Evolution*, 2018.

[163] R. E. Michod, Y. Viossat, C. A. Solari, M. Hurand, and A. M. Nedelcu, "Life-history evolution and the origin of multicellularity," *Journal of Theoretical Biology*, vol. 239, no. 2, pp. 257 –272, 2006, Special Issue in Memory of John Maynard Smith.

[164] I. Ispolatov, M. Ackermann, and M. Doebeli, "Division of labour and the evolution of multicellularity," *Proceedings of the Royal Society of London B: Biological Sciences*, vol. 279, no. 1734, pp. 1768–1776, 2012. eprint: http://rspb.royalsocietypublishing.org/content/279/1734/1768.full.pdf.

[165] C. A. Solari, J. O. Kessler, and R. E. Goldstein, "A general allometric and life-history model for cellular differentiation in the transition to multicellularity.," *The American Naturalist*, vol. 181, no. 3, pp. 369–380, 2013, PMID: 23448886. eprint: https://doi.org/10.1086/669151.

[166] R. E. Michod, "Evolution of individuality during the transition from unicellular to multicellular life," *Proceedings of the National Academy of Sciences of the United States of America*, vol. 104, no. Suppl 1, pp. 8613–8618, May 2007.

[167] S. A. West, R. M. Fisher, A. Gardner, and E. T. Kiers, "Major evolutionary transitions in individuality," *Proceedings of the National Academy of Sciences*, vol. 112, no. 33, pp. 10 112–10 119, 2015. eprint: http://www.pnas.org/content/112/33/10112.full.pdf.

[168] R. E. Michod, "Darwinian dynamics: Evolutionary transitions in fitness and individuality," *Complexity*, vol. 5, no. 1, pp. 42–43, 1999.

[169] H. J. Folse III and J. Roughgarden, "What is an individual organism? a multilevel selection perspective," *The Quarterly review of biology*, vol. 85, no. 4, pp. 447–472, 2010.

[170] L. W. Buss, *The Evolution of Individuality*. Princeton University Press, 1988, ISBN: 9781400858712.

[171] E. Libby and W. C. Ratcliff, "Ratcheting the evolution of multicellularity," *Science*, vol. 346, no. 6208, pp. 426–427, 2014.

[172] D. W. McShea, "Functional complexity in organisms: Parts as proxies," *Biology and Philosophy*, vol. 15, no. 5, pp. 641–668, 2000.

[173] J. Smith and E. Szathmáry, *The Major Transitions in Evolution*. OUP Oxford, 1997, ISBN: 9780198502944.

[174] H. J. Goldsby, A. Dornhaus, B. Kerr, and C. Ofria, "Task-switching costs promote the evolution of division of labor and shifts in individuality," *Proceedings of the National Academy of Sciences*, vol. 109, no. 34, pp. 13 686–13 691, 2012. eprint: http://www.pnas.org/content/109/34/13686.full.pdf.

[175] P. A. Corning and E. Szathmáry, "Synergistic selection: A darwinian frame for the evolution of complexity," *Journal of Theoretical Biology*, vol. 371, pp. 45 –58, 2015.

[176] C. A. Hidalgo and R. Hausmann, "The building blocks of economic complexity," *Proceedings of the National Academy of Sciences*, vol. 106, no. 26, pp. 10 570–10 575, 2009. eprint: http://www.pnas.org/content/106/26/10570.full.pdf.

[177] G. Boza, A. Szilágyi, Á. Kun, M. Santos, and E. Szathmáry, "Evolution of the division of labor between genes and enzymes in the rna world," *PLOS Computational Biology*, vol. 10, no. 12, pp. 1–9, Dec. 2014.

[178] M. Taborsky, J. G. Frommen, and C. Riehl, "Correlated pay-offs are key to cooperation," *Philosophical Transactions of the Royal Society of London B: Biological Sciences*, vol. 371, no. 1687, 2016. eprint: http://rstb.royalsocietypublishing.org/content/371/1687/20150084.full.pdf.

[179] R. E. Page, R. Scheiner, J. Erber, and G. V. Amdam, "The development and evolution of division of labor and foraging specialization in a social insect (apis mellifera l.)," *Current Topics in Developmental Biology*, Current Topics in Developmental Biology, vol. 74, pp. 253 –286, 2006.

[180] C. Rueffler, J. Hermisson, and G. P. Wagner, "Evolution of functional specialization and division of labor," *Proceedings of the National Academy of Sciences*, vol. 109, no. 6, pp. 1830–1831, 2012. eprint: http://www.pnas.org/content/109/6/E326/1.full.pdf.

[181] P. Szekely, H. Sheftel, A. Mayo, and U. Alon, "Evolutionary tradeoffs between economy and effectiveness in biological homeostasis systems," *PLOS Computational Biology*, vol. 9, no. 8, pp. 1–14, Aug. 2013.

[182] R. Findlay, "Comparative advantage," *The New Palgrave Dictionary of Economics: Volume 1–8*, pp. 924–929, 2008.

[183] B. Allen, G. Lippner, Y.-T. Chen, B. Fotouhi, N. Momeni, S.-T. Yau, and M. A. Nowak, "Evolutionary dynamics on any population structure," *Nature*, vol. 544, 227 EP –, 2017.

[184] A. Pavlogiannis, J. Tkadlec, K. Chatterjee, and M. A. Nowak, "Construction of arbitrarily strong amplifiers of natural selection using evolutionary graph theory," *Communications Biology*, vol. 1, no. 1, p. 71, 2018.

[185] J. Damuth and I. L. Heisler, "Alternative formulations of multilevel selection," *Biology and Philosophy*, vol. 3, no. 4, pp. 407–430, 1988.

[186] D. L. Kirk, "A twelve-step program for evolving multicellularity and a division of labor," *BioEssays*, vol. 27, no. 3, pp. 299–310, 2005.

[187] T. Wey, D. T. Blumstein, W. Shen, and F. Jordan, "Social network analysis of animal behaviour: A promising tool for the study of sociality," *Animal behaviour*, vol. 75, no. 2, pp. 333–344, 2008.

[188] E. Lieberman, C. Hauert, and M. A. Nowak, "Evolutionary dynamics on graphs," *Nature*, vol. 433, no. 7023, p. 312, 2005.

[189] R. E. Michod, "On the transfer of fitness from the cell to the multicellular organism," *Biology and Philosophy*, vol. 20, no. 5, pp. 967–987, 2005.

[190] R. E. Michod and D. Roze, "Transitions in individuality," *Proceedings of the Royal Society of London B: Biological Sciences*, vol. 264, no. 1383, pp. 853–857, 1997. eprint: `http://rspb.royalsocietypublishing.org/content/264/1383/853.full.pdf`.

[191] R. R. Lew, "How does a hypha grow? the biophysics of pressurized growth in fungi," *Nature Reviews Microbiology*, vol. 9, no. 7, p. 509, 2011.

[192] A. Simonin, J. Palma-Guerrero, M. Fricker, and N. L. Glass, "Physiological significance of network organization in fungi," *Eukaryotic Cell*, vol. 11, no. 11, pp. 1345–1352, 2012. eprint: `https://ec.asm.org/content/11/11/1345.full.pdf`.

[193] N. J. Butterfield, "Bangiomorpha pubescens n. gen., n. sp.: Implications for the evolution of sex, multicellularity, and the mesoproterozoic/neoproterozoic radiation of eukaryotes," *Paleobiology*, vol. 26, no. 3, pp. 386–404, 2000.

[194] D. L. Kirk, "A twelve-step program for evolving multicellularity and a division of labor," *BioEssays*, vol. 27, no. 3, pp. 299–310, 2005.

[195] M. Willensdorfer, "Organism size promotes the evolution of specialized cells in multicellular digital organisms," *Journal of evolutionary biology*, vol. 21, no. 1, pp. 104–110, Jan. 2008.

[196] J. T. Bonner, "The origins of multicellularity," *Integrative Biology: Issues, News, and Reviews*, vol. 1, no. 1, pp. 27–36, 1998.

[197] S. R. Fairclough, M. J. Dayel, and N. King, "Multicellular development in a choanoflagellate," *Current biology : CB*, vol. 20, no. 20, R875–R876, Oct. 26, 2010.

[198] S. Bengtson, T. Sallstedt, V. Belivanova, and M. Whitehouse, "Three-dimensional preservation of cellular and subcellular structures suggests 1.6 billion-year-old crown-group red algae," *PLOS Biology*, vol. 15, no. 3, pp. 1–38, Mar. 2017.

[199] M. L. Droser and J. G. Gehling, "Synchronous aggregate growth in an abundant new ediacaran tubular organism," *Science*, vol. 319, no. 5870, pp. 1660–1662, 2008. eprint: http://science.sciencemag.org/content/319/5870/1660.full.pdf.

[200] I. Berman-Frank, A. Quigg, Z. V. Finkel, A. J. Irwin, and L. Haramaty, "Nitrogen-fixation strategies and fe requirements in cyanobacteria," *Limnology and Oceanography*, vol. 52, no. 5, pp. 2260–2269, 2007. eprint: https://aslopubs.onlinelibrary.wiley.com/doi/pdf/10.4319/lo.2007.52.5.2260.

[201] W. C. Ratcliff, R. F. Denison, M. Borrello, and M. Travisano, "Experimental evolution of multicellularity," *Proceedings of the National Academy of Sciences*, vol. 109, no. 5, pp. 201 115 323–1600, Jan. 2012.

[202] N. J. Butterfield, "Bangiomorpha pubescens n. gen., n. sp.: Implications for the evolution of sex, multicellularity, and the mesoproterozoic/neoproterozoic radiation of eukaryotes," *Paleobiology*, vol. 26, no. 3, 2000.

[203] W. C. Ratcliff, J. D. Fankhauser, D. W. Rogers, D. Greig, and M. Travisano, "Origins of multicellular evolvability in snowflake yeast," *Nature Communications*, vol. 6, pp. 6102+, Jan. 2015.

[204] S. Bengtson, B. Rasmussen, M. Ivarsson, J. Muhling, C. Broman, F. Marone, M. Stampanoni, and A. Bekker, "Fungus-like mycelial fossils in 2.4-billion-year-old vesicular basalt," *Nature Ecology &Amp; Evolution*, vol. 1, 0141 EP –, 2017, Article.

[205] M. McCarthy and B. Enquist, "Organismal size, metabolism and the evolution of complexity in metazoans," in *Evolutionary Ecology Research*, vol. 7, Jul. 2005, pp. 681–696.

[206] N. A. Heim, J. L. Payne, S. Finnegan, M. L. Knope, M. Kowalewski, S. K. Lyons, D. W. McShea, P. M. Novack-Gottshall, F. A. Smith, and S. C. Wang, "Hierarchical complexity and the size limits of life," *Proceedings of the Royal Society of London B: Biological Sciences*, vol. 284, no. 1857, 2017. eprint: http://rspb.royalsocietypublishing.org/content/284/1857/20171039.full.pdf.

[207] C. R. McClain and A. G. Boyer, "Biodiversity and body size are linked across metazoans," *Proceedings of the Royal Society of London B: Biological Sciences*, vol. 276, no. 1665, pp. 2209–2215, 2009. eprint: http://rspb.royalsocietypublishing.org/content/276/1665/2209.full.pdf.

[208] R. E. Michod and A. M. Nedelcu, "On the reorganization of fitness during evolutionary transitions in individuality," *Integrative and Comparative Biology*, vol. 43, no. 1, pp. 64–73, 2003.

[209] J. F. Nash, "Equilibrium points in n-person games," *Proceedings of the National Academy of Sciences*, vol. 36, no. 1, pp. 48–49, 1950. eprint: http://www.pnas.org/content/36/1/48.full.pdf.

[210] J. M. Smith, "Evolution and the theory of games," in *Did Darwin Get It Right? Essays on Games, Sex and Evolution*. Boston, MA: Springer US, 1988, pp. 202–215, ISBN: 978-1-4684-7862-4.

[211] W. C. Ratcliff, J. T. Pentz, and M. Travisano, "Tempo and mode of multicellular adaptation in experimentally evolved Saccharomyces cerevisiae," *Evolution*, vol. 67, no. 6, pp. 1573–1581, Feb. 2013.

[212] N. King, "The unicellular ancestry of animal development," *Developmental cell*, vol. 7, no. 3, pp. 313–325, 2004.

[213] P. Kenrick and P. R. Crane, "The origin and early evolution of plants on land," *NATURE*, vol. 389, p. 4, 1997.

[214] T. Silberfeld, J. W. Leigh, H. Verbruggen, C. Cruaud, B. De Reviers, and F. Rousseau, "A multi-locus time-calibrated phylogeny of the brown algae (heterokonta, ochrophyta, phaeophyceae): Investigating the evolutionary nature of the brown algal crown radiationi," *Molecular phylogenetics and evolution*, vol. 56, no. 2, pp. 659–674, 2010.

[215] J. M. Cock and J. Collén, "Independent emergence of complex multicellularity in the brown and red algae," in *Evolutionary Transitions to Multicellular Life*, Springer, 2015, pp. 335–361.

[216] L. G. Nagy, G. M. Kovács, and K. Krizsán, "Complex multicellularity in fungi: Evolutionary convergence, single origin, or both?" *Biological Reviews*, vol. 93, no. 4, pp. 1778–1794, 2018.

[217] W. C. Ratcliff, M. Herron, P. L. Conlin, and E. Libby, "Nascent life cycles and the emergence of higher-level individuality," *Phil. Trans. R. Soc. B*, vol. 372, no. 1735, p. 20 160 420, 2017.

[218] E. Pennisi, "The power of many," *Science*, vol. 360, no. 6396, pp. 1388–1391, 2018. eprint: `http://science.sciencemag.org/content/360/6396/1388.full.pdf`.

[219] A. J. Black, P. Bourrat, and P. B. Rainey, "Ecological scaffolding and the evolution of individuality: The transition from cells to multicellular life," *BioRxiv*, p. 656 660, 2019.

[220] C. J. Rose, K. Hammerschmidt, and P. B. Rainey, "Meta-population structure and the evolutionary transition to multicellularity," 2019.

[221] V. Grimm and S. F. Railsback, *Individual-based modeling and ecology*. Princeton university press, 2005.

[222] E. M. Purcell, "Life at low reynolds number," *American journal of physics*, vol. 45, no. 1, pp. 3–11, 1977.

[223] C. Reas and B. Fry, *Getting Started with Processing: A Hands-On Introduction to Making Interactive Graphics*. Maker Media, Inc., 2015.

[224] N. F. Britton *et al.*, *Reaction-diffusion equations and their applications to biology.* Academic Press, 1986.

[225] L. E. Bingle, C. M. Bailey, and M. J. Pallen, "Type vi secretion: A beginner's guide," *Current Opinion in Microbiology*, vol. 11, no. 1, pp. 3–8, 2008.

[226] A. B. Russell, S. B. Peterson, and J. D. Mougous. Type VI secretion system effectors: poisons with purpose.

[227] .

[228] B. S. A. trans-kingdom effector, "Cludio nunes-alves nature reviews microbiology 12," vol. 461, p. 2014, 2014.

[229] J. Thomas, S. S. Watve, W. C. Ratcliff, and B. K. Hammer, "Horizontal gene transfer of functional type vi killing genes by natural transformation," *mBio*, vol. 8, pp. 654–17, 2017.

[230] S. S. Watve, J. Thomas, and C. B. K. Hammer, "Is a global positive regulator of competence," *type VI secretion, and chitinases in Vibrio cholerae, PLoS One*, vol. 10, 2015.

[231] M. Haklay and P. Weber, "Openstreetmap: User-generated street maps," *IEEE Pervasive Computing*, vol. 7, no. 4, pp. 12–18, 2008.

[232] B. Jiang and C. Claramunt, "A structural approach to the model generalization of an urban street network," *GeoInformatica*, vol. 8, no. 2, pp. 157–171, 2004.

[233] W. M. Liaw A, "Classification and regression by randomforest," *R News*, 2002.

[234] S. Adu, *Python-google-places*, `https://github.com/slimkrazy/python-google-places`, 2017.

[235] S. Kwoczek, S. Di Martino, and W. Nejdl, "Predicting and visualizing traffic congestion in the presence of planned special events," *Journal of Visual Languages & Computing*, vol. 25, no. 6, pp. 973–980, 2014.

[236] B. Pan, U. Demiryurek, C. Shahabi, and C. Gupta, "Forecasting spatiotemporal impact of traffic incidents on road networks," in *Data Mining (ICDM), 2013 IEEE 13th International Conference on*, IEEE, 2013, pp. 587–596.

[237] F. Sun, A. Dubey, and J. White, "Dxnatdeep neural networks for explaining non-recurring traffic congestion," in *Big Data (Big Data), 2017 IEEE International Conference on*, IEEE, 2017, pp. 2141–2150.

[238] *Data feeds*, `http://www.nyc.gov/html/dot/html/about/datafeeds.shtml`, Accessed: 2018-10-16, 2018.

[239] A. Greenberg, *How an entire national became russia's test lab for cyberwar*, `https://www.wired.com/story/russian-hackers-attack-ukraine` [Online; accessed 2-August-2017], 2017.

[240] T. Gjelten, *Cyberworm's origins unclear, but potential is not*, `http://www.npr.org/templates/story/story.php?storyId=130162219` [Online; accessed 2-August-2017], 2010.

[241] A. Shapiro, *Documentary explores the cyber-war secrets of stuxnet*, `http://www.npr.org/2016/07/04/484713086/documentary-explores-the-cyber-war-secrets-of-stuxnet` [Online; accessed 2-August-2017], 2016.

[242] B. Chappell and M. Penman, *Ransomware attacks ravage computer networks in dozens of countries*, `http://www.npr.org/sections/thetwo-way/`

2017/05/12/528119808/large-cyber-attack-hits-englands-nhs-hospital-system-ransoms-demanded [Online; accessed 2-August-2017], 2017.

[243] T. Ring, "Connected cars–the next target for hackers," *Network Security*, vol. 2015, no. 11, pp. 11–16, 2015.

[244] F. A. V. Policy, "Accelerating the next revolution in roadway safety, nhtsa, us dept," *Transportation*, 2016.

[245] J. Petit and S. E. Shladover, "Potential cyberattacks on automated vehicles," *IEEE Transactions on Intelligent Transportation Systems*, vol. 16, no. 2, pp. 546–556, 2015.

[246] M. Harris, "Researcher hacks self-driving car sensors," *IEEE Spectrum*, vol. 9, 2015.

[247] J. Harding, G. Powell, R. Yoon, J. Fikentscher, C. Doyle, D. Sade, M. Lukuc, J. Simons, and J. Wang, "Vehicle-to-vehicle communications: Readiness of v2v technology for application," National Highway Traffic Safety Administration, Tech. Rep., 2014.

[248] C. Harris and M. Stephens, "A combined corner and edge detector.," in *Alvey Vision Conference*, Manchester, UK, vol. 15, 1988, pp. 10–5244.

[249] B. D. Lucas, T. Kanade, *et al.*, "An iterative image registration technique with an application to stereo vision," *Proceedings DARPA Image Understanding Workshop*, 1981.

[250] D. M. Shaffer, A. B. Maynor, and W. L. Roy, "The visual perception of lines on the road," *Perception & Psychophysics*, vol. 70, no. 8, pp. 1571–1580, 2008.